Review Vol. 14, No. 4 / December 2022 / Advances in Optics and Photonics 783

Advances in Optics and Photonics

AR/VR light engines: perspectives and challenges

En-Lin Hsiang,[1,†] Zhiyong Yang,[1,†] Qian Yang,[1,†] Po-Cheng Lai,[2] Chih-Lung Lin,[2] and Shin-Tson Wu[1,*]

[1] College of Optics and Photonics, University of Central Florida, Orlando, Florida 32816, USA
[2] Department of Electrical Engineering, National Cheng Kung University, Tainan 701-01, Taiwan
*Corresponding author: swu@creol.ucf.edu
† These authors contributed equally to this work.

Received June 16, 2022; revised September 9, 2022; accepted September 9, 2022; published 9 November 2022

Augmented reality (AR) and virtual reality (VR) have the potential to revolutionize the interface between our physical and digital worlds. Recent advances in digital processing, data transmission, optics, and display technologies offer new opportunities for ubiquitous AR/VR applications. The foundation of this revolution is based on AR/VR display systems with high image fidelity, compact formfactor, and high optical efficiency. In this review paper, we start by analyzing the human vision system and the architectures of AR/VR display systems and then manifest the main requirements for the light engines. Next, the working principles of six display light engines, namely transmissive liquid crystal display, reflective liquid-crystal-on-silicon microdisplay, digital light processing microdisplay, micro light-emitting-diode microdisplay, organic light-emitting-diode microdisplay, and laser beam scanning displays, are introduced. According to the characteristics of these light engines, the perspectives and challenges of each display technology are analyzed through five performance metrics, namely resolution density, response time, efficiency/brightness/lifetime, dynamic range, and compactness. Finally, potential solutions to overcoming these challenges are discussed.

https://doi.org/10.1364/AOP.468066

AR/VR light engines: perspectives and challenges

En-Lin Hsiang, Zhiyong Yang, Qian Yang, Po-Cheng Lai, Chih-Lung Lin, and Shin-Tson Wu

1. INTRODUCTION

From televisions and monitors to smartphones and tablets, flat-panel displays have permeated our daily lives. These devices act as an interface between humans and machines to display digital information. From the oldest cathode-ray tube (CRT) displays, liquid crystal displays (LCDs) [1], organic light-emitting-diode (OLED) displays [2], to the latest micro light-emitting-diode (μLED) displays [3], the prosperous development in flat panel displays is primarily focused on high resolution, high dynamic range (HDR), vivid colors, wide viewing angle, fast motion picture response time (MPRT), thin profile, lower power consumption, and low cost [4–6]. Despite the tremendous progresses made in flat panel displays, there is still an ultimate desire for interactive displays to exhibit vivid three-dimensional (3D) visual experiences [7,8]. To achieve this goal, different types of augmented reality (AR) and virtual reality (VR) headsets have been proposed since the 1990s. However, the first wave of AR/VR headsets did not last too long due to insufficient support for high-speed communication (5G), small-sized displays, computing platforms, and battery capacity. Nowadays, all the above-mentioned bottlenecks have been gradually overcome, so another wave of AR/VR displays is once again receiving enthusiastic attention. Due to the broad interests and rapid development of AR/VR headsets, several articles reviewing recent advances from the perspectives of microdisplays, optical system integration including liquid crystal planar optics, holographic optics, freeform optics, meta-structure, and potential applications have been published [9–12]. Some of these reports emphasize how to generate a comfortable 3D visual experience by multiplane displays, integral imaging displays, and holographic displays, but very few analyze advanced light engines for AR/VR headsets. To remedy this deficiency, in this review paper, we focus on advanced light engines for AR/VR applications. It is worth noting that, depending on the applications and functionalities, the display characteristics of the optical engines in AR/VR devices are quite different from those used in direct-view flat panels. For example, in direct-view displays, such as TVs and desktop computers, Lambertian radiation pattern is favored to enable a wide viewing angle for multiple viewers, but in the near-eye projection systems, wide emission cones can cause image smudges and lower optical efficiency. In addition, the magnified images in AR/VR projection systems demand a much higher resolution density than traditional direct-view displays.

In the following sections, we first review the basic structure of the human visual system (HVS) and the architecture of AR/VR displays, and then manifest the requirements of advanced light engines to support AR/VR displays with a vivid 3D visual experience. After that, we dive into the working principles of six types of light engines: two of them are self-emissive types, OLED microdisplays and μLED microdisplays; three of them are light modulation types, transmissive LCDs, reflective liquid-crystal-on-silicon (LCOS) microdisplays, and digital light processing (DLP) microdisplays; and the last one is a scanning type, laser beam scanning (LBS) display. Next, five display performance metrics, resolution density, response time, efficiency/brightness/lifetime, HDR, and compactness, are proposed to analyze the advantages and challenges of each

light engine technology. During the analysis, advanced display configurations for each light engine to enhance its performance are also discussed.

2. HUMAN-CENTRIC AR/VR DISPLAYS

2.1. Comfort and Immersion

To achieve a spectacular viewing experience, AR/VR devices should offer both comfort and immersion [13,14]. Although there are some AR/VR applications realized with tabletop devices such as transparent displays [15], in this paper, we focus on the near-eye AR/VR devices. Comfort determines whether a user can wear the headset for an all-day use, whereas immersion requires that the display turns the virtuality into reality. The comfort comes with wearability [16], visual experience [17], and social interaction [18]. The immersion relates to all kinds of human senses, especially in aural, visual, and haptic senses [19]. The optics mainly determines the visual comfort and immersion [20], but it also plays an essential role for wearable and social comfort. For example, an AR/VR headset must have a small formfactor and be lightweight to widen acceptance by consumers [21]. The weight of a headset should be as evenly distributed as possible and, therefore, the center of gravity should be close to the head, enabling comfortable wearing for long-time use. As optics occupies a larger volume in a near-eye headset, both light engines and optical combiners should be lightweight and compact. Therefore, the first requirement for an advanced light engine is compactness. For an optical see-through AR device, it is expected that the user's eyes can be clearly seen by others, allowing for true eye contact for social interaction. Visual comfort and immersion are not easily measurable objective metrics. They are subjective experiences and vary from person to person [22]. Thus, the design of AR/VR devices should be a human-centric task. The HVS has its unique capabilities and limitations. A detailed understanding of the HVS helps designers to make sensible trade-offs in optical specifications or even reduce the system complexity by taking advantage of the HVS.

2.2. Architecture of Human Eye

The HVS consists of two eyes and the interpupillary distance (IPD) is the distance between the center of two eyes (Fig. 1(a1)), usually expressed in millimeters. This value (49–76 mm) varies by individual [23], depending on age, gender, and ethnicity. An eye is essentially an imaging system including multiple refractive surfaces and an adjustable iris [24]. A simplified eye model is illustrated in Fig. 1(a2). The incident light passes through cornea and aqueous humor and then enters the pupil, a round opening in the center of the iris. The iris adjusts the effective F number of the imaging system by changing the size of the pupil, limiting the light throughput. As light continues, it passes through the lens. The lens is attached to muscles which can change the shape and optical power of the lens by contracting or relaxing. This feature enables humans to accommodate for an in-focus image at different depths. The last refraction occurs on the interfaces between the lens and vitreous and finally an image is formed on the retina. From there, photoreceptors including cone cells and rod cells convert light intensity into electrical impulses, which are unevenly distributed on the retina. Cone cells concentrate most in the central region of the retina called the macula, which spans about 5 mm. Visual acuity refers to the ability for a human eye to resolve small features. The fovea, in the center of macula, has the maximum visual acuity due to its highest photoreceptor density, covering only 2–3° [13]. For a 20/20 vision, an eye should be able to resolve detail as small as 1 arcmin, or, in other words, the angular resolution is 60 pixels per degree (PPD) in the fovea. Outside the fovea, visual acuity declines rapidly in the rest region of macula. Rod cells can be found away from the macula, responsible for scotopic vision with low-resolution perception. In AR/VR systems, both the imaging quality of optics and the resolution density of light engines affect the

Figure 1

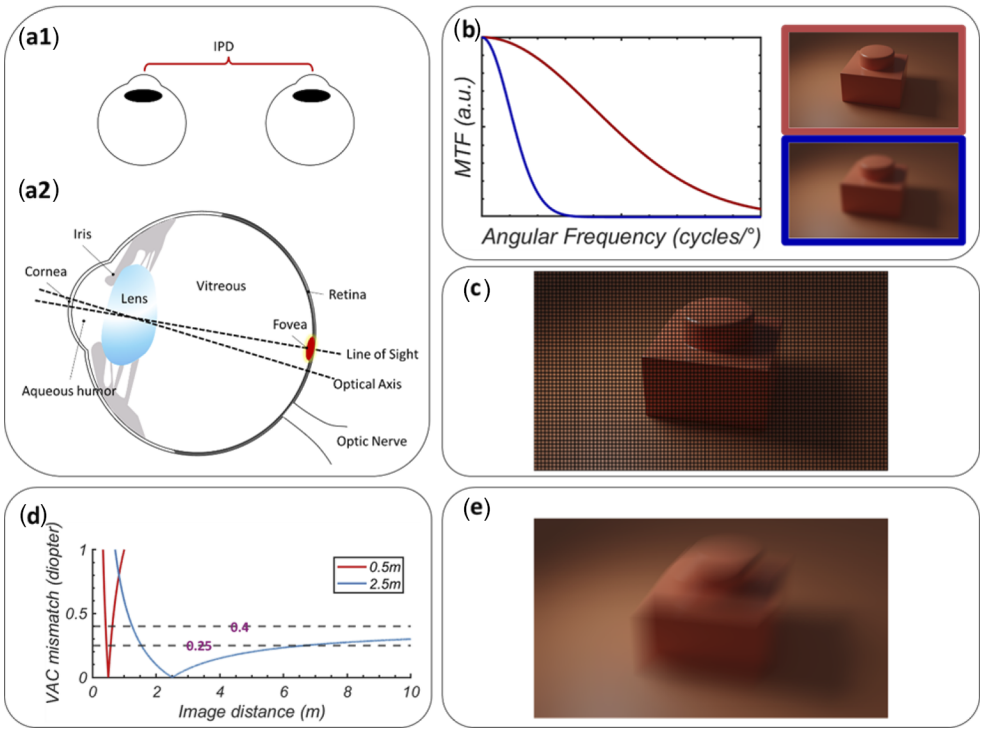

(a1) Illustration of interpupillary distance (IPD) in humans. (a2) Schematic of a simplified human eye model. (b) Effect of excellent (red) and poor (blue) MTF to display quality. (c) Displayed image with screen door effect. (d) Vergence-accommodation tolerances at a near (0.5 m) and far (2.5 m) distance. (e) Displayed image with motion blur.

final image quality on the retina. The modulation transfer function (MTF) [25] is an indicator of how well an imaging system can reproduce fine details and sharp edges as shown in Fig. 1(b). MTF shows the contrast performance as a function of angular or spatial frequency, and it decides the spatial frequencies which the display and following optics can deliver to an eye. The perceived PPD may be lower than expected if the optics between the display panel and eyes shows a poor MTF. Failing to satisfy such a high PPD leads to the screen door effect [26], where a mesh pattern is overlaid over the image, like seeing the world through a screen door (Fig. 1(c)). The "screen door" is essentially the pixel structure of a display panel as the fill factor is not 100% and only part of pixel is emitting, transmitting, or reflecting light. Here, we present the second requirement for an advanced display light engine: high resolution density.

The image perceived by human eyes is not a flat 2D image but with 3D sense. Depth cues exist in the HVS [27]. Physiologically speaking, the depth cues include accommodation, convergence, and motion parallax [28]. On the one hand, the lens in an eye can dynamically accommodate its shape as well as optical power to form clear images at different depths. On the other hand, with binocular vision, each eyeball will rotate to converge its line of sight on the focused object. Thus, this convergence angle provides depth information to the visual cortex. These two depth cues, vergence and accommodation, are closely linked within the HVS and are intrinsically matched with each other in reality. The ability for the human eye to perceive depth variation is called stereo acuity. The HVS is not sensitive to the depth change caused by absolute distance difference, but by diopter difference [29,30]. This feature indicates that the HVS is more sensitive to the depth variation at a close range, usually referred to as "one-arm's

length," which is about 30–50 cm. For objects at further range, stereo acuity is not sensitive. When looking at a fixed focus stereo display, a user is forced to accommodate to a single distance to obtain a clear image, but stereoscopic disparity tells eyes to make a vergence for objects at different depths, introducing vergence–accommodation conflict (VAC) [31,32]. The VAC tolerance range for a near and far distance is illustrated in Fig. 1(d). If the image plane is set at 2.5 m away from a user, then the acceptance region covers about 5 m, from 1.5 m to 6.7 m, if the VAC tolerance limit is set to 0.25 diopters. For a higher VAC tolerance limit, say 0.4 diopters, then for 1.25 m to infinity, there is no VAC issue. However, for a closer imaging plane at 0.5 m, the acceptance region will be much narrower due to drastic diopter variation. Integral imaging displays [33,34] and holographic displays [14,35] are proposed to reproduce the light field by ray approximation or a complete wavefront. Maxwellian displays [21,36] avoid VAC by creating a large depth of focus image and may introduce natural blur through image rendering. In light engines with a high frame rate, accompanying an active combiner, more focal planes [37] can be created statically or dynamically at near depth to mitigate the VAC issue. In addition, motion artifacts [38] in nature usually happens when an observed object or an observer's eye is moving too fast, resulting in an inability to resolve details, as depicted in Fig. 1(e). A nature-looking movement requires some degree of motion blur, but if the response time [39] of the hold-type display is too high [40], extra undesired motion artifacts may be caught by the users. Motion artifacts may also occur when the head moves too fast, and the displayed content is not updated synchronously. This is usually described as motion-to-photon latency [41,42]. Fast sensors and a better video-processing pipeline could also diminish this nausea. Based on this discussion, we present the third requirement for an advanced display light engine: fast response time.

The HVS has a huge dynamic range, from the dim starlight at 10^{-6} nits to bright sunlight at 10^{8} nits, as shown in Fig. 2(a). In dark light environments, or at scotopic light levels, it is mainly the rod cells that are responsive for luminance ranging from 10^{-6} to 10^{-2} nits, whereas cone cells are active for photopic light levels (10–10^{8} nits). Between these two ranges (mesopic range), both rod and cones are involved in the sensing. The difference in scale between the darkest and brightest objects a human eye can perceive spans 14 orders of magnitude. At one time, the HVS can only perceive a subset of such range, say about five orders of magnitude. The traditional standard dynamic range (SDR) displays cover 3 orders, but HDR [43,44] displays aim to match the steady dynamic range of the human eye, allowing objects to be represented closer to their nature. Human eyes are more sensitive to the illuminance variation at low light levels, so high contrast ratio, lower dark level, and more bits at low gray levels are preferable in HDR displays. For AR applications, the highest illuminance of a HDR display is vital for outdoor scenarios. The ambient contrast ratio (ACR) [45] should achieve at least (3:1) for an acceptable readability. Considering the ambient illuminance is 3000 nits in a sunny day, the display needs to deliver at least 10,000 nits, ignoring the optical loss. If methods such as exit pupil expansion (EPE) are applied to enlarge the eyebox, an AR device will demand a much higher brightness from the display panel. Due to limited battery capacity, the optical efficiency of the overall system should be high. Given that ambient light is fully blocked in VR headsets, 150–200 nits of brightness received by human eye is acceptable after considering the optical losses. Here, we present the fourth and fifth requirements for an advanced display light engine: HDR, high efficiency and peak brightness, and long lifetime.

2.3. Eyebox and FoV

In HVS, an entire field of view (FoV) spans more than 200° horizontally (H) and about 130° vertically (V), whereas the binocular overlap is about 120° H, as shown

Figure 2

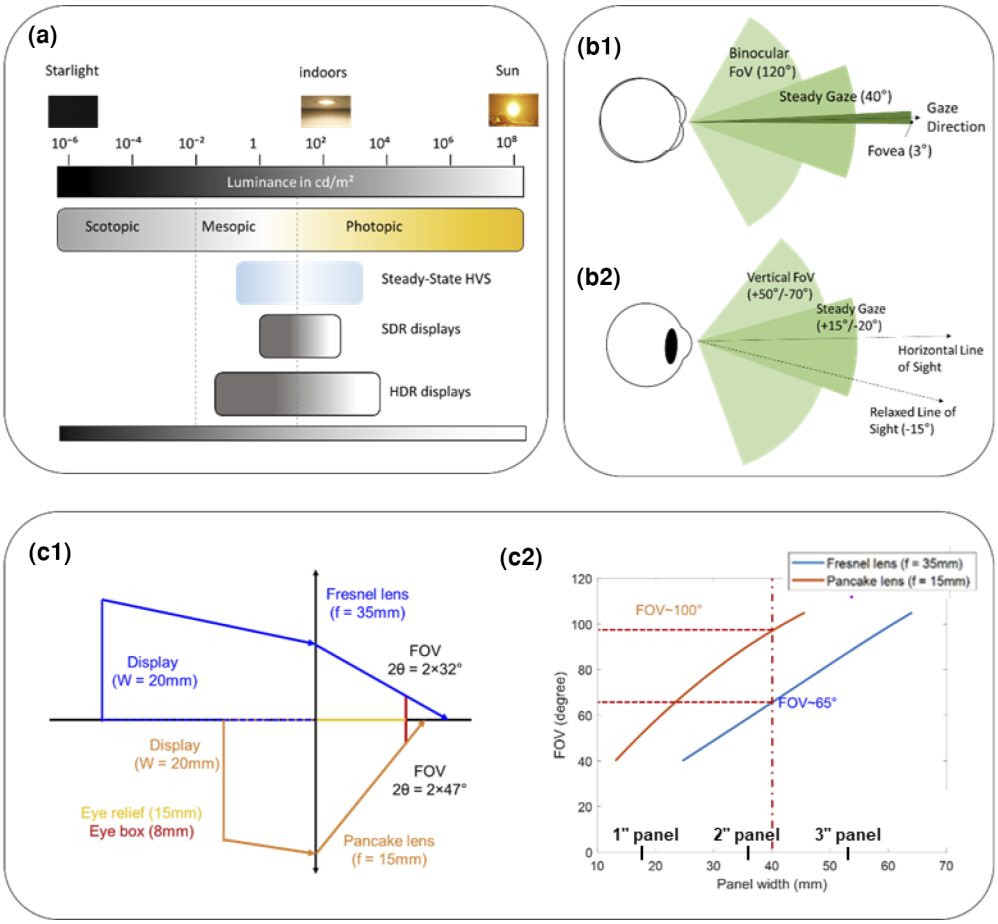

(a) Dynamic range of the human visual system. (b1) Horizontal human vision FoV. (b2) Vertical human vision FoV. (c1) Schematics of FoV calculations in Fresnel and pancake VR systems at a given display panel width, eye relief, and eyebox, assuming the optical power is provided by a singlet lens. (c2) Relation between FoV and panel width in Fresnel- and pancake-lens-based VR systems.

in Fig. 2(b1). When eyes are at a relaxing state, steady gaze is possible for a FoV of ±20° H and +15°/–20° V, without producing any eye strain. Compared with horizontal FoV, the vertical FoV is asymmetric because the relaxed line of sight is 15° below the horizontal line of sight, as depicted in Fig. 2(b2). Figures 2(b1) and 2(b2) also show capabilities of each part of FoV in the HVS. The eyebox [46] is a physical 3D region where the whole FoV can be viewed without vignetting. In an AR/VR device, this 3D volume is closely related to the exit pupil size of the optical combiner. Although the eyebox is defined in terms of volume, it is usually expressed as a few millimeters horizontally. A larger eyebox would allow an AR/VR device to be set up faster and better account for variations in human IPD and positioning of the head. Eye relief [47] refers to the distance from the last optical surface to the best viewing spot. A shorter eye relief generally increases the perceived eyebox size but may prohibit users from wearing glasses if needed. In addition, due to the conservation of Lagrange invariant and étendue in an imaging system, a trade-off exists between the eyebox and FoV. In AR devices, pupil replication [36,48] and pupil steering [49] techniques are proposed to mitigate the limited eyebox. Moreover, in VR devices, a sufficiently large panel size is required to support the required FoV with acceptable eyebox. Assuming the eyebox size is 8 mm and eye relief is 15 mm (Fig. 2(c1)), Fig. 2(c2) illustrates the relation

between FoV and panel size in a Fresnel lens or folded-optics-based (often called a pancake lens; see Sec. 3.1) VR system, under the simplification that optical power is provided by an ideal singlet lens. In Fig. 2(c2), a larger panel size generally leads to a wider FoV. Here, we label the panels with diagonal dimensions of 1, 2, and 3 inches for reference. Furthermore, at a given panel width of 40 mm (vertical dashed lines), the VR system (pancake architecture) with a larger optical power exhibits a wider FoV (100°) than the VR system (Fresnel architecture) with a lower optical power (FoV = 65°).

2.4. Eye Safety

Cone cells on the retina have different spectral sensitivities and are generally labeled by their peak wavelengths as short (S), medium (M), and long (L) cone types. According to the trichromatic theory, the same color can be perceived by a human eye even if the input light spectrum is different, as long as the tristimulus values remain the same. This gives some freedom on the choice of the light sources in AR/VR displays to reproduce the desired colors. However, the designer must take good care of spectrum brightness perceived by human eyes, following the eye safety regulation. For example, at the same brightness, deep blue is more harmful to eyes than light blue. Nowadays, mainstream light sources are LED (both inorganic and organic) and lasers. These high-brightness emissive light engines could be harmful to the user's eyes for two possible reasons: (1) they may contain some ultraviolet (UV) or deep blue component, such as deep-blue-pumped quantum dot (QD) color conversion layer; and (2) the light source could be very strong to keep a reasonably high ACR for outdoor applications.

3. AR/VR ARCHITECTURES

3.1. VR Architecture

Most current VR devices adopt a simple optical architecture combining a light engine and a collimation lens with positive optical power, as Fig. 3(a) depicts. Usually, some optical power is provided by a Fresnel lens and therefore the collimating lens is a hybrid Fresnel refractive lens. In addition, a hybrid diffractive and refractive lens can also be applied to reduce lateral chromatic aberration [50]. To further reduce form factor, the optical path can be folded by introducing polarization sensitive optical elements, such as a reflective polarizer (RP) or a cholesteric liquid crystal (CLC) lens. This optical design is usually referred to as "pancake" optics [51]. A typical pancake optics design is plotted in Fig. 3(b).

Figure 3

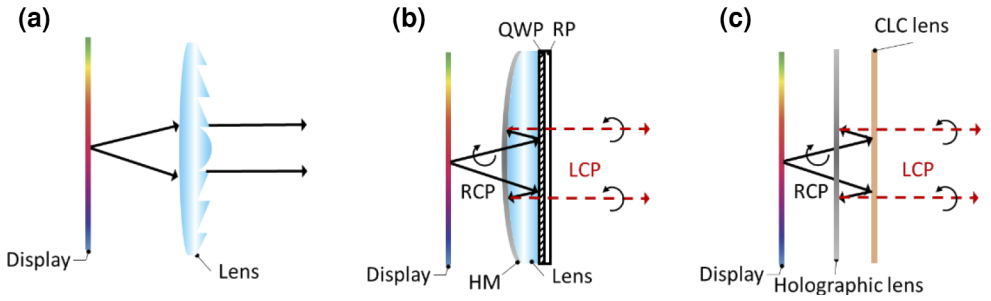

(a) Sketch of the optical architecture of a simplest VR system including a light engine and a hybrid Fresnel refractive lens. (b) Sketch of a pancake VR system consisting of a light engine, a half mirror (HM), a refractive lens, a QWP, and a reflective polarizer (RP). (c) Sketch of an ultra-slim pancake VR system consisting of a holographic lens and a CLC lens.

The system is composed of five parts: a light engine, a half mirror (HM), a refractive/Fresnel/hybrid lens, a quarter-wave plate (QWP), and a RP. Assuming the input light polarization is right-handed circular polarization (RCP), after passing through the QWP and RP, the polarization state remains unchanged. Upon reflection on the HM, the reflected light is switched to left-handed circular polarization (LCP) and passes through the QWP and RP. The optical path between the HM and RP is tripled, but the maximum efficiency of the optical combiner is only 25% in theory. In an even more compact pancake VR design (Fig. 3(c)), the HM and lens could be replaced by a volume holographic lens [52] and the QWP and RP can be replaced by a CLC lens [53]. Although all kinds of light engines can work in the VR systems, active-matrix LCDs and OLED displays are currently the mainstream choices.

3.2. AR Architecture

AR architectures are often categorized by their combiners. Based on where the incident light propagates, there are three types of optical combiners: free-space combiners, freeform prism combiners, and waveguide combiners.

3.2a. Free-Space Combiner

The simplest free-space combiner is a 50/50 beam splitter. The output light from an optical engine is reflected to the eye while the ambient light from the real world passes through the beam splitter and is combined with the display light, as shown in Fig. 4(a). Some optical power can be added to the partial reflector by making it a curved surface [54] (Fig. 4(b)), enabling a large FoV, but this design suffers from image distortion because all the optical power is provided by a single surface and the form factor is large. The birdbath optics [55] in Fig. 4(c) folds the optical path for a smaller form factor and introduces additional optical elements for aberration correction. These architectures serve as traditional imaging systems, imaging from a "real" plane of a light engine to a "virtual" plane. Then this "virtual" plane is imaged by an eye to the retina. Thus, display panels such as OLED, μLED, DLP, and LCOS are preferred. In a Maxwellian display [21,36,48,49,56], the combiner reflects the image from the light engine to the eye pupil, as shown in Fig. 4(d). As the focusing spot is much smaller than the eye pupil, a clear image with infinite depth of focus can be formed on the retina, no matter what the optical power of the eye is. However, the eyebox is limited in Maxwellian displays, thus pupil steering or pupil duplication is often required to enlarge the eyebox. A LBS display [57] is a natural point source and, thus, can be applied directly to Maxwellian displays. A spatial light modulating display such as LCOS or DLP [35] can also be used in Maxwellian displays if illuminated by a collimated light, as Fig. 4(e) shows. Although self-emissive display panels, such as μLED and μOLED, relayed by a 4-f system with an aperture stop can also be employed in Maxwellian displays, their light throughput is relatively low.

3.2b. Freeform Prism and Waveguide Combiners

In both freeform prism combiners [58] and waveguide combiners [45], the imaging light propagates in either prism or waveguide by total internal reflection (TIR), as depicted in Figs. 4(f) and 4(g), respectively. The optical path is folded in a prism combiner and each surface is carefully designed for achieving an excellent image quality. The most obvious feature in a waveguide combiner is the EPE process, which breaks the étendue limit and effectively increases the eyebox size. The upper limit of the FoV is determined by the waveguide refractive index, which is about 70° for a $n = 2$ glass. Usually, for a display panel, the output image is first Fourier transformed to far field, converting image information from the spatial to the angular domain. However, the LBS display does not require such a conversion. Then, display light is coupled into a

Figure 4

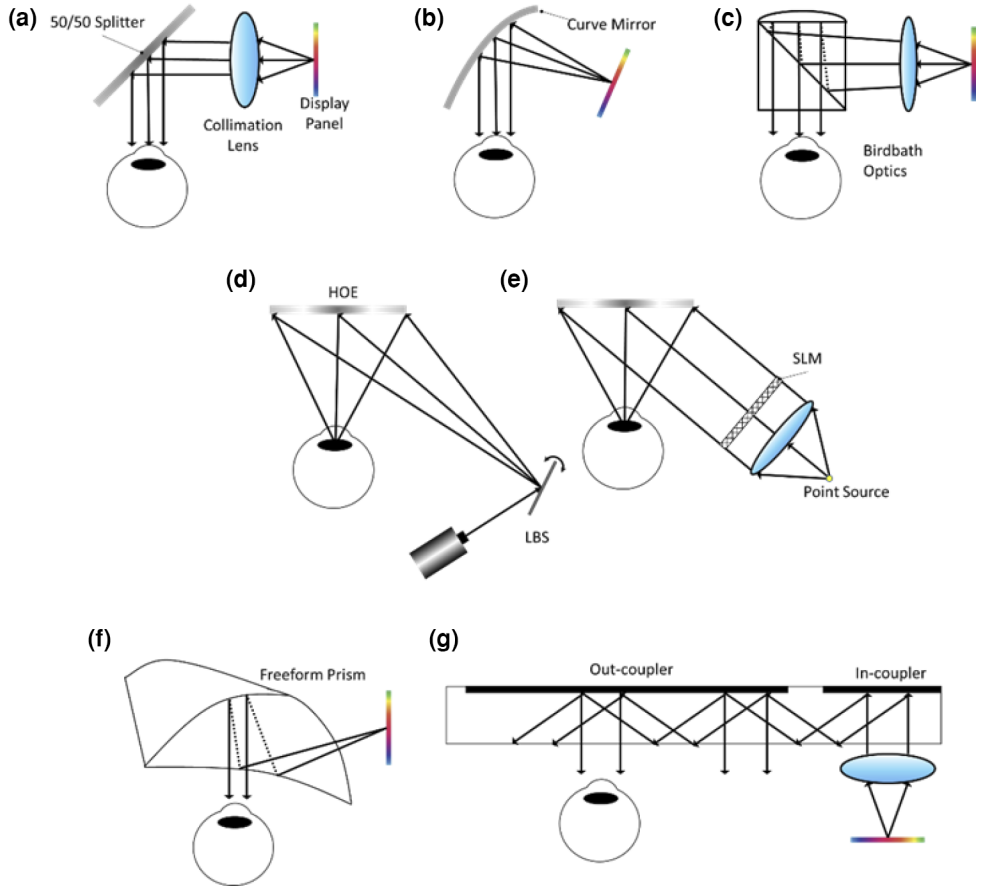

(a) A 50/50 beam splitter as a combiner. (b) Single reflective curved surface combiner. (c) Birdbath design combiner with a folded optical path. (d) Maxwellian display based on a LBS. (e) Maxwellian display based on a SLM. (f) Freeform prism combiner. (g) Waveguide combiner consisting of two reflective-type diffractive gratings. HOE, holographic optical element; SLM, spatial light modulator.

waveguide, propagates through the TIR process, and finally is outcoupled into human eyes. The in- and outcoupler can be a prism, a diffractive grating, or partial reflective mirrors.

4. LIGHT ENGINES FOR AR/VR DISPLAYS

4.1. Light Modulation Display

Here, a light modulating display refers to a display that utilizes mechanisms to modulate the polarization, propagation direction, or phase of the imaging light. The modulation of polarization or propagation direction can be converted into amplitude modulation, and the phase modulation can be used for holographic displays. Presently, commercially available light modulating displays mainly include LCDs, LCOS microdisplays, and DLP microdisplays. Recently, transmissive thin-film transistor (TFT) LCDs with resolution density of 2016 pixels per inch (PPI) have been demonstrated by Innolux (in Touch Taiwan 2022) for VR applications. On the other hand, the reflective LCOS and digital micromirror device (DMD) driven by silicon backplane can achieve a higher resolution density (>6000 PPI) and smaller form factor for AR applications.

Figure 5

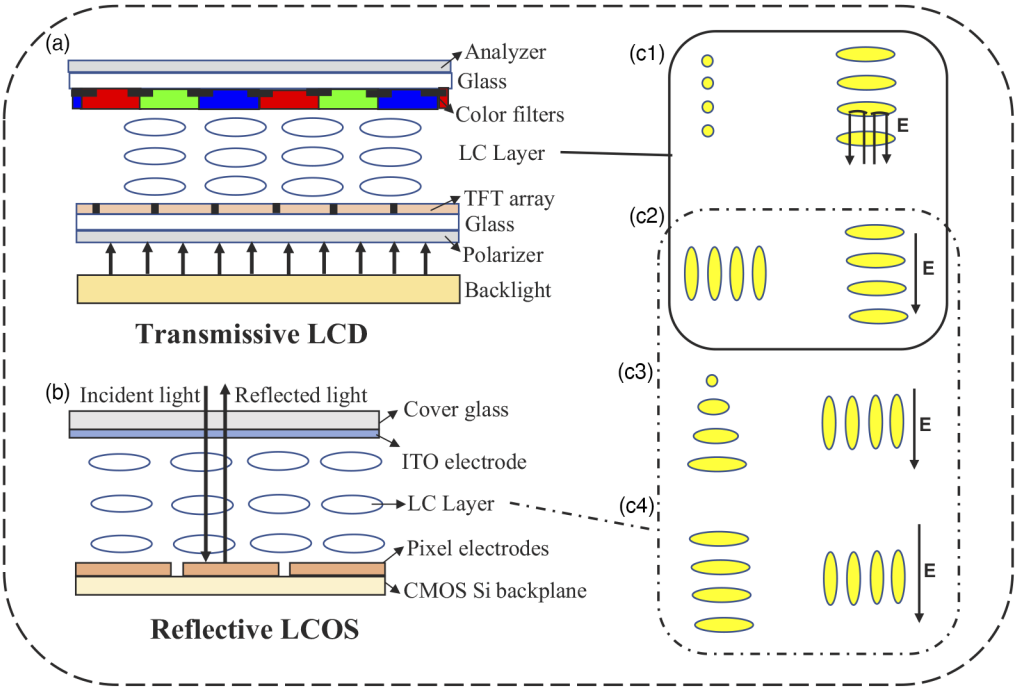

Schematics of (a) LCD and (b) LCOS: (c1) FFS mode, (c2) VA mode, (c3) MTN mode, and (c4) HG mode.

For a light modulation display, the light source also plays a significant role affecting the final performances of light engines. LEDs and lasers are two widely used light sources. For LCDs, the LEDs used in the backlight module can be further categorized into conventional large-size LEDs and mini-LEDs. Mini-LEDs can provide a much higher dynamic range than conventional LEDs through local dimming effect, but the halo effect should be minimized. The lasers used in backlight modules can widen the color gamut and theoretically save about 70% of the optical losses from color filters and polarizers. However, in comparison with LED backlights, laser sources generally require a larger space to homogenize the brightness distribution. In addition, during the homogenization process, the polarization property of the lasers may be deteriorated. As a result, the optical efficiency improvement is often lower than the theoretical value. Furthermore, from the perspective of light source efficiency, the wall plug efficiency of the lasers is lower than that of LEDs. For the light modulated AR displays (LCOS and DMD), due to the smaller panel size, using a laser as light engine may not suffer from the severe homogenization issues that LCDs do. Moreover, compared with LEDs, almost all the light from a laser with a small etendue can impinge on the panel, resulting in a much smaller optical loss. However, the speckle issue needs to be addressed by methods such as electromechanical de-speckling and AC driving.

4.1a. LCD

Liquid-crystal-based displays consist of transmissive LCDs (Fig. 5(a)) and LCOS microdisplay (Fig. 5(b)). An active-matrix LCD is composed of a backlight module, a TFT array, a LC layer, color filters, and crossed polarizers, as schematized in Fig. 5(a). The backlight module provides a uniform luminance distribution, and the pixelated LC cell, modulated by the TFT array, determines the transmittance of each subpixel for gray-scale images [59]. In LCD panels, two commonly used operation modes have been developed, depending on the molecular alignment and the electric field direction:

(1) fringe-field switching (FFS) mode (Fig. 5(c1)) [60] and (2) vertical alignment (VA) mode (Fig. 5(c2)) [61]. Each mode has its own pros and cons and has been discussed extensively in several review papers [6,62,63]. Thus, we only briefly introduce their device configurations and operation principles, and in the following section, we focus on the recently developed LC modes, which meet the requirements of AR/VR display applications, such as fast response time, high transmittance, and acceptable viewing angle. For the FFS mode, the LC directors are homogenously aligned, and the lateral electric field reorients the LC directors mostly in-plane. According to the in-plane switching, the FFS LCDs feature a small angular color shift and contrast roll-off under oblique viewing angles. Moreover, the built-in storage capacitor formed in FFS mode is more suitable for high PPI display (VR display) because of its larger aperture ratio. However, the slow response time caused by the small twist elastic constant of traditional FFS mode should be overcome to suppress the motion image blurs for VR applications. For VA mode, the LC directors are initially aligned in vertical direction, so the incident linearly polarized light is not modulated when traversing through the LC cell and is blocked by the crossed analyzer. As the voltage exceeds a threshold, the negative dielectric anisotropy LC molecules bend against the longitudinal electric field, allowing the incident light to pass through the crossed polarizers. The intrinsic high contrast ratio of VA mode is preferred for providing HDR images. However, VA mode is plagued by a limited viewing angle, so the multi-domain structures, such as 4, 8, and even 12 domains, have been proposed to expand its viewing angle [64]. However, for VR applications, the viewing angle requirement is much more relaxed than the traditional direct-view displays, such as TVs. Therefore, for VR applications, the multi-domain structure of VA LCD has more degrees of freedom to balance the viewing angle, transmittance, and response time. It is worth mentioning that, due to the scattering from the TFT array, the LC layer, and the color filter, the contrast ratio of LCDs is limited by around 2000:1 and 5000:1 for the FFS mode and VA mode, respectively. Therefore, the grayish dark state of the LCDs may severely disrupt the immersive experience of the users. Fortunately, mini-LED backlight can help the LCD achieve a much higher dynamic range via local dimming. As a result, the mini-LED backlit LCD is a good candidate for advanced VR headsets due to its higher contrast ratio, higher bit depth, and lower power consumption.

4.1b. LCOS

Compared with transmissive TFT-LCDs, LCOS adopts silicon backplane to achieve a higher resolution density and a reflective operation mode to increase the fill factor and frame rate. The first attempt to drive LCs using a silicon backplane was made by Ernstoff *et al*. in the early 1970s [65]. Dynamic scattering electro-optic effect was initially used but not appropriate for phase modulation due to the charge leakage. Later the LCOS devices based on the field effect of nematic LCs and ferroelectric LCs were reported [66], respectively. A typical LCOS device consists of a CMOS backplane, metal pixel electrodes, a LC layer, an indium tin oxide (ITO) common electrode, and a cover glass, as shown in Fig. 5(b). A set of red, green, and blue (RGB) LEDs is employed as a light source to illuminate the LC panel uniformly and the full color image is generated via field sequential colors (FSCs). To obtain coaxial RGB beams from the separated RGB light sources (LEDs or lasers), dichroic mirrors are usually employed. When the incident light travels through the LC layer, the intersection between the transverse plane and the refractive index ellipsoid yields two eigenwaves with two eigenpolarizations and normal indices. One eigenwave experiences an angle-dependent refractive index (n_e), and the other experiences a constant refractive index (n_o). Owing to the birefringence ($n_e - n_o$), effect, the incident polarization is decomposed into two eigenpolarizations, and the accumulated phase retardation between the

two eigenpolarizations can modulate the incident polarization. Polarization modulation can be converted into amplitude modulation through a polarizing beam splitter (PBS) or a circular polarizer. However, if the incident polarization is parallel to the eigenpolarization with a variable refractive index, the incident polarization remains unchanged, and the pixelated phase change depending on an applied voltage can be obtained. In this way, pure phase modulation is achieved.

To date, three major LC modes have been widely adopted in LCOS devices: VA mode [61] (Fig. 5(c2)) and mixed-mode twisted nematic (MTN) [67] (Fig. 5(c3)) are mainly used in amplitude modulation, and homogenous (HG) alignment (Fig. 5(c4)) is dominantly employed in phase modulation. For the VA mode, without any applied voltage ($V = 0$), an excellent dark state and high contrast ratio can be obtained, which is a major advantage of the VA mode. In the MTN mode, the LCs are twisted from the bottom substrate to the top substrate with 90° twist angle. The angle between the polarizer's optic axis and the front LC directors is defined as β, which is set at 20° to maximize the reflectance of the 90°-MTN cell. MTN exhibits a faster response time, wider viewing cone, and weaker fringing field effect (FFE) than VA, but its contrast ratio (~1000:1) is lower. Homogeneous alignment is not suitable for amplitude modulation due to its strong wavelength dependency and narrow viewing angle, but it is widely used in phase modulation because of its fast response time.

4.1c. DLP

A DMD is a microelectromechanical system (MEMS) device [68,69] developed by Texas Instruments in 1987. The DMD originated from the deformable mirror device in 1977, and then was commercialized in DLP in 1996. At the heart of the DMD technology are a dense array of micromirrors that can be electrostatically rotated to an on or off state. Each DMD pixel consists of the micromirror, yoke and hinge, metal standing, and dual CMOS memory. Figure 6(a) illustrates that the micromirror is attached by a via to a yoke with a torsion hinge [70]. The two electrodes steer the micromirror to the two operational positions (Fig. 6(b) [71]) by electrostatic forces. One electrode addresses directly the micromirror, and another controls the yoke. Dual CMOS memory is used to store the binary state of the micromirror, and a mirror clocking pulse will transfer the stored memory state to the mechanical position of the micromirror. Due to the binary module, gray levels are usually generated by pulse width modulation (PWM). To create color images, FSC is adopted. In contrast to LCOS devices, high-speed response and polarization insensitivity are two main characteristics for DMDs.

In the past two or three decades, the DMD technology has advanced in various aspects including the mirror tilt angle, mirror pitch, optical/system efficiency, and contrast ratio. The tilt angle has been continuously improved from initial ± 10°, ± 12°, to current ± 17°. Due to enlarged tilt angles, the illumination cone angle at the mirror and the étendue of the illumination system are increased, contributing to a higher system efficiency. The mirror pitch has been reduced from the initial 17 μm to current 5.4 μm realized in the Texas Instruments DLP3010, enabling a high-resolution DMD. The optical efficiency of the DMD depends on several factors including the window transmission, fill factor, diffraction effect, and mirror reflectance. To calculate the system-level efficiency, we should consider more factors such as étendue mismatches between the illumination and projection system, which are described in more detail in Sec. 5.2. As for contrast ratio, it cannot be described for the DMD itself, which is different from LCOS. The system contrast ratio can be defined once the projection lens or system aperture stop constraining a solid angle is considered. The dominant factors affecting the system contrast ratio consist of illumination angle, mirror gap, numerical aperture, and coating quality [72]. Illumination angle and surface coating

Figure 6

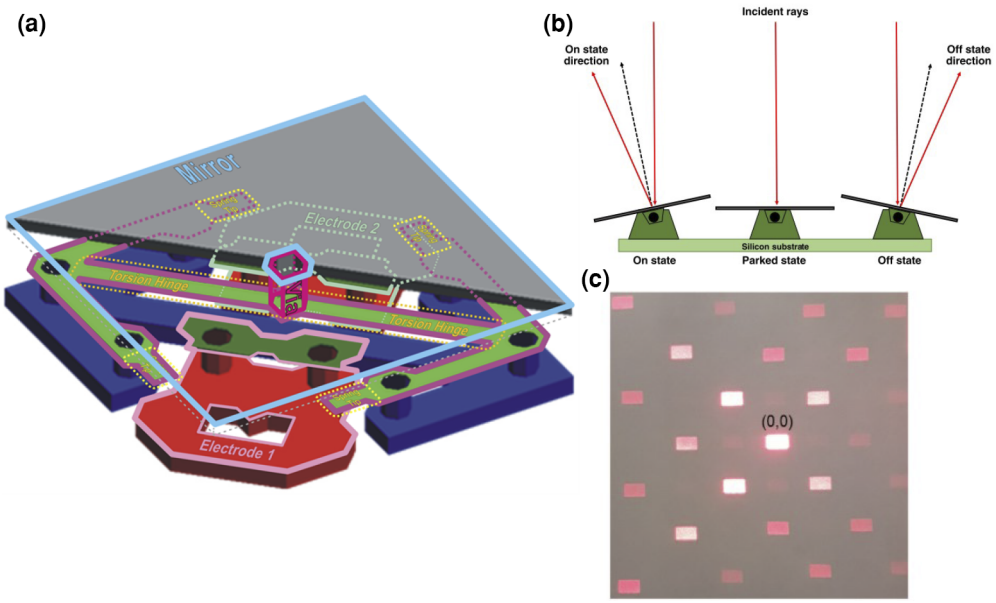

Schematic of (a) a single DMD pixel and (b) two DMD pixels with opposite statuses and one micromirror at the parked state. (c) Diffraction pattern from the DMD at normal incidence with all mirrors in the on state. (a) Reprinted with permission from [70]. © Texas Instruments. (b) and (c) Reprinted with permission from Scholes *et al*., Opt. Eng. **59**, 041202 (2019) [71]. © 2019 SPIE.

can affect the distribution of reflected light and scattered light, and mirror gap can lead to diffracted light. Numerical aperture determines how much of the reflected, scattered, or diffracted light is collected by a projection lens and thereby plays a significant role in influencing system contrast ratio as well. Figure 6(c) shows the far-field diffraction pattern from the DMD at normal incidence when all mirrors are in the "on state" [71]. The rectangle marked (0,0) represents the zeroth-order diffraction, whereas the remaining rectangles represent other diffraction orders that may cause a loss of efficiency and a reduction of system contrast ratio.

4.2. Self-Emissive Displays

4.2a. OLED

The basic structure of a low-voltage OLED device was invented in 1987 by Tang and VanSlyke [2]. The electrons and holes are injected to the organic emission material for light emission. However, at the initial stage, the OLED efficiency is limited by the low quantum efficiency, carrier injection efficiency, and light extraction efficiency (LEE). In the past few decades, different types of emission mechanism (fluorescent, phosphorescence, triplet–triplet fluorescent, and thermally active delayed fluorescent) have been developed to significantly boost the quantum efficiency [73–76]. In addition, by applying doping techniques in the hole and electron injection layers, the carrier injection efficiency is enhanced to almost 100%. Nowadays, the OLED efficiency is mainly limited by the low extraction efficiency resulting from the TIR at the interfaces between organic material, glass, and air [77,78]. From the perspective of display configurations, an OLED display consists of two parts: (1) OLED devices (front plane), which can be patterned red, green, and blue (RGB) OLED devices (Fig. 7(a)) or white OLED (WOLED) with RGB color filters (Fig. 7(b)); (2) electrical driving (backplane) which can be TFTs fabricated on the glass substrate or the complementary metal oxide semiconductor (CMOS) on the silicon backplane. According to two types

Figure 7

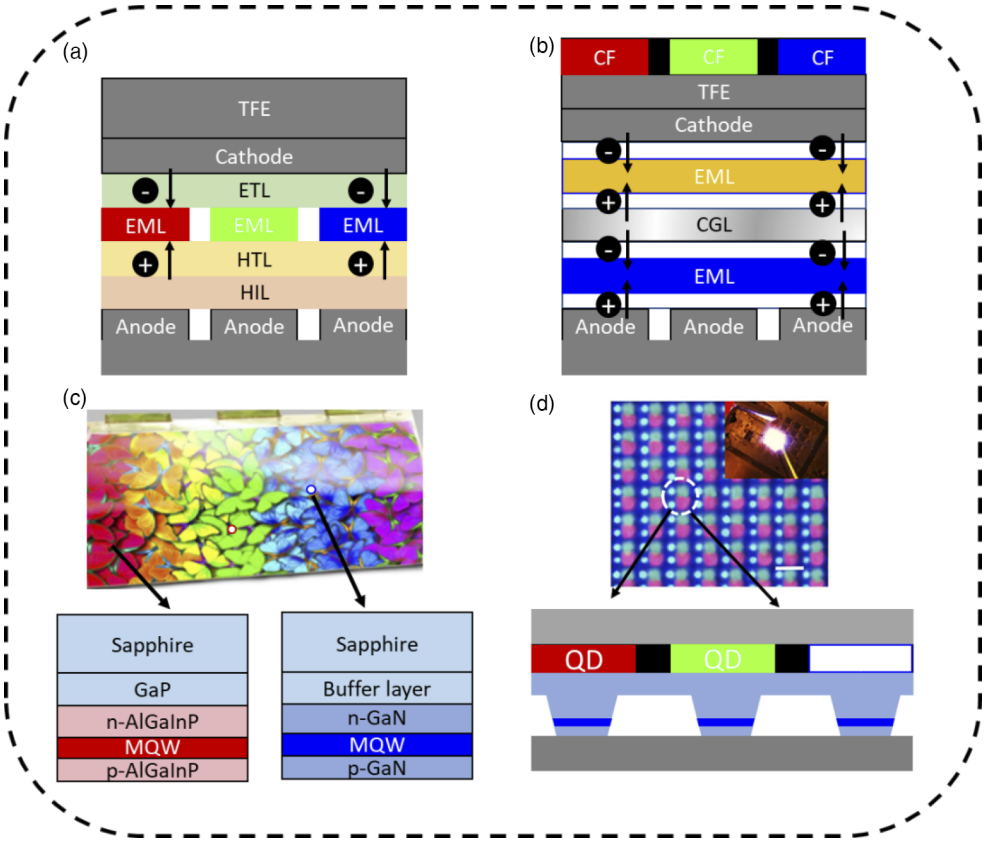

Schematics of (a) RGB OLED, (b) tandem WOLED, (c) RGB μLED, and (d) color conversion μLED display. (c) Reprinted from Lee *et al.*, J. Soc. Inf. Disp. **29**, 360–369 (2021) [79]. Copyright Wiley-VCH Verlag GmbH & Co. KGaA. Reproduced with permission. (d) Reprinted from [80] under a Creative Commons license.

of front planes and two types of back planes, there are four combinations for achieving a full-color OLED display, but each has its own pros and cons.

For an OLED display, the brightness of each pixel is determined by the driving current. Therefore, the complicated driving circuits, which consist of eight transistors, are proposed to drive the OLED device to a precise gray level. Compared with TFT, CMOS with a higher carrier mobility and narrower linewidth can minimize the occupied layout area of the driving circuit and support a higher resolution density. However, due to the fabrication process and cost, the panel size of OLED-in-silicon is normally limited to about 1.5 inches [81]. In general, the patterned RGB OLED devices are fabricated by material depositions through a fine metal mask (FMM) with resolution density below 600 PPI, which is inadequate for near-eye headsets [82]. Therefore, an advanced patterning method for the organic material is required. In contrast, for white OLED with RGB color filters, the pixel pitch is defined by the resolution density of color filters, which can be fabricated with high resolution density by conventional photolithography methods [83]. However, the color filters absorb about two-thirds of the emission light from the white OLED, resulting in a lower optical efficiency. In addition, to generate white light, the tandem WOLED with two or more stacked emission layers connected in series with charge generating units is widely applied. To design an advanced WOLED device, it is important to balance the driving current density, current efficiency, and peak brightness between RGB subpixels because the weakest subpixels restrict the overall display performance [84]. For example, in the

two-stacked (blue florescent and yellow phosphorescent) WOLED, the blue OLED [85] has a lower current efficiency that limits the peak brightness and lifetime of the WOLED displays. As a result, tandem WOLEDs with more than two stacks are also proposed to balance the performance between RGB subpixels, but at the expense of higher driving voltage and higher fabrication cost.

4.2b. μLED

The GaAsP-based red LED was first invented by Holonyak and Bevacqua in 1962 [86]. Afterwards, different color LEDs were subsequently introduced but the commercialization of blue LEDs faltered for decades until the 1990s, when high-power blue LEDs were developed by Akasaki, Amano, and Nakamura (see Ref. [87]). After that, high-power and high-efficiency LEDs have significantly replaced traditional lamps as illuminating systems for light-modulating display systems, such as LCDs, and projection displays. Millimeter-scale LED chip sizes are used to provide high-brightness emission, and the emitted light is further modulated through high-resolution density LC panels or DMD to display vivid images [88]. In the early 2000s, the LED chip size as small as 10 μm has been demonstrated [89]. Therefore, high-resolution-density LED arrays can directly generate decent images without the need of an additional light-modulating element. Like an OLED display, the active-matrix μLED also requires front and back planes. For the front plane, it could be an array of RGB μLED chips (Fig. 7(c)) [79] or an array of blue μLEDs with a patterned QD color conversion layer (Fig. 7(d)) [80]. However, unlike OLEDs which can be fabricated directly on a glass substrate, the μLED chips are first fabricated on a specific substrate, such as sapphire for green and blue LEDs and GaAs for red LEDs, and then transferred to a back plane. Because RGB LED chips are fabricated on different substrates, they need to be picked and placed onto the designated positions of a glass substrate. For a 4K2K display, there are 24M subpixels, i.e., 24M μLED chips need to be transferred. The fabrication yield and defects repair jointly affect the cost. Recently, various pick-and-place techniques based on elastomer stamping, electrostatic/electromagnetic transfer, laser-assisted transfer, or fluid self-assembly are proposed to improve the manufacturing time and yield [90]. However, restricted by the transfer technologies the resolution density of these methods is normally below or around 1500 PPI. At 2021 SID Display Week, PlayNitride demonstrated a full-color RGB μLED prototype with 1411 PPI by the pick-and-place mass transfer technology. To achieve high-resolution density μLED arrays, wafer-level transfer approaches have been proposed: flip-chip bonding and wafer bonding [91], which can work at subpixel pitches less than 3 μm. However, for the monolithic integration methods, the display panels only support a single color. Therefore, to generate full colors, the color conversion layer is widely used on top of blue LED array or using an X-prism [92] to combine the images from three single-color R/G/B μLED panels. At 2022 SID Display Week, PlayNitride demonstrated a full-color μLED prototype (panel size 0.49-inch, resolution 1920×1080, pixel size 2.5 μm, and pixel pitch 5.6 μm) with 4536 PPI using subpixel rendering arrangement and QD color conversion layer. At 2020, Jade Bird Display demonstrated a full-color μLED prototype (panel size 0.31-inch, resolution 1280×720, and pixel pitch 5 μm) with 5000 PPI using an X-prism and three single-color R/G/B μLED panels. For the back plane, similar to the OLED devices, both TFT and CMOS can be employed to precisely control the driving current level or light emitting time to accurately modulate the brightness of the μLED chips.

4.3. Light Scanning Displays

So far, we have introduced two kinds of display engines used in AR/VR, which are panel-based microdisplays composed of a two-dimensional (2D) pixel array. In this section, LBS microdisplays are introduced. In contrast to panel-based microdisplays,

LBS exhibits the advantages of small size, high brightness, and high contrast ratio. Small size arises from the fact that they are not limited by the étendue conservation, because there is no object plane unlike a panel-based microdisplay. However, the major drawbacks of LBS microdisplays are low resolution and limited frame rate because each individual pixel is displayed in a time-sequential manner, analogous to raster scan. Moreover, laser speckles should be suppressed for practical applications.

A LBS system is composed of a laser module and a beam scanner. A laser module usually consists of laser sources (red, green, and blue laser diodes), collimation optics, and a dichroic beam combiner. For the beam scanning [93–95], in this review paper we focus on MEMS scanners. To illustrate the working principles of a MEMS scanner, here we briefly describe the mirror configurations and scanning methods. The scanning methods include raster scan and bi-resonant (Lissajous) scan. For the raster scan, the horizontal axis is driven in resonance with a high sinusoidal frequency (around 1 kHz), and the vertical axis is driven in a linear motion with a low frequency (60–120 Hz). The horizontal scanning can be performed unidirectionally or bidirectionally. Unidirectional scanning has more equidistant horizontal lines, but bidirectional scanning (Fig. 8(a)) can provide a higher resolution. For the bi-resonant scanning (Fig. 8(b)), both axes are driven with high sinusoidal frequencies, generating a so-called Lissajous trajectory. Due to a higher scanning frequency in the vertical direction, Lissajous scanning outperforms raster scanning in the vertical FoV, but the pixel density is less uniform [96]. Mirror configurations can also be divided into two kinds: two one-dimensional (1D) MEMS mirrors (Fig. 8(c)) and one 2D MEMS mirror (Fig. 8(d)). The 2D MEMS mirror reduces alignment steps and power consumption, but the cross talk between two axes will be unacceptable for high-resolution microdisplays, leading to the adoption of a bulkier two-mirror architecture.

5. DISPLAY METRICS

According to the inherent requirements of HVS mentioned previously, the five metrics resolution density, response time, efficiency/brightness/lifetime, HDR, and compactness are proposed to evaluate the performance of light engines for AR/VR applications. In the following, we compare different light engines based on these metrics one by one.

5.1. Resolution Density

In an AR/VR device, unless specified, the FoV usually refers to the diagonal direction. Without considering PPD degradation due to MTF mismatch, for a VR headset with 100° FoV, to meet a normal human visual acuity (60 PPD), a 6K resolution panel is required for each eye. On the other hand, a 2K resolution panel is required to support an AR device with 40° FoV. Moreover, a smaller microdisplay panel size leads to a smaller optics so that the formfactor of the headset will be more compact and lightweight. Therefore, for VR and AR devices, the display resolution of 6K×6K or 2K×2K should be packed into a 2-inch or 0.3-inch panel, which correspond to 2121 PPI and 4715 PPI, respectively. Such a demand challenges every display technology, including LCD, OLED, and micro-LED. It not only increases the manufacturing difficulty, but also has side effects on display performance, such as lower efficiency, more pronounced angular color shift, and reduced image quality. Recently, several advanced designs have been proposed to boost the resolution density of all display technologies. Next, we discuss them one by one.

5.1a. LCD

Presently, transmissive LCDs are widely used as light engines for VR headsets due to

Figure 8

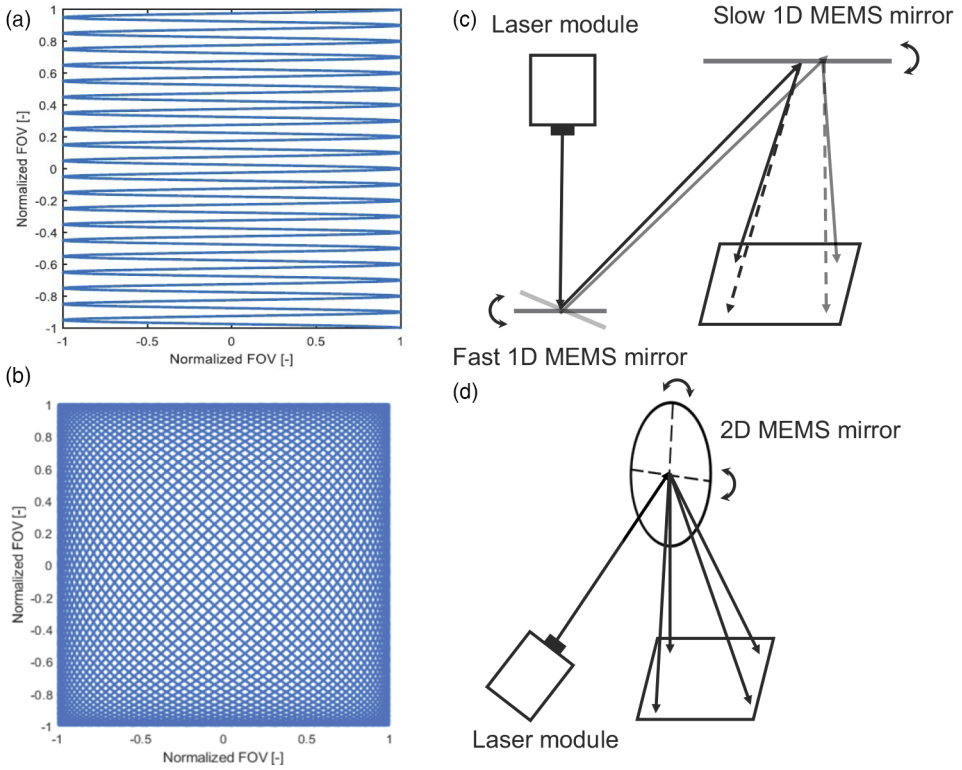

(a) Raster scan (bidirectional scan); (b) bi-resonant scan; (c) two 1D MEMS mirrors; (d) one 2D MEMS mirror. (a) and (b) Reprinted with permission from Reitterer *et al*., Proc. SPIE **11765**, 1176504 (2021) [96]. © 2021 SPIE.

their higher PPI, higher brightness, and lower cost than the competing active-matrix OLED displays, because the latter require more TFTs and compensation circuits to provide steady current. However, the LCD's resolution density is still insufficient to eliminate the screen door effect. For present commercial VR products, the LCD's resolution density is in the range of 500–800 PPI. As a result, there is still clearly a long way to go for the targeted 2000 PPI or higher. For a high PPI display, the subpixel width is restricted by the TFT manufacturing process. Recently, Innolux has developed process capability of narrow linewidth (1.5 μm) and line space (1.5 μm), as shown in Fig. 9(a) [97]. The corresponding subpixel size is minimized to 6 μm (1411PPI). A resolution density over 2000 PPI could be achieved by the subpixel rendering. However, the challenge of high-resolution density is not merely improving the manufacturing process to achieve narrower linewidths. As LCD resolution density increases, many challenges and issues arise. (1) Flicker effect, which refers to changes in the brightness of displayed image over time [98]. In a LCD, the storage capacitor is formed by the sandwich structure between pixel electrode, passivation layer, and common electrode. Furthermore, its capacitance is proportional to the cross-sectional area of the pixel and common electrode. As a result, the smaller the pixel size, the smaller the LC capacitance. The insufficient storage capacitance is unable to maintain the target driving voltage in entire frame time so that the pixel's brightness is susceptible to the voltage variation from data and scan lines. As a result, the image flicker is more pronounced [99]. To increase the storage capacitance, Innolux proposed to use top V_{com} structure and thinner passivation layer thickness [97]. Moreover, Huo *et al*. [100] used an additional passivation layer and common electrode to form a compensate capacitor at the opposite side of the pixel electrode to increase the LC pixel's storage

Figure 9

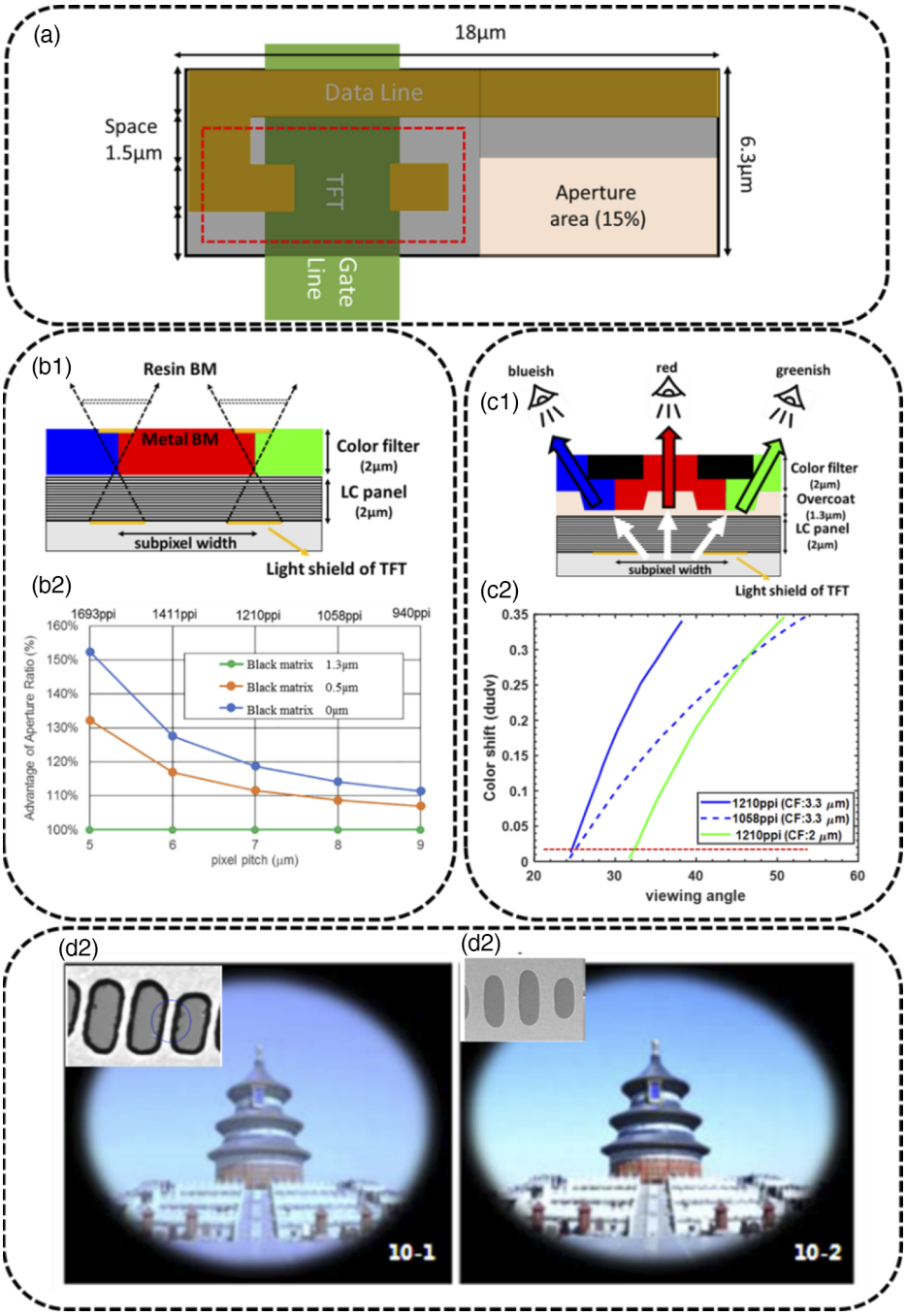

(a) Schematics of a LCD subpixel. (b1) Schematics of aperture ratio comparison between thin and thick black matrices. (b2) Aperture ratios of displays with different black matrix thicknesses and resolution densities. (c1) Schematics of color mixing effect in LCDs. (c2) Angular color shifts of LCDs with different color filter thicknesses and resolution densities. The image quality comparison is between (d1) a rounded resin black matrix and (d2) a sharp metal black matrix. (b1) and (b2) Reprinted from Yoshida *et al.*, J. Soc. Inf. Disp. **30**, 413–422 (2022) [101]. Copyright Wiley-VCH Verlag GmbH & Co. KGaA. Reproduced with permission. (d1) and (d2) Reprinted from Yao *et al.*, SID Symp. Dig. Tech. Pap. **52**, 735–737 (2021) [102]. Copyright Wiley-VCH Verlag GmbH & Co. KGaA. Reproduced with permission.

capacitance, which helps reduce the flicker ratio by 50%. In other words, the brightness variation during the frame time is reduced by 50%. (2) Small aperture ratio, which refers to the ratio of transmission area to the total subpixel area. The structure of each LCD subpixel is shown in Fig. 9(a), which consists of a TFT, driving line, and aperture area. Normally, a black matrix is overlaid on top of the electric circuit to prevent the current leakage of TFT originated from backlight illumination and on top of the driving line to prevent the light leakage from LCD by blocking the uncontrolled area. As a result, the aperture ratio of the LCD with 1411 PPI is only 15%.

Figure 9(b1) illustrates that if the color filter includes a thin black matrix (by using a low-reflectivity metal multilayer film), then the gap between TFT substrate and black matrix layer can be reduced. As a result, a smaller black matrix area and a larger aperture ratio can be achieved. Figure 9(b2) demonstrates the aperture ratio improvement of thin black matrix as a function of different display resolution density [102]. (3) Color mixing effect, which refers to the light in one pixel passing through the adjacent color filters [103,104]. For example, as shown in Fig. 9(c1), the emitted light from the red subpixel crosses to the adjacent blue and green subpixels. Therefore, the color purity is degraded at large viewing angles. This color mixing effect is more pronounced when the thickness of the LC cell increases and the resolution density increases. From the perspective of display resolution density, Fig. 9(c2) illustrates that the 1210-PPI LCD (solid blue line) shows a more noticeable angular color shift than the 1058-PPI LCD (dashed blue lines). From the perspective of cell thickness, a thinner black matrix helps to reduce the overcoat thickness in the CFs, thereby reducing the CF thickness from 3.3 μm to 2 μm. A thinner CF mitigates the color mixing effect so that the upper threshold angle of indistinguishable color shift ($\Delta u'\Delta v' < 0.02$) extends from 24° to 33° as illustrated in Fig. 9(c2). (4) Rounded and non-uniform black matrices significantly degrade the image quality of high-resolution-density LCDs. The thin metal black matrix (100–200 nm) with a much sharper edge than the traditional resin BM significantly improves the clarity of the displayed images, as shown in Fig. 9(d) [102].

5.1b. OLED

Although the high-resolution-density WOLED microdisplays have been commercialized by Sony and Kopin, to reduce the approximately 80% light loss caused by color filters, novel methods have been proposed to pattern RGB organic light-emitting material with high resolution density. In the traditional evaporation method, the organic material is sputtered through a FMM to obtain the desired pattern. However, the resolution density of the FMM fabricated by the wet etching process is inadequate, and the thick FMM (20 μm) will also form a wide shadow area during the evaporation process. Overall, this approach limits the display resolution density to about 600 PPI. To improve the resolution density of the FMM, as shown in Fig. 10(a1), Kim *et al.* [105] used a multi-scan femtosecond pulsed laser to ablate the pattern shapes in a metal mask. Such an ultrashort pulsed laser significantly avoids the deformation caused by overheating. In addition, the metal foil is thinned down from 20 to 2 μm to reduce shadowing effects during evaporation. Based on the above improvements, an 1057-PPI FMM (Fig. 10(a2)) has been produced successfully [106]. To further increase the resolution density of the FMM, the beam size of the laser could be reduced. By replacing the infrared laser with an UV laser, the beam size of the laser can be reduced from 15 to 2 μm, and the resolution density of FMM increases to 2400 PPI. In addition to metal shadow masks, Jiang *et al.* [107] also fabricated a high-resolution density (2000 PPI) shadow mask from a silicon nitride film as shown in Fig. 10(b1) and 10(b2). Silicon nitride films are suitable for photolithographic methods to achieve high resolution density patterns and are thin enough (<2 μm) to significantly reduce the shadowing effects. However, to pattern OLED devices with high resolution density,

Figure 10

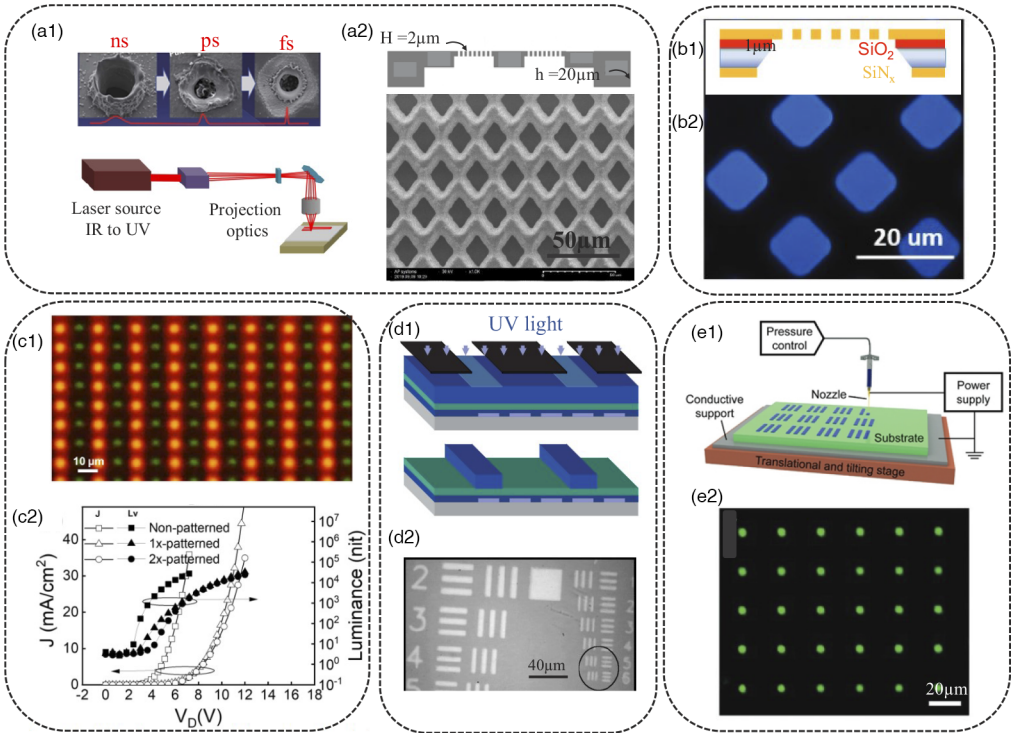

(a1) Schematics of FMM fabricated by a multi-scanned ultrafast laser. (Inset: SEM image showing drilling hole fabricated by different laser pulses.) Reprinted from Kim *et al.*, SID Symp. Dig. Tech. Pap. **49**, 1011–1013 (2018) [82] and Kim *et al.*, J. Soc. Inf. Disp. **28**, 668–679 (2020) [105]. Copyright Wiley-VCH Verlag GmbH & Co. KGaA. Reproduced with permission. (a2) SEM image of fabricated 1057-PPI FMM. Reprinted from Kim *et al.*, SID Symp. Dig. Tech. Pap. **52**, 131–134 (2021) [106]. Copyright Wiley-VCH Verlag GmbH & Co. KGaA. Reproduced with permission. (b1) Schematics of shadow mask fabricated by silicon nitride films. Reprinted from Jiang *et al.*, SID Symp. Dig. Tech. Pap. **49**, 1011–1013 (2020) [107]. Copyright Wiley-VCH Verlag GmbH & Co. KGaA. Reproduced with permission. (b2) PL image of patterned organic material evaporated through the silicon nitride films. Reprinted from Jiang *et al.*, SID Symp. Dig. Tech. Pap. **49**, 1011–1013 (2020) [107]. Copyright Wiley-VCH Verlag GmbH & Co. KGaA. Reproduced with permission. (c1) EL image and (c2) OLED device-degraded patterned organic material fabricated by the photolithographic method. (c1) Reprinted from Malinowski *et al.*, J. Soc. Inf. Disp. **26**, 128–136 (2018) [109]. Copyright Wiley-VCH Verlag GmbH & Co. KGaA. Reproduced with permission. (c2) Reprinted from Ke *et al.*, SID Symp. Dig. Tech. Pap. **52**, 127–130 (2021) [110]. Copyright Wiley-VCH Verlag GmbH & Co. KGaA. Reproduced with permission. (d1) Schematics and (d2) SEM image of solution-processed organic material patterned by direct photolithography. Reprinted by permission from Gather *et al.*, Adv. Funct. Mater. **17**, 191–200 (2007) [111]. Copyright Wiley-VCH Verlag GmbH & Co. KGaA. Reproduced with permission. (e1) Schematics and (e2) SEM image of electrohydrodynamic printing OLEDs. Reprinted from Ref. [112] with permission from the Royal Society of Chemistry.

it is not enough to simply increase the resolution density of the shadow mask. The evaporation sources should also be extended from point, line, to area so that the angle of incidence from the source to the mask can be reduced, which helps to suppress the shadowing effects [108]. In addition to the patterning process though a shadow

mask, IMEC and Fujifilm [109] have also developed a photographic method to pattern organic light-emitting materials with 1-μm linewidth, as shown in Fig. 10(c1). During the photographic patterning process, the organic material film is first evaporated in a vacuum chamber. Then, a substrate is removed from the vacuum chamber, and a photoresist material forms a design pattern on the organic material film. By reactive ion etching, the designed photoresist pattern is transferred to the organic material thin film. After that, the patterned organic thin film is loaded back to the vacuum chamber to evaporate the second color organic material, and then the same patterning process repeats. Organic light-emitting materials for RGB colors are patterned one by one to achieve full-color display. However, the exposure of organic materials in a non-vacuum environment, etching process, residual photoresist, etc., all lead to defects in the organic materials, resulting in degraded optical properties of OLED devices, such as reduced lifetime and increased driving voltage (~2 V increasement at a brightness of 1000 nits) [110]. The degradation of patterned OLED devices can be observed by comparing the *L*–*I*–*V* curves between the non-patterned and patterned OLED devices as shown in Fig. 10(c2).

Different from the photographic process that transfers the pattern on the photoresist to the organic material thin film through the etching process, Gather *et al*. [111] used oxetane-functionalized crosslinkable electroluminescent polymer as the functional photoresist. Crosslinking in films is induced by UV exposure. Therefore, as shown in Fig. 10(d1), by performing patterned UV exposure on the desired regions and rinsing the film with organic solvents to dissolve the unexposed areas, patterned organic light-emitting pattern with a 2-μm linewidth can be achieved (Fig. 10(d2)). Printing methods with fewer materials waste are also developed for patterning organic light-emitting materials. More recently, electrohydrodynamic jet printing [112,113], which controls the electric field between the nozzle and the substrate (Fig. 10(e1)), enables printing inks with a narrow linewidth down to around 5 μm, as demonstrated in Fig. 10(e2). However, ink sticking to the nozzle, print uniformity (no coffee-ring effect), and time-consuming printing process are the main challenges for its widespread application. Overall, the high-resolution-density patterning method by increasing the shadow mask resolution density and improving the evaporation source is most compatible with existing fabrication processes. Moreover, other advanced patterning techniques may break the vacuum environment and expose susceptible organic materials to moisture and air during the fabrication processes. Therefore, the lifetime issue of OLED devices fabricated by these novel patterning techniques, which disrupt the vacuum environment during the fabrication should be further evaluated.

5.1c. μLED

As mentioned previously, the μLED chips need to be transferred from a wafer to a display substrate. As a result, the resolution density of an RGB μLED display is determined by two factors: the chip size and the gap between them. The chip size is determined by the mesa manufacturing process of the LED chip and can be as small as 2 μm and the gap is determined by the transferring technologies. Compared with the "pick-and-place" approaches, monolithic integration methods achieving a gap of about 1 μm shows advantages for high-resolution-density microdisplay applications. Two monolithic integration methods have been implemented: flip-chip bonding and wafer-bonding style. The major difference between these two methods is whether the μLED chips are defined before or after the bonding process. For flip-chip bonding, the μLED chips are well defined on the LED substrate, and the metal-bonding arrays are fabricated on the CMOS substrate. Then, the μLED array is aligned and bonded to the CMOS backplane by a thermal-compression method. For wafer-bonding style, the LED epitaxy is firstly bonded to the entire CMOS substrate. Then, the μLED are

Figure 11

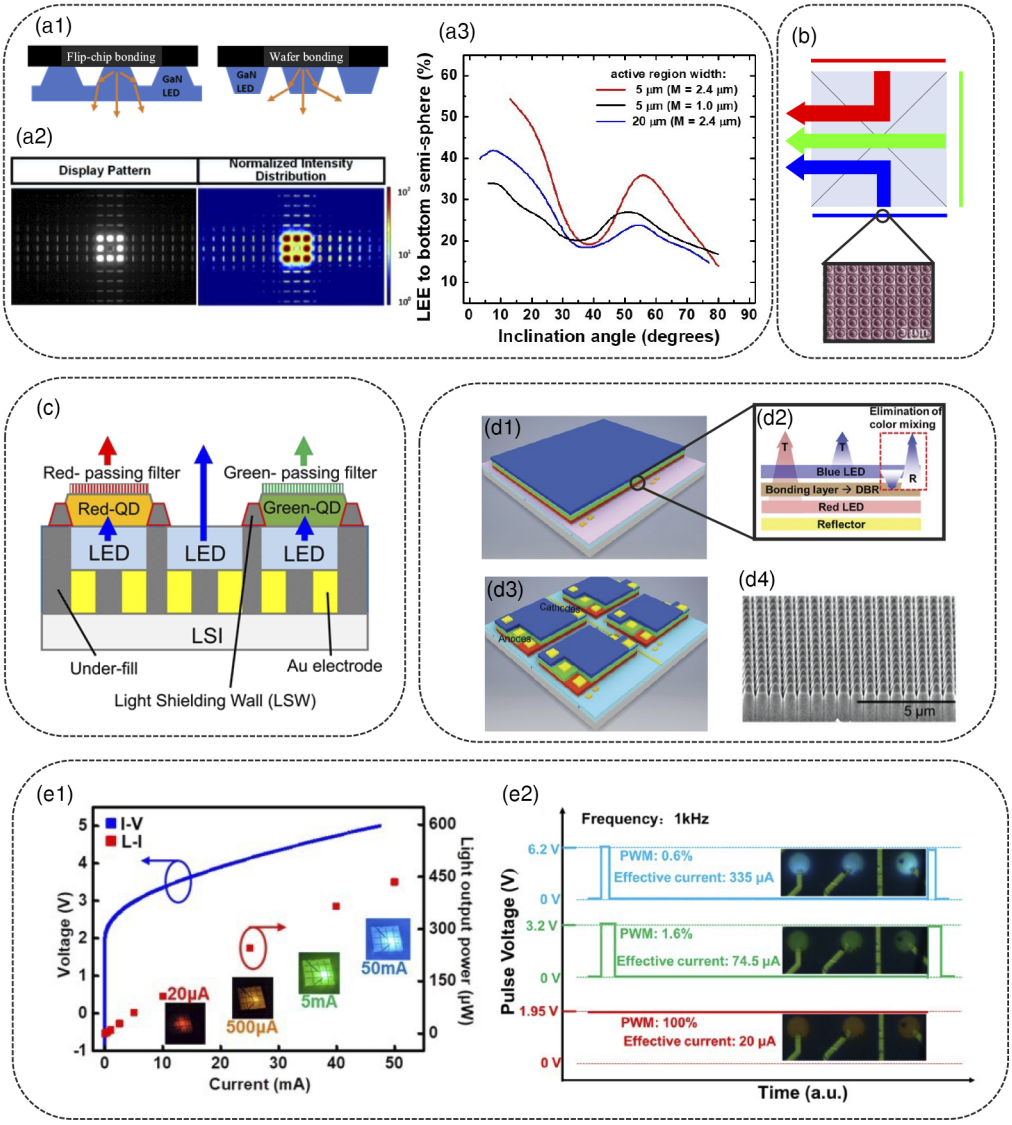

(a1) Schematics of μLED array fabricated by flip-chip bonding and wafer bonding. (a2) Cross talk effect in the flip-chip bonding μLED array. Reprinted with permission from [114] © The Optical Society. (a3) LEE of flip-chip μLED with different inclination angle. (Red, black, and blue lines indicate the LED chip with diameter 5 μm, 5 μm, and 20 μm and thickness 2.4 μm, 1 μm, and 2.4 μm, respectively). Reprinted from [115] under a Creative Commons license. (b) RGB μLED microdisplays combined by a trichroic prism. Reprinted by permission from Zhang *et al.*, J. Soc. Inf. Disp. **26**, 137–145 (2018) [116]. © 2018 Wiley (c) Color conversion micro-LED microdisplays. Reprinted from Kawanishi *et al.*, J. Soc. Inf. Disp. **29**, 57–67 (2021) [117]. Copyright Wiley-VCH Verlag GmbH & Co. KGaA. Reproduced with permission. (d1) Schematics of vertically stacked μLED film. (d2) DBR interlayer in stacked μLED film for avoiding light loss. (d3) The pixelized vertically stacked μLED connected to the driving circuit. (d4) SEM image of pixelated μLED array. (d1)–(d4) Reprinted from Ref. [123] with permission from the Royal Society of Chemistry. (e1) *L–I–V* curve of the multi-wavelength MQWs μLED and its emitted colors under different driving currents. (e2) PWM method for modulating the brightness of a multi-color LED. (e1) and (e2) Reprinted with permission from [124] © The Optical Society.

formed by the photolithography process followed by plasma etching. Both methods have pros and cons, and the manufacturing process and yield challenges have been summarized in [91]. From the perspective of optical performance, Fig. 11(a1) shows that the inverted trapezoidal geometry μLED chips fabricated by flip-chip bonding process are more convenient to extract the emission light to the normal direction than the trapezoidal geometry fabricated by wafer-bonding process. However, Fig. 11(a2) demonstrates a severe optical cross talk of the flip-chip μLED with connected n-GaN between each LED chip [114]. A complete isolation trench between each pixel is required to eliminate the optical cross talk. Moreover, the inclination angle of the inverted trapezoidal geometry should be tailored for improving the LEE of the LED chips at normal direction, as shown in Fig. 11(a3) [115].

The μLED microdisplays fabricated by the monolithic integration methods are normally single color, so various methods have been developed to obtain full colors. The most convenient way is to combine the displayed images of three separate RGB μLED microdisplays through a trichroic prism [92], which is then projected by a lens. Because the RGB subpixels are provided individually by three separate panels, rather than side by side in a single panel as shown in Fig. 11(b) [116], the LED pitch is the same as the pixel pitch, and the resolution density can be as high as 10,000 PPI. However, the aligning and driving three display panels synchronously are still challenging. In addition, from the optics perspective, the trichroic prism is bulky and the distance between the projection lens and the emission panel is relatively long, which also reduces the FoV of the AR device. Another solution is to assemble color conversion materials on top of the blue or UV μLEDs as shown in Fig. 11(c) [117]. Numerous QD pattering processes have been proposed to pattern a uniform QD array with high resolution density, sufficient film thickness, and reasonable stability [118,119]. Inkjet printing and photolithography are the two main methods for patterning QD arrays due to their ability to form reasonable film thicknesses (few micrometers). However, the uniformity and nozzle clogging are common issues of inkjet printing technologies. For the photolithography, QD material degradation, due to exposure to solvents and water, reduces the efficiency and stability of the QD arrays. Other methods, such as microcontact printing, electron-beam lithography, and light-driven ligand crosslinker, could provide a narrower linewidth which is favorable for high-resolution density display applications, but the insufficient film thickness [120–122] results in a severe blue light leakage and low color conversion efficiency. Therefore, the challenges of patterning high-resolution-density QD arrays are twofold: to achieve not only narrow linewidths but also high aspect ratios (thickness-to-width ratios).

Figures 11(d1)–11(d4) shows the device structure of a vertically stacked μLED display on a driver circuit through monolithic 3D integration [123]. The driver circuits, metal lines, and electrode pads of each RGB pixel are prefabricated before the monolithic integration process. Then, to avoid the alignment process, thin film transfer was performed to bond the uniformly stacked μLED thin film layer on the driving substrate, as shown in Fig. 11(d1). It is worth noting that for the stacked μLED thin film layer, due to the high absorption of InGaP-based red LED, it is usually placed at the bottom of the stack. Furthermore, to reflect the back-emitted green and blue light, a high distributed Bragg reflector (DBR) film is deposited on the interface between the blue and red LEDs (Fig. 11(d2)). After that, Fig. 11(d3) illustrates that high-resolution-density vertically stacked μLED pixels can be defined by photolithographic methods, including the cathode and anode of each layer of LEDs. Finally, the cathode and anode of each LED are interconnected with the prefabricated driver circuit common and bus lines. The pixel size of LEDs can be as small as 0.5 μm as shown in Fig. 11(d4), regardless of driving capability. Overall speaking, vertically stacked RGB μLEDs [125–130] can

triple the resolution density, and the monolithic 3D integration could achieve precise alignment, resulting in high resolution density. However, the complicated fabrication process still hinders its widespread applications.

In addition to stacking RGB LEDs, multi-wavelength MQWs have also been explored. For example, one MQW with a higher concentration of indium emits red light and the other MQW with a lower concentration of indium emits blue light [131]. As shown in Fig. 11(e1), the emission wavelength of the μLED is determined by modulating the driving current, and the brightness is determined by modulating the emission time. Similar to stacked RGB LEDs, multi-wavelength MQW full-color μLED chips can emit RGB light on the same μLED chip, providing a three-fold increase in resolution density as compared to the side-by-side RGB μLED displays. However, there are two main drawbacks for this kind of devices. (1) Color purity. As both MQWs emit at different driving currents, the color purity of such μLEDs has yet to be improved. (2) Complicated driving circuit. As shown in Fig. 11(e2) [124], because the driving current for blue light is much higher than that for red light, the blue light-emitting time (0.6%) should be much shorter than the red light-emitting time (100%) to have the same brightness. If we further consider generating 10-bit gray levels, the driver is a big burden to overcome. Despite the above-mentioned challenges, these μLED displays still attract a lot of attention because they do not require complex transfer and stacking processes. For example, Porotech demonstrated a single-pixel full-color adjustable display prototype at SID 2022 and won the I-Zone Best Prototype Award.

5.1d. LCOS

The resolution density of a LCOS is mainly limited by the FFE and the limited voltage swing [132]. When the pixel pitch of a LCOS device is comparable with or even smaller than the cell gap, unequal voltages on adjacent pixels generate a pronounced horizontal electric field, which causes the FFE. For this reason, a straightforward method to mitigate FFE is to employ a thinner cell gap by using a higher birefringence LC mixture [133–135]. To demonstrate the FFE in an amplitude LCOS panel, we simulate the FFE of MTN and VA modes using TechWiz LCD 3D program. Figure 12(a) shows the simulated reflectance for the 6-μm-pitch VA cell and 6-μm-pitch 90°-MTN cell when the three adjacent pixels are operated at dark–bright–dark state. The overall dark state in the 90°-MTN cell is quite good, except for a small lobe at the right-hand side of the dark pixel. In contrast, the FFE in the VA cell is rather strong: the fringing fields induce a broad dark stripe near the right edge of the bright pixel. Due to the negative dielectric anisotropy, the LC directors tend to reorient perpendicular to the incident plane. At a certain position, most of the LC directors are orthogonal to the incident polarization direction, leading to the unchanged polarization state. Under such a condition, the incident light is completely blocked, and a dark stripe splits the bright pixel into two unequal parts. In summary, the FFE can reduce the optical efficiency and contrast ratio of an amplitude LCOS device.

Several strategies have been proposed to suppress the FFE of amplitude LCOS devices since the early 2000s. In 2002, Fan-Chiang *et al*. optimized the slope of pixel electrodes to reduce FFE [137]. For the 80°-MTN and 45°-TN modes, the optimal ITO electrode slope is 1; however, changing the slope can hardly mitigate the FFE of the VA mode. In 2005, Fan-Chiang *et al*. adopted a circularly polarized (CP) light to eliminate the FFE of the VA mode [136] (Fig. 12(b)). At $x = x_b$, most LC directors are aligned along the y direction. Therefore, little phase retardation is accumulated at $x = x_b$ when the incident light is linearly polarized along the x direction, leading to a dark region. A CP light will help solve this issue because the phase retardation is still accumulated no matter where the LC director is orientated. Later, Li *et al*. proposed a double mirror structure and butterfly-like pixel shape to compensate the deformation of LCs [138].

Figure 12

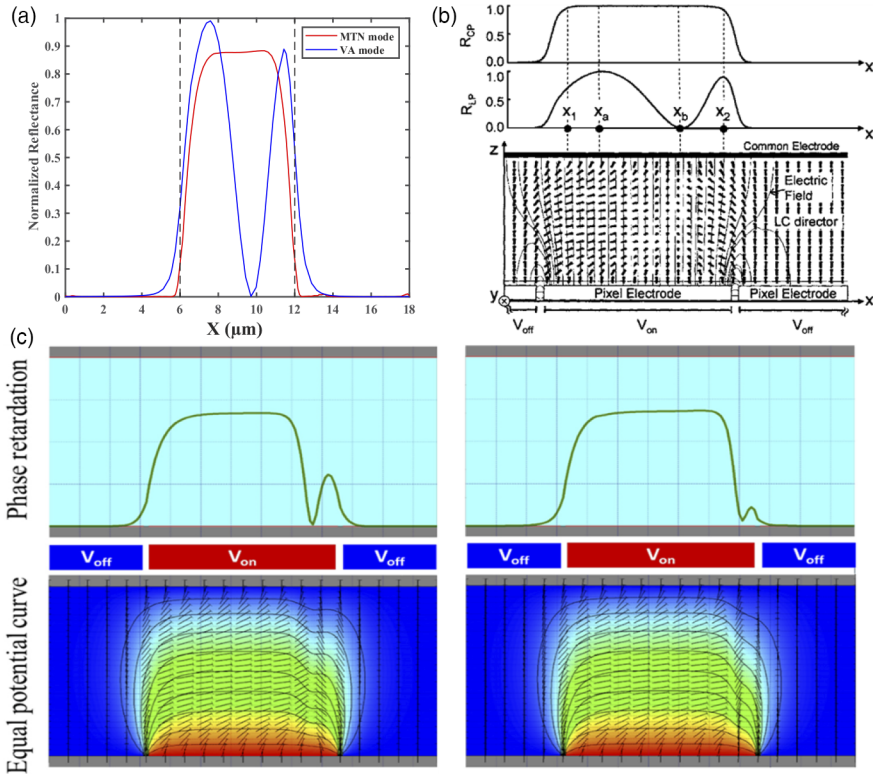

(a) Simulated FFE of the MTN and VA modes in an amplitude LCOS device and (b) CP light employed to eliminate the FFE of the VA modes. Reprinted with permission from Chiang *et al.*, Appl. Phys. Lett. **87**, 031110 (2005) [136]. Copyright 2005, AIP Publishing LLC. (c) FFE without patterned pretilt angle (left) and the reduced FFE with patterned pretilt angle (right). Reprinted from [132] under a Creative Commons license.

Vithana developed a VA mode with large pretilt angles to remove the disclinations and introduce twisted structure to keep a high contrast ratio [139], enabling a pixel pitch of ~3 μm. Liao proposed patterned pretilt angles to mitigate the FFE [140] (Fig. 12(c)). In this method, the pixel region is divided into two zones with a FFE border width, and such an inhomogeneous LC alignment helps mitigate FFE. The pretilt angle of the optimized inner zone and outer zone is 88° and 85°, which can significantly reduce the FFE as shown in the right-hand side of Fig. 12(c).

For a phase LCOS device, which is commonly called spatial light modulator (SLM), the required phase change is 2π. As a result, the FFE is more severe than that in an amplitude LCOS device because of the twice thicker cell gap. To demonstrate the FFE in a SLM, we use TechWiz LCD 3D to calculate the LC director distribution and then calculate the accumulated phase change by [141]

$$\Delta\varphi(x) = \frac{4\pi}{\lambda}\int_0^d \frac{n_e n_o}{\sqrt{n_o^2 + (n_e^2 - n_o^2)\sin^2(\theta(x,z))}}dz, \tag{1}$$

where n_o and n_e are ordinary and extraordinary refractive indices of the LC material, respectively, d is the cell gap, and θ is the tilt angle of the LC directors. The simulated configuration is as follows: three adjacent pixels operate at on–off–on states, constituting binary phase gratings. The on state refers to the maximum phase change and the off state represents the minimum phase change. Figure 13(a) shows that the FFE blurs the

Figure 13

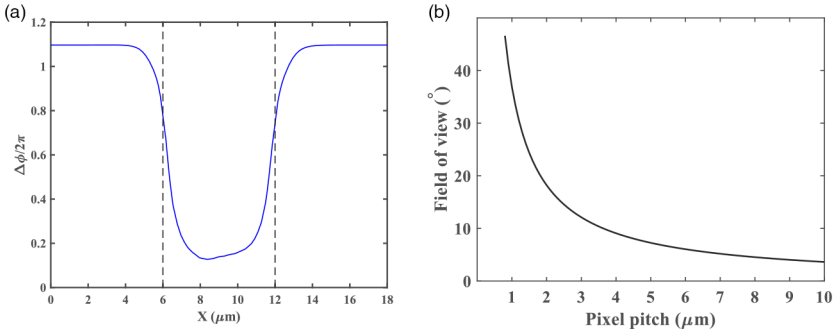

(a) Simulated FFE of the HG mode in a phase LCOS device. (b) Relation between FoV and pixel pitch in a holographic display.

phase edges due to a transition region connecting the on and off states. Owing to the smeared phase profiles, the diffraction efficiency in holographic displays is reduced. In particular, 1 μm or less pixel pitch is required to achieve a wide FoV holographic display [14,35] (Fig. 13(b)). To suppress the strong FFE for the 1-μm pixel pitch, the dielectric shield wall structure was proposed [142], but the LC alignment remains a major challenge [143]. Other strategies aim at integrating a modeled or measured SLM response [144–146] (point spread function) into holographic calculations.

In addition to FFE, the limited voltage swing of the LCOS poses another challenge to achieve 1-μm pixel pitch. In such a small pixel area, the CMOS backplane can only support a limited voltage swing. For a LCOS panel with more than 5000 PPI, the driving voltage is usually below 3.3 V [147]. Optimizing material parameters can be an effective solution to reduce the operating voltage while keeping a fast response time. Some main parameters of a LC mixture include birefringence (Δn), dielectric anisotropy ($\Delta\varepsilon$), elastic constants (K_{ii}), and rotational viscosity (γ_1). A higher Δn enables a steeper slope of the voltage-dependent phase curve. On the other hand, elastic constant and dielectric anisotropy jointly determines the Freedericksz threshold voltage; a larger dielectric anisotropy helps to reduce the threshold voltage and operating voltage. On the other hand, response time is determined by the cell gap and viscoelastic constant. Therefore, these parameters are interrelated.

To illustrate the optimization process, we use DIC A4907 [148] as an example. The voltage-dependent phase curves corresponding to different material parameters can be simulated via TechWiz LCD. When the dielectric anisotropy remains unchanged ($\Delta\varepsilon = 7.3$), a low operating voltage of 3.3 V can be obtained if Δn increases to 0.23. However, it is challenging to obtain such a high birefringence while retaining a low viscosity. Although tolane compounds help realize this goal, their ultraviolet (for hermetic sealing the SLM) and blue photostability remains a concern. The other method to reduce the operating voltage is to decrease the threshold voltage. For this method, the slope of the voltage-dependent phase curve basically remains unchanged, and the curves shift towards the lower voltage side because of its lower threshold voltage, if the dielectric anisotropy increases from 7.3 to 16.3. However, the challenge for this method is to obtain such a high dielectric anisotropy without increasing the viscosity too significantly. The difluoromethoxy bridge (–CF_2O) [149] and isothiocyanato group (–NCS) [150] could improve $\Delta\varepsilon$ while retaining a low viscosity. However, the molecular π–π conjugation is broken in the former, leading to a low Δn, whereas the latter decreases the voltage holding ratio because the –NCS dipole tends to trap ions. If we combine these two mechanisms to lower the operating voltage to 3.3 V_{rms},

Figure 14

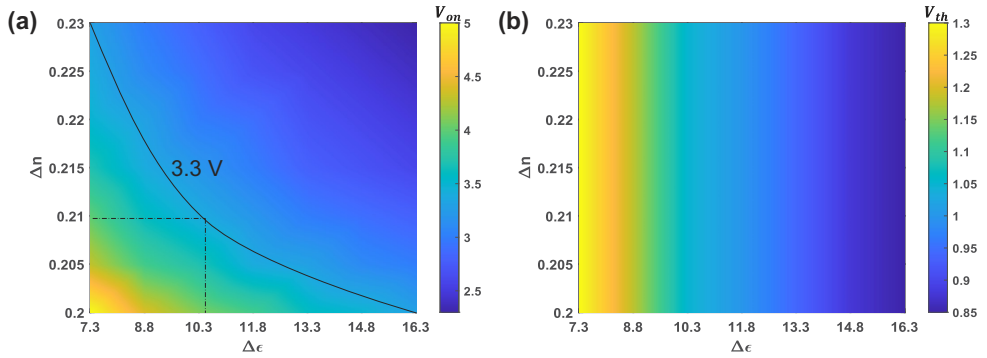

(a) Operating voltage and (b) threshold voltage as a function of Δn and $\Delta\varepsilon$.

numerous combinations of Δn and $\Delta\varepsilon$ can be searched in the parameter space. Figure 14(a) shows how the operating voltage varies with Δn and $\Delta\varepsilon$: as both Δn and $\Delta\varepsilon$ increase, the operating voltage is dramatically decreased from 5 V to 2.5 V. A certain operating voltage of 3.3 V can be realized by different combinations of Δn and $\Delta\varepsilon$, as indicated by the same color corresponding to different Δn and $\Delta\varepsilon$. Figure 14(b) shows how the threshold voltage varies with Δn and $\Delta\varepsilon$: the threshold voltage decreases as $\Delta\varepsilon$ increases. Among all the combinations of Δn and $\Delta\varepsilon$ that can generate 3.3 V operating voltage, a medium $\Delta\varepsilon$ is desirable due to a larger V_2/V_{th} ratio. For example, if $\Delta n = 0.21$ and $\Delta\varepsilon = 10.3$, then the operating voltage is 3.3 V and the threshold voltage is 1.05 V. Such a LC mixture is not too difficult to obtain.

5.1e. DLP

For DMD, the resolution density is mainly limited by the gap between micromirrors. Presently, the smallest pixel pitch is 5.4 μm as implemented in the Texas Instruments DLP3010. A certain gap distance should be maintained to allow each micromirror to rotate independently without colliding with each other. In comparison with DMD, the gap between pixels in a LCOS panel can be much smaller because the light modulation is through the liquid crystal layer, instead of mechanically moving mirrors. When the pixel size decreases, the gap between mirrors may be comparable with the mirror size, leading to a strong diffraction. The diffraction dramatically reduces the efficiency and the contrast ratio of the DMD, making an ultrahigh resolution density difficult.

5.1f. LBS

The resolution density of the LBS is determined by the number of resolvable spots. Under the paraxial approximation, the number of resolvable spots along the horizontal direction can be calculated by the following equation [151]:

$$N_h = \frac{\theta_{opt} z}{a\lambda z/D} = \frac{\theta_{opt}}{a\lambda/D} = \frac{\theta_{opt} D}{a\lambda}, \tag{2}$$

where z is the distance from the MEMS scanner to the screen, θ_{opt} is the full optical scan angle, D is the clear mirror aperture, a is a shape factor determined by the beam profile, mirror shape, and the amount of spot overlap between adjacent spots. For example, $a = 1.22$ if the shape of mirror is circular and laser beam profile approaches plane wave. The practical a value ranges from 0.75 to 2, depending on the laser beam profile, mirror shape, and so on. Some relevant parameters are sketched in Fig. 15(a). The horizontal pixel size is typically chosen to be equal to the spot size, $a\lambda z/D$. From Eq. (2), the product of θ_{opt} and D determines the maximum horizontal resolution. On

Figure 15

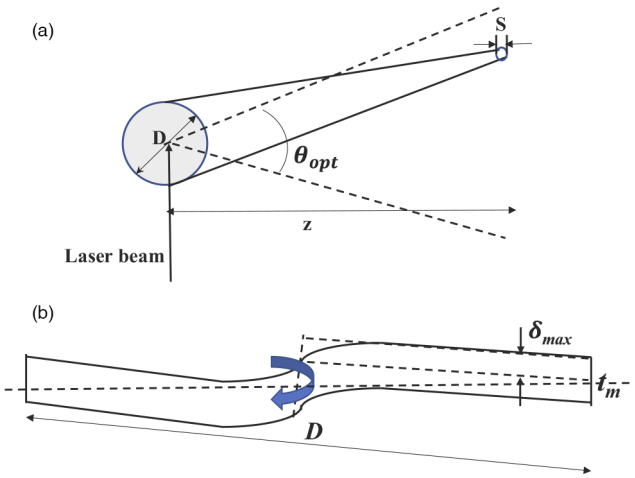

(a) Schematic of the laser beam scanning. (b) Schematic of the dynamic mirror deformation.

the other hand, the number of resolvable spots along the vertical direction is calculated as

$$N_v = \frac{f_h K_{ub} K_{rt}}{F_r}, \tag{3}$$

where f_h is the horizontal scanner frequency, F_r is the frame rate, K_{ub} is 1 for unidirectional scanning and 2 for bidirectional scanning, and K_{rt} considers the retrace time of the vertical scanner. From Eq. (3), the ratio of the horizontal scan frequency to the frame rate determines the maximum vertical resolution. Bidirectional scanning and a large K_{rt} relieve the requirement for the horizontal scanner frequency. Overall, a large mirror aperture and a wide scan angle are desired to increase the horizontal resolution; a high horizontal scanner frequency is demanded to obtain the high vertical resolution. There is also a trade-off between frame rate and vertical resolution. In real applications, a larger mirror aperture can worsen mirror deformation as shown in Fig. 15(b), leading to image distortions and decreased scanning frequency [152]. According to Brosens's formula [153], the mirror deformation relates with the mirror aperture as

$$\delta_{\max} = 0.217 \frac{\rho f^2 D^5 \theta_{mech}}{E t_m^2}, \tag{4}$$

where f is the scanner frequency, ρ is the material density, D is the mirror aperture, E is the modulus of elasticity, t_m is the mirror thickness, and θ_{mech} is the zero-to-peak mechanical scan angle. To ensure a good image quality, the mirror size is limited by the maximum tolerable mirror deformation, thereby limiting the horizontal resolution.

5.2. Fast Response Time

The display with fast response time has two main functions in an AR/VR display system: one is to alleviate motion blur from the displayed image and the other is to generate multi-depth images to mitigate the VAC effect. To alleviate motion blurs, a fast MPRT is desired. To achieve MPRT < 1.5 ms, both high frame rate and low duty ratio (the backlight-on time in a frame) can be considered. However, as the frame rate increases from 60 to 120 and then to 240 Hz, the MPRT value will decrease noticeably first but then gradually saturate. Therefore, a low duty ratio (10–20%) illumination plays a key role to suppress the motion blurs. On the other hand, to generate multi-depth images, because the content of images at different depths is diverse, a high

frame rate is required to quickly update the image information at different depths. Each display system has different constraints to achieve fast response time. For example, the response time of LCDs and LCOS microdisplays is mainly limited by the employed LC material. On the other hand, for OLED and μLED displays, because the device response time is in the microsecond and nanosecond range, the constraints come from the backplane (driving circuit). Furthermore, there is a trade-off between high frame rate and bit depth in DLP displays, and between high frame rate and display resolution in LBS displays. In next section, we dive into each display system one by one.

5.2a. LCD

High frame rate (240 Hz) LCDs have been commercialized for gaming monitors. However, most of these commercial products still have a LC response time of about 5 ms if the overdrive and undershoot voltage [154] is not applied. With overdrive and undershoot, the LC response time can be reduced to about 1 ms. Under such condition, if the duty ratio remains at 100%, then the MPRT is still ~4 ms, which is mainly determined by the 240-Hz frame rate. Such a MPRT is still far from the target 1.5 ms for motion-blur-free CRT-comparable images [155]. In addition, the overdrive function may further cause inaccurate gray levels and degraded image quality. Therefore, a low duty ratio (<30%) has been widely employed to reduce the MPRT of the display. Figure 16(a) illustrates the driving time chart of a LC panel with duty illumination, which consists of three parts: scanning time, LC response time (LCRT), and backlight emission time (backlight is on). In other words, the sum of scanning time, LC response time, and backlight emission time should be smaller than the frame time. As shown in Fig. 16(b), if we set the scan time for 2160 gates to 5 ms and take an emission duty ratio of 25% as an example, the LCRT of the 120 Hz panel is 1.5 ms and the corresponding MPRT matches the target value: 1.5 ms. Although using a smaller emission duty ratio (e.g., 10%) allows more time for the LC to response (1.5–2.5 ms), an instantaneously brighter backlight results in a higher driving current and higher power consumption. In addition, one can use a lower frame rate (e.g., 90 Hz as shown) and a smaller duty cycle (e.g., 15%) to achieve the same MPRT (1.5 ms). At such a frame rate and duty ratio, the remaining LCRT is about 4.5 ms, which is friendly to LC devices. However, as mentioned previously, low-frame-rate displays are not suitable for multi-depth applications. Thus, to simultaneously achieve high frame rate that generates multi-depth images and small duty ratio that mitigates motion blurs, a fast-response LC device is required. In the following discussions, we focus on novel LC modes and electrode designs to reduce LCRT without the overdrive/undershoot function to maintain decent image quality and simple driving circuit. According to Eq. (5), LCRT can be reduced by using a thinner cell gap and a LC material with a smaller viscoelastic coefficient (γ_1/K_{ii}):

$$\tau_0 = \frac{\gamma_1 d^2}{\pi^2 K_{ii}}. \tag{5}$$

In Eq. (5), the corresponding elastic constant K_{ii} depends on the employed LC mode. Taking FFS mode as an example, the corresponding K_{ii} is the twist elastic constant (K_{22}), whose value is about two or three times smaller than the splay and the bend elastic constants (K_{11} and K_{33}), which corresponds to TN and VA LCDs. However, the negative dielectric anisotropy LC material used in VA mode usually exhibits a higher rotational viscosity because the polar groups are in lateral positions.

To further improve LC response time, various approaches for forming virtual walls have been proposed and widely applied [156–160]. Yoon *et al*. [161] demonstrated a three-electrode vertically aligned LC panel with a longitudinal electric field at the top of the gap region and fringe field at the gap peripheral region (VA-FFS mode). The LC

Figure 16

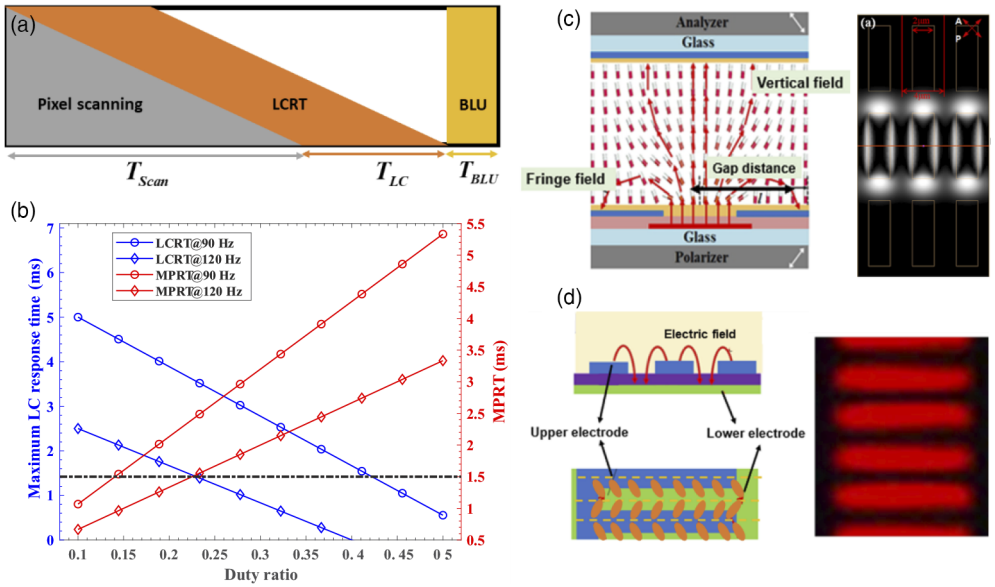

(a) Timeline of LCD driving. (b) Calculated maximum allowable LCRT and the corresponding MPRT as a function of duty ratio. The black dashed lines represent a cathode ray tube (CRT)-like MPRT = 1.5 ms. (c) Schematics and transmittance distribution VAFFS mode LCD. Reprinted with permission from [161] © The Optical Society. (d) FFS mode LCD with 0° rubbing angle and non-zero pretilt angle. Reprinted from Matsushima *et al.*, J. Soc. Inf. Disp. **29**, 221–229 (2021) [160]. Copyright Wiley-VCH Verlag GmbH & Co. KGaA. Reproduced with permission.

directors in the gap region do not reorient, forming virtual walls to provide a strong restoring force. The device structure and its transmittance distribution are depicted in Fig. 16(c). Furthermore, Fig. 16(d) illustrates that the FFS LCD can easily form virtual walls by using zero degree rubbing angle and non-zero pretilt angle [160]. The LC directors on top of electrodes are fixed, and on both sides of the electrode rotate clockwise and counterclockwise, respectively. When the virtual wall is formed, three anchoring forces are present simultaneously: top and bottom alignment layers, and the virtual walls. Therefore, the LC response time is no longer governed solely by the cell gap, but also by the distance between virtual walls. Taking the short-range lurch control in-plane switching proposed by Japan Display Inc. as an example, its LC decay time is determined by [160]

$$\tau_0 = \frac{\gamma_1}{\pi^2 \left[\frac{K_{22}}{d^2} + \frac{K_{11}}{l^2}\right]}. \tag{6}$$

Under normal conditions, $K_{11} \approx 2K_{22}$ [162]. If the distance between two dead zones is the same as the cell gap, the LC response time would be reduced by a factor of three. Despite the benefits of fast response time mentioned previously, in the virtual wall region, the incident light on the non-rotating LC molecules has no accumulated phase and is, thus, further blocked by the top analyzer. Overall, these advanced LC devices have improved response time at the expense of efficiency.

5.2b. LCOS

For LCOS devices, color sequential operation is widely adopted for achieving high resolution. Therefore, high frame rate is essentially desirable to avoid color break-up. The frame rate of LCOS devices is mainly limited by the LC response time. Due to

the reflective operation in the LCOS, its response time is approximately four times faster than the corresponding transmissive LCD. To reduce response time further, high birefringence and low viscosity LC mixtures [163] are particularly desirable. Chen *et al*. [164] developed a fluorinated high-birefringence and low-viscosity negative dielectric anisotropy LC mixture to enable a VA LCOS with submillisecond response time. Later, Peng *et al*. [165] reported a LC mixture with low viscosity and high clearing point for a color sequential MTN LCOS. The average gray-to-gray rise time is 0.5 ms and gray-to-gray decay time is 0.2 ms at $T = 55°C$. Abeeluck *et al*. [166] reported an amplitude LCOS device with a color subframe rate greater than 720 Hz to avoid color break-up. On the other hand, the required phase range for a phase LCOS SLM is 2π, which is about twice as large as its amplitude counterpart. Therefore, the cell gap of an LCOS SLM is twice as thick if the same LC material is employed. As a result, the response time for a phase LCOS device is approximately four times slower than its amplitude counterpart [167]. For this reason, it is challenging to obtain the LCOS SLM with a high frame rate. Polymer network liquid crystals can be a potential solution to achieve submillisecond response [168], but the high driving voltage limits its adoption in the LCOS SLM. Recently, by using a high birefringence ($\Delta n \approx 0.21$) yet photo-stable LC mixture, a LCOS SLM with 2π phase change at $\lambda = 633$ nm and ~3 ms response time (rise + decay) [169], which enables the LCOS SLM to be operated at 300 Hz, has been demonstrated. To further decrease the response time, ferroelectric liquid crystal (FLC) was used in LCOS devices because of its microsecond response time [170,171]. To realize the inherent advantages of FLCs, photoalignment by nano-size azo-dye was employed [172]. Three electrooptic modes, namely surface stabilized FLC, deformed helix ferroelectric (DHF), and electrically suppressed helix, have been developed. For FLC-based LCOS microdisplays, the DHF mode stands out because of its low driving voltage, high resolution, and ultrafast response time. However, such a FLC has no threshold voltage to block the TFT voltage fluctuation, and the driving circuits are rather complicated. On the other hand, for holographic displays, the first-order diffraction efficiency is only about 40.5% due to its binary phase modulation [173].

5.2c. DLP

Among all the light engines, DMD has the highest frame rate, which is enabled by a fast electromechanical response (~μs) of micromirrors. Because the micromirror operates at a binary (on/off) state, only black and white images can be generated without any processing. To deliver an n-bit gray-scale image, PWM at each pixel is usually used. The key point is that each frame is divided into n sequentially projected bit-planes. The gray level of each frame depends on the ratio of the whole on-state time to one frame time because the luminance is averaged by human eyes due to the persistence of vision. The exposure time of each bit-plane is sequentially $t, 2t, \ldots, 2^{(n-1)}t$ μs, which is weighted by the corresponding power of 2. Figure 17(a) shows that how an 8-bit gray-scale image is generated with PWM. It is noted that the minimum bit-plane exposure time is limited by the DMD's refresh time. With block-based control, the minimum bit-plane exposure time can be as little as 2 μs [174]. To project a color image, the above sequential bit-planes are repeated for each color channel, thus tripling the frame time to $3 \times (2n - 1)t$. When the bit depth increases, the total frame time exponentially increases, leading to the exponentially decreasing frame rate. This trade-off between frame rate and bit depth is demonstrated in Fig. 17(b). One solution to break the exponential relationship is to use intensity-modulated light with the intensity of $2(n - i)$ multiplied by the maximum intensity of light source L at the ith bit-plane. For this method, each bit-plane has the same exposure time t with different illumination intensity (Fig. 17(c)), leading to a linear relationship between the total frame time of $n \times t$ μs and the bit depth. However, the maximum averaged brightness is significantly

Figure 17

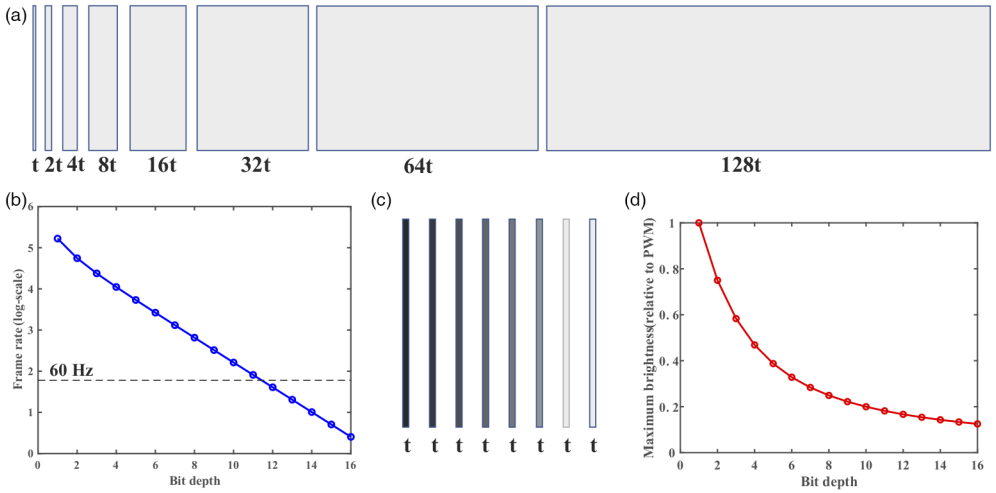

(a) Schematic of an 8-bit gray-scale image with the PWM method. (b) Trade-off between frame rate and bit depth with the PWM method (t = 2 μs) (c) Schematic of an 8-bit gray-scale image with the intensity-modulated light (d) Trade-off between maximum brightness and bit depth with the intensity-modulated light.

Figure 18

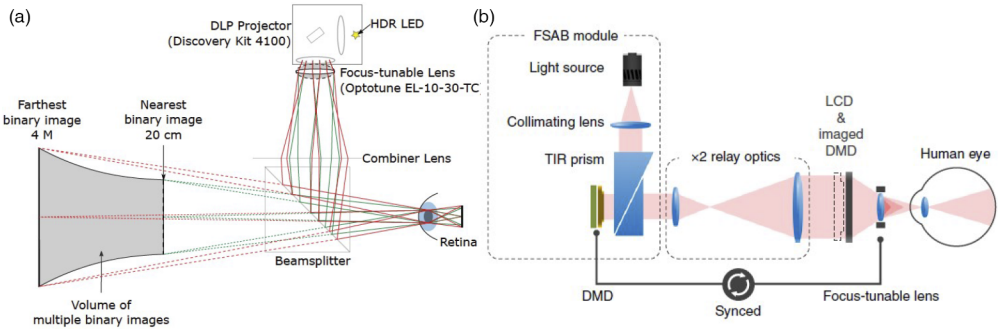

(a) Schematic of a volumetric near-eye display composed of a HDR LED, a DLP projector, a focus-tunable lens, and a combiner lens. © 2018 IEEE Computer Society. Reprinted, with permission, from Rathinavel *et al.*, IEEE Trans. Visual. Comput. Graphics **24**, 2857–2866 (2018) [175]. (b) Schematic of tomographic near-eye displays consisting of a FSAB module, a relay optics, a LCD module, and a focus-tunable lens. Reprinted from [176] under a Creative Commons license.

reduced, which can be calculated as

$$L_{\max} = \frac{L(2^{-(n-1)} + \cdots + 2^{-1} + 1)t}{nt} = \frac{2}{n}(1 - \frac{1}{2^n})L. \tag{7}$$

For example, when the bit depth $n = 16$, the maximum brightness is reduced to about $L/8$, as shown in Fig. 17(d). For AR applications calling for high brightness, this solution is impractical.

The high-speed response makes the DMD a perfect candidate for a multifocal AR enabled by time multiplexing. Rathinavel *et al.* [175] achieved a full-color volumetric near-eye display with a focus ranging from 20 cm to 4 m via the synchronized operation of the HDR LEDs, the DMD and the focus-tunable lens, as shown in Fig. 18(a). The number of single-color binary images decomposed from a color image is determined

by the ratio of the DMD's refresh rate to the target display refresh rate. Their DMD's refresh rate and target display refresh rate is 16,800 Hz and 60 Hz, respectively, which can support 280 binary images distributed at different depths. Later, Lee *et al*. [176] presented a tomographic near-eye display enabled by the synchronization of focus-tunable lens and a fast spatially adjustable backlight (FSAB). Figure 18(b) shows a benchtop prototype consisting of a FSAB module, relay optics, LCD module, and a focus-tunable lens. At the heart of the FSAB module is a DMD, which can show binary images at a very high frame rate. The relay optics provides a magnified image of the DMD panel at the LCD plane. The LCD module determines the gray levels and the resolution. The complementary relations between the FSAB module and the LCD module breaks the trade-off between frame rate and bit depth and, thus, support 24-bit depth color as well as a high frame rate for 80 focal planes.

5.2d. LBS

The frame rate of LBS is usually 60 Hz, which might cause image flickering. In raster scan, the frame rate is the same as the vertical scanning frequency. According to Eq. (3), there is a trade-off between frame rate and vertical resolution. Bidirectional writing schemes and a short retrace time of the vertical scanner [177] help increase the frame rate at a given vertical resolution. On the other hand, increasing horizontal scanner frequency can also boost the frame rate at a given vertical resolution. Reducing the mirror size is a straightforward way to obtain a higher horizontal scanner frequency, but the diffraction effect may limit the horizontal resolution.

5.2e. μLED and OLED

The device response time of OLED and μLED is in the microsecond and nanosecond level, respectively, which enables a single device to be driven at megahertz or gigahertz for optical communication applications. However, the situation is completely different for display applications where millions of pixels should be driven to an accurate brightness within a frame time. Considering a high-resolution and high-frame-rate display, the addressing time for each row is extremely short. In general, the driving timeline of a self-emissive display consists of three stages: compensation, data input, and emission.

During the compensation period, the driving circuit detects the variations of each TFT, device, etc., and precisely modulates the corresponding driving current for each device to improve its image uniformity. At data and emission stages, compensated driving data is delivered to each pixel, and then at emission stage devices are turned on. The image performance under various compensation time (2, 4.3, and 33.3 μs) is illustrated in Fig. 19(a). The presently developed compensation pixel circuits with progressive emission, as Fig. 19(b) depicts, need to execute the compensation and data input operations within the line time. Here, we take a 120 Hz FHD (1920×1080) OLED as an example, which has a line time of 4.3 μs (=1 s/120/1920), so the compensation time in progressive emission approach must be less than 4.3 μs, e.g., 2 μs. It is clearly shown in Fig. 19(a) that when the compensation time is reduced, the compensation performance degrades, resulting in a non-uniform image. To resolve this issue, several compensation methods including simultaneous emission (Fig. 19(c)) [178–180], block emission (Fig. 19(d)) [181], parallel addressing (Fig. 19(e)) [182,183], and external compensation, have been proposed to extend the time for compensation.

For the simultaneous emission method, all the pixels are compensated at the same time and then data voltages, which are determined by the desired images, are input to pixels row by row. Finally, all pixels are turned on simultaneously. Because the compensation and data input operations are separated, the compensation time is adjustable and not restricted by the line time. When the line time decreases with the increased frame

Figure 19

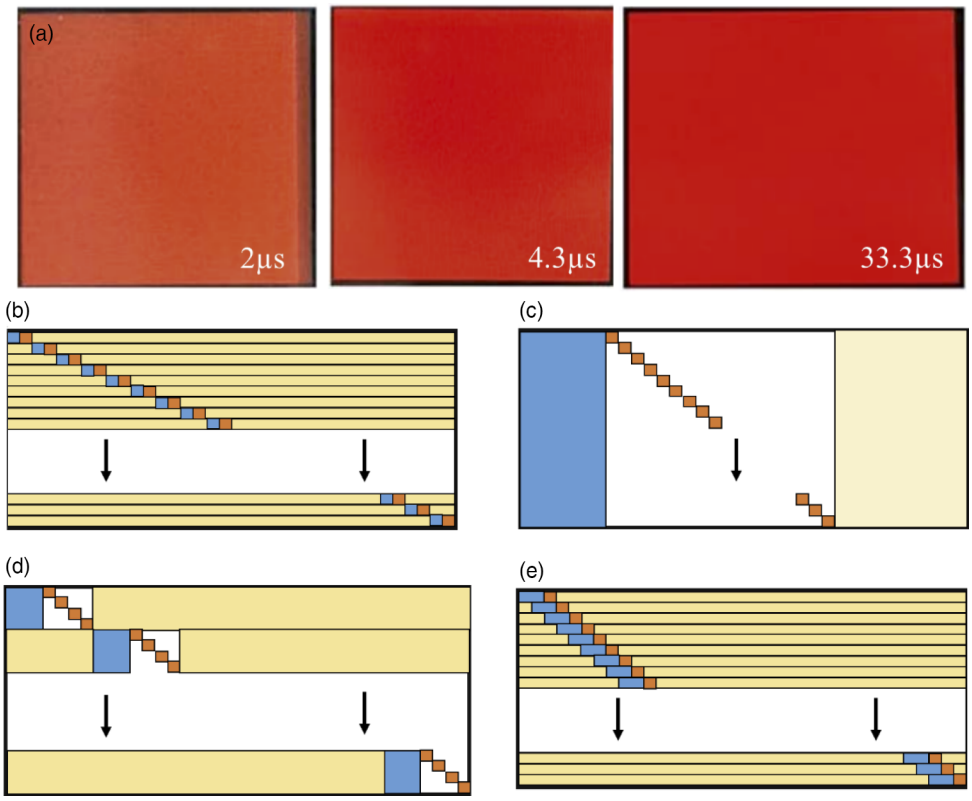

(a) Displayed image of an OLED panel with different compensation times. © 2019 IEEE Solid-State Circuits Society. Reprinted, with permission, from Lin *et al*., IEEE J. Solid-State Circuits **54**, 489–500 (2019) [184]. Driving diagram of (b) progressive emission, (c) simultaneous emission, (d) block emission, and (e) parallel addressing.

rate, simultaneous emission can still yield an excellent performance of compensation to enhance the image quality. However, this method has less emission time than the progressive emission method, resulting in lower luminance. In addition, global signals that are shared by all pixels are commonly used in the simultaneous emission method. Once these signals are activated, all pixels are turned on and illuminated at the same time, increasing power consumption, and generating a large current to flow through the parasitic resistance on the power lines. This causes a serious drop in voltage, which in turn degrades the image uniformity.

To extend the emission time for the reduction in the generated currents, the block emission method, which combines the simultaneous emission and progressive emission methods, has been developed. The block emission method divides the whole panel into N blocks, and each block contains pixels of M rows where $N \times M$ is the total number of the row lines. The operation of pixels in each block is the same as the simultaneous emission method, ensuring sufficient compensation time. Each block is activated sequentially, which is the same as the progressive emission method, enabling that the emission time using the block emission method is longer than the simultaneous emission method. Consequently, adopting the block emission method has not only enough compensation time but also longer emission time, which helps improve the image quality. Nevertheless, a cross talk occurs between each block due to the parasitic capacitor of the adjacent pixels, causing the Mura defect. The phenomenon is more severe especially for those high PPI displays.

In contrast, the parallel addressing method also divides the compensation operation from the data input operation, and no data voltages are used for the compensation, enabling that the compensation time of adjacent pixels to overlap and be adjusted to a proper duration for a better compensation performance. As the frame rate increases, the compensation using parallel addressing method does not need to complete within a shorter line time, acquiring an adequate time to provide an accurate compensation. Therefore, the high uniformity of images is ensured despite the high frame rate of displays. Nevertheless, more components including TFTs and capacitors, and more complicated control signals are utilized to implement the parallel addressing method. In general, it requires about six to seven transistors, which is almost doubled as compared with the other three driving methods. Therefore, parallel addressing method may increase the difficulty for achieving high pixel density and decrease the stability of the pixel circuits. In addition to the compensation by the internal pixel circuits, another approach is to use external compensation. The external compensation uses a detection circuit out of the internal pixel with compensation algorithm to make driving currents uniform. Therefore, the structure of internal pixels can be simplified. This method performs compensation when displays are offline, so its compensation time is independent of the line time, making the external compensation to provide an accurate compensation even though the frame rate is greatly increased. However, the required algorithm is complicated and additional memories are needed, which undoubtedly increases the complexity and cost of the display system. The above-mentioned methods can deal with the issue of insufficient compensation time for use in high-frame-rate displays, but they have their own problems to be conquered.

5.3. Efficiency

When a microdisplay is used as the light engine for a see-through AR system, high brightness is required due to image washout caused by strong ambient light. In general, the output luminance of the AR systems should be at least 500 nits and 10,000 nits, for indoor and outdoor applications, respectively. If we further consider the light efficiency of the optical combiner (e.g., ~1% for the waveguide approach), the required microdisplay brightness should be up to 1 million nits. This is indeed the case for some commercial prototypes demonstrated. On the other hand, for VR systems, since ambient light is blocked by the enclosure, the desired brightness on the viewer's end is usually set at about 150 nits. However, to eliminate motion blur, a small duty emission ratio of 10–20% is commonly used, which means the OLED or LCD panels should provide 10 times the instantaneous display brightness. In addition, considering the 75% optical loss of a decent pancake VR display, the display should be a further four times brighter. Therefore, microdisplays of about 6000 nits are required. To deliver enough brightness in an AR/VR system, the overall efficiency of the projection system should be improved. Otherwise, the limited capacity of battery would significantly restrict the device operation time. In an AR/VR system, the light emitted by the display is first received by the projection system to generate an enlarged image for the HVS. Here, we separate the display system into two categories: one is panel-based display devices and the other is scanning display. Now, let us first focus on the efficiency of panel-based projection systems. The optical efficiency of a system depends not only on the efficiency of the panel itself, but also on the proportion of emitted light collected by the projection system, which could be estimated and defined by the well-known étendue conservation [185]. As shown in Fig. 20(a), the étendue of the projection system in AR/VR displays can be defined by the FoV of the display system and the surface area (A_{EP} in Fig. 20(a)) of the eyebox (VR displays) or optical combiner (AR displays). On the other hand, the étendue of the display panel may be determined by the product of the display radiation pattern and the display surface area. The bottom part of Fig. 20(b) shows the broad emission cone display typically produced by an OLED

Figure 20

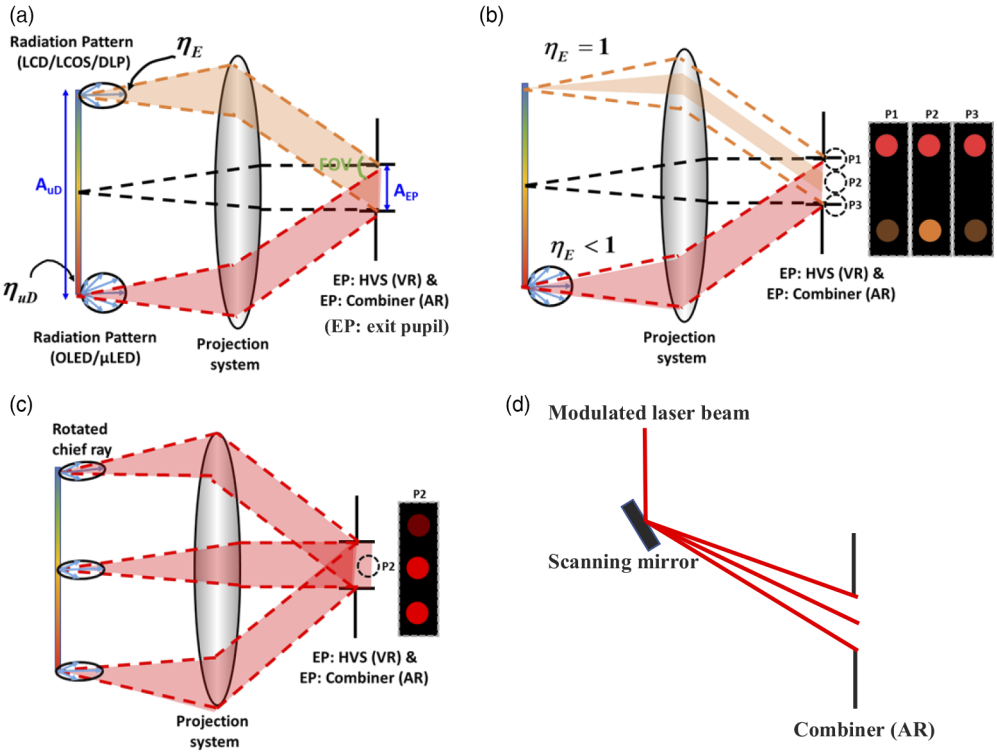

(a) Étendue definition in a projection display system. (b) Schematic of applying broad (bottom part of display) and narrow (top part of display) emission cone display in a projection display system. (P1, P2, and P3 indicates top, center, and bottom pupil position, and its corresponding received image is shown in the right.) (c) Schematic of matched (top part of display) and unmatched (bottom part of display) display chief ray with a projection display system. (d) Schematic of a LBS projection display system.

or μLED display. On the other hand, the upper part of Fig. 20(b) shows the narrow emission cone display typically produced by LCD, LCOS, and DLP. For the broad emission cone display (red light path), the étendue of the display is greater than the étendue the projection system, i.e., part of the light emitted by the display is wasted, which means that the coupling efficiency is less than 1. The benefit is that it provides uniform brightness in the different pupil position within the entrance pupil area. On the other hand, for the narrow emission cone display (orange light path), the étendue the display is less than that of the projection system, and the coupling efficiency is 1, which means that there is no power loss during coupling, but the brightness of the display will change as eye saccades in the entrance pupil area. Therefore, the optimal design of the projection system is to match the étendue of the display panel and projection system to maximize the optical efficiency without compromising image quality. In Figs. 20(a) and 20(b), a telecentric projection system is used. However, in some projection systems, because telecentric design is not employed, the chief rays of the projection system's display emission and reception cones may not match at the edges of the display panel, as shown in Fig. 20(c). In such projection display systems, the radiation pattern of the display should be locally modulated to match the corresponding receiver cone to maximize the optical efficiency [52,186].

For the panel-based projection systems, the overall efficiency of the projection system can be defined by

$$\eta = \eta_{uD} \times \eta_E, \tag{8}$$

where η_{uD} is the optical efficiency of the display panel and η_E is the coupling efficiency between the display panel and the projection system.

Furthermore, for a self-emissive display (OLED and μLED), the optical efficiency of the display panel is determined by

$$\eta_{uD} = \eta_{LED/OLED} \times \eta_{color} \times T_{film}, \tag{9}$$

where $\eta_{LED/OLED}$ is the optical efficiency of the emissive devices and T_{film} is the transmittance of the optical films. Color filters are employed in a white OLED to generate RGB colors and in QD-based μLED displays to purify colors. Depending on the spectral match between the color filter transmission spectra and the device emission spectra, varying degrees of optical loss may occur. For RGB OLEDs and RGB μLEDs, color filters are not usually needed, leading to a higher η_{color}.

For the non-emissive display, the optical efficiency of the display panel is determined by

$$\eta_{uD} = \eta_S \times \eta_I \times \eta_p \times \eta_m \times \eta_{color} \times T_{film}, \tag{10}$$

where η_S is the efficiency of the illumination source, η_I is the efficiency of the integrator, η_P is the polarization management efficiency, η_m is the optical efficiency of the light modulator (LCD panel or DMD), and η_{color} is the color-generating efficiency. More specifically, the integrator efficiency represents the optical losses during light shaping and homogenization, such as in LCD backlight units, and in integrator rods and fly-eye lenses in LCOS/DLP microdisplays. The polarization management loss is due to the polarizer in the illumination system that generates polarized light for the LC device. Novel compact polarization recycling systems help reduce polarization management losses. The optical efficiency loss of light modulators may come from diffraction, reflection, a limited fill factor, and so on. In LCDs, color filters are used to generate colors, leading to about two-thirds optical loss. For LCOS and DMD, color sequential operation is adopted to eliminate color filters, leading to a higher η_{color}.

Different from panel-based projection displays, the LBS microdisplay usually does not require the collimation or projection lens in an AR display [187], as shown in Fig. 20(d) Therefore, the overall efficiency η is equal to the efficiency of the LBS η_{uD}. For the AR based on a waveguide combiner, the scanned laser beam can be directly coupled into the waveguide via an input coupler because the pixel in the LBS is already in the angular domain. The LBS can also enable the Maxwellian display based on a free space combiner [36], thus exhibiting a focus-free advantage [188]. To summarize, the small étendue of the LBS helps minimize the coupling loss. In the remaining section, we focus on reviewing the optical efficiency of each light engine based on the above parameters.

5.3a. LCD

LCD has been developed for decades, but its low optical efficiency has always been the Achilles heel. Fortunately, many methods have been proposed to solve this issue. For example, dual brightness enhancement films are employed to increase the polarization management efficiency by 60%, and optical losses in CFs can be mitigated by QDs with narrow emission spectra. In addition, brightness enhancement films are used to concentrate the emitted light onto the desired viewing cone, much like what we desire to do in projection systems, matching the display's emission cone to the projection system's acceptance cone. Based on the topic of this review paper, here let us pay special attention to the LCDs used in AR/VR display systems. In AR/VR display systems, the requirements for high-resolution density and fast-response LC panels, results in small aperture ratios and dead zones, respectively. As a result, compared

Figure 21

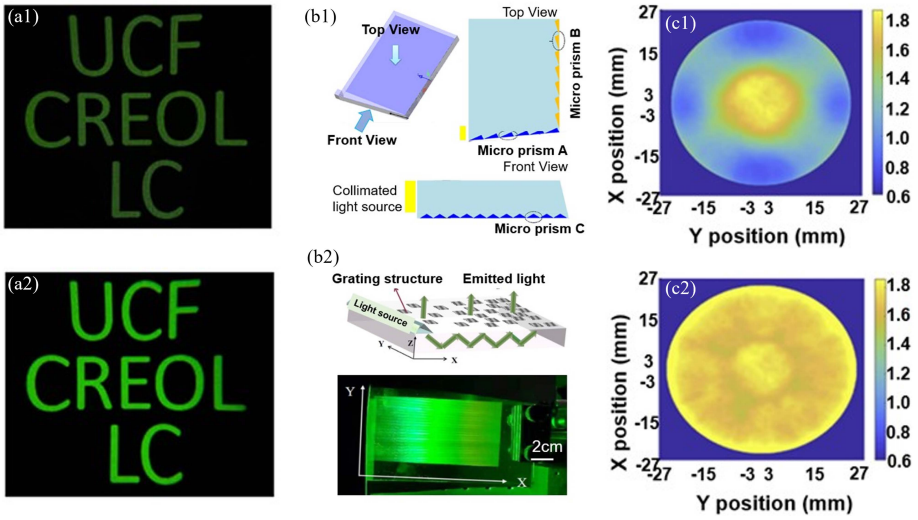

Imaging results of a Fresnel VR system with (a1) conventional BL and (a2) directional BL at center fovea. (a1) and (a2) Reprinted with permission from [189]. © The Optical Society (b1). Device structure of a directional backlight unit consisting of three microprism structures on three surfaces of light guide plate. Reprinted with permission from [190]. © The Optical Society. (b2) Directional backlight unit consisting of grating structure with different spatial densities on top of light guide plate for directional extraction of light. Reprinted by permission from Opt. Commun. **459**, Zhang *et al*., Directional backlight module based on pixelated nano-gratings,125034, Copyright 2020 [191], with permission from Elsevier. The optical efficiency distribution of a Fresnel VR system (c1) without and (c2) with a spatially radiation pattern modulator. (c1) and (c2) Reprinted with permission from [186] © The Optical Society.

with conventional direct-view LCDs, the LCDs intended for AR/VR systems are much less efficient.

On the other hand, compared to conventional LCDs, the fixed eyebox region in AR/VR systems also provides a chance to improve the coupling efficiency. The small pupil size of HVS constrains the étendue of the projection system, so only a narrow emission cone can finally be received by the HVS. Figure 21(a) compares the displayed image of a VR headset with a LCD light engine implementing directional or conventional backlighting [189]. The LCD light source with a directional backlight shows brighter images. The directional backlight unit can be achieved by applying microlens arrays (MLAs), micropyramid films, or reflective microstructures. As shown in Fig. 21(b1), Wang *et al*. [190] proposed a directional backlight by using microprism arrays, whereas as shown in Fig. 21(b2) Zhang *et al*. [191] demonstrated a grating method. The collimated light source is steered into the lightguide plate, and then the traditional scattering particles are replaced by the surface relief grating (SRG). The grating pitch is designed to diffract the light in lightguide upward to surface normal. Moreover, the density of the grating increases from the near side to the far side of the light source to keep a good brightness uniformity. The angular divergence is 6.17°, and the brightness uniformity exceeds 90% for a phone-sized backlight unit. Recently, Maimone and Wang [52] demonstrated holographic films based on emissive backlights for a compact VR system. In this application, a light beam from a point source at the edge of the lightguide propagates, and it is diffracted by the holographic films in the lightguide to form an extended source. Furthermore, Fig. 21(c1) illustrates that in a

VR display system without a telecentric design (Fig. 20(c)), because the acceptance cones of the projection systems are spatially different, applying a directional backlight in a VR display system may result in a severe vignetting effect, which indicates that in a projection system, pixels in the center of the display may appear brighter than those at the edges. In 2021, Hsiang *et al*. [186] proposed a patterned inverted prism film for spatially modulating the radiation pattern of the LCD backlights to locally match the chief ray of display and projection system. Figure 21(c2) illustrates that they could obtain uniform optical efficiency distribution (without vignetting effect) from the center to the edge of the display panel. Notably, the complicated backlight unit of LCD provides room for modulation of the display radiation pattern before the pixel-defining layer. As a result, image quality can be better maintained than modulating the display radiation pattern after the pixel-defining layer typically used for OLED or μLED displays.

5.3b. OLED

A high-brightness OLED device with a high driving current density usually suffers from shorter lifetime and image burn-in issues. Thus, there is urgent need to develop high-brightness OLED [192] with a low current density so that its lifetime can be extended to a reasonable range. The total efficiency of an OLED device is governed by two factors: internal quantum efficiency (IQE) and LEE. The IQE of an OLED device is mainly determined by the emission mechanism of the emitter, such as a fluorescence emitter (IQE ~25% (single) or ~75% (triple)), phosphorescence emitter (~100%), and thermally activated delayed fluorescence emitter (~100%). Considering high-quantum-yield emitters and their reasonable lifetimes, high-IQE OLED devices typically use fluorescent emitters for blue color and phosphorescent emitters for green, red, and other colors. As the IQE of OLED devices has approached 100%, recent research has focused on improving the LEE of OLED devices, initially limited to 20% due to TIR. For an OLED microdisplay, due to the opaque silicon backplane, the OLED devices must be a top-emitting device. Furthermore, to display clear and sharp images, the added light extraction components should not sacrifice the resolution density of the microdisplay. For a top-emitting OLED, the strong cavity effect formed by the top and bottom metal electrodes leads to a large surface plasmon polariton (SPP) mode lost (air mode ~25%; waveguide mode ~35%; SPP mode ~40%) [193]. Several methods, such as scattering layers, MLA, and corrugated structures, have been widely used to extract the power from OLEDs in waveguide and SPP modes [77]. Scattering layers are widely used in OLED devices for lighting applications, which consist of nanoparticles, reflective diffusers, or nanoporous films to break the TIR and to extract the substrate or waveguide mode [194–196]. However, for high-resolution-density displays, image blurring caused by the scattering layers is the most critical issue. Furthermore, scattering layer widens the emission cone of the OLED display, approaching the Lambertian distribution, which is also undesirable in projection display systems.

A MLA can be laminated directly on the top electrode of OLED devices to extract the waveguide mode or on the top glass to extract the substrate mode. However, the former approach may damage the vulnerable OLED devices and require a high-refractive-index MLA to match the high-refractive-index organic materials or ITO, whereas the latter method may result in server blurred images due to a thicker substrate. Laminating a MLA onto a microdisplay is much more challenging than using it in traditional displays or lighting apparatus [197,198]. For traditional displays, one OLED device corresponds to an array of microlenses. In contrast, for microdisplay applications, because the light-emitting area of each OLED device is very small (~μm), the microlens size should be in the same level. In other words, one microlens

will correspond to one OLED device. In addition, a microlens with high aperture ratio, high aspect ratio, and small gap between the emissive layers is required to reduce cross talk and to maximize efficiency. Sony [199] proposed to assemble an inverted microlens above a top-emitting OLED device, which not only increases the brightness in normal direction by a factor of 1.8 (Fig. 22(a1)) but also reduces cross talk between subpixels. Furthermore, as shown in Fig. 22(a2), the offset between microlens and OLED subpixel shifts the chief ray of the emitted light by ±20° from the center [200]. Therefore, by optimizing the arrangement between the microlens and OLED subpixels, spatially different radiation patterns can be achieved for improving the overall optical efficiency and image quality of the OLED projection display system. Finally, the OLED projection system with >1,000,000 nits (green light) has been demonstrated (Fig. 22(a3)). Another approach is corrugated structure. Figure 22(b1) shows the device structure of a corrugated OLED [201]. The main challenge of the corrugated structure is that even though the corrugated structure can efficiently extract the trapped waveguide and SPP modes through Bragg diffraction, the corrugated structure simultaneously weakens the cavity effect due to its low reflectivity. Moreover, the extracted waveguide and SPP modes cause a fierce angular intensity variation (Fig. 21(b2)) [202].

In a projection system, a higher LEE does not mean a better outcome. Preferably, we only want to extract the emitted light of the display whose emission cone falls into the acceptance cone of the projection system; the other light extracted outside the acceptance cone of the projection system will become stray light, which may degrade the image quality. Therefore, how to realize OLED devices with directional angular intensity distribution is a hot topic. There are two main approaches: one is to increase the reflectivity of the top cathode through the DBR layers to obtain a stronger cavity; the other is to optimize the thickness of each organic layer to achieve a highly direct-emitting OLED device (Fig. 22(c1)) [203]. Although the higher the intensity of the microcavity, the more concentrated the light is in the normal direction, the EQE of the OLED device first increases and then decreases. Therefore, Hsiang *et al*. [186] systematically optimized OLED devices to achieve high efficiency, high color gamut, and low color non-uniformity for VR display applications. The second is to design the cavity of the OLED device with strong waveguide mode first, and then to eliminate the air mode, and then use the nanostructure to form Bragg diffraction to extract the waveguide mode with an extremely narrow emission cone to the normal direction (Fig. 22(c2)) [204].

Multiple emissive layers (RGB layers or BY layers) can be used to realize a white light emitting OLED device [205]. The electrons and holes of the OLED device are injected from the cathode and anode, respectively. The thicknesses and electron/hole mobilities of the different emissive layers determine the recombination rates of different emissive layers. For example, due to the low hole mobility of the blue emissive layer, most of the recombination is close to the bottom blue emissive layer (near the anode) and results in an undesired emission spectrum with dominant blue light and insufficient green and red lights. Therefore, to achieve electron–hole balance and desired white light emission spectra, the exciton recombination rates of different emission layers should be carefully designed by adjusting the thickness and position of each emission layer and intercalation interlayer. Furthermore, from the driving voltage perspective, a p-type doped hole injection layer (HIL), and a thinner emissive layer with low hole mobility, are required to reduce the overall operating voltage. After the device configuration is optimized, the *L*–*I*–*V* curves and emission spectra of the multilayer WOLED are shown in Fig. 23(a). The current efficiency is 6 cd/A, and the brightness at 3.3 V is 4200 nits, which is about 100 times higher than the initial state.

Figure 22

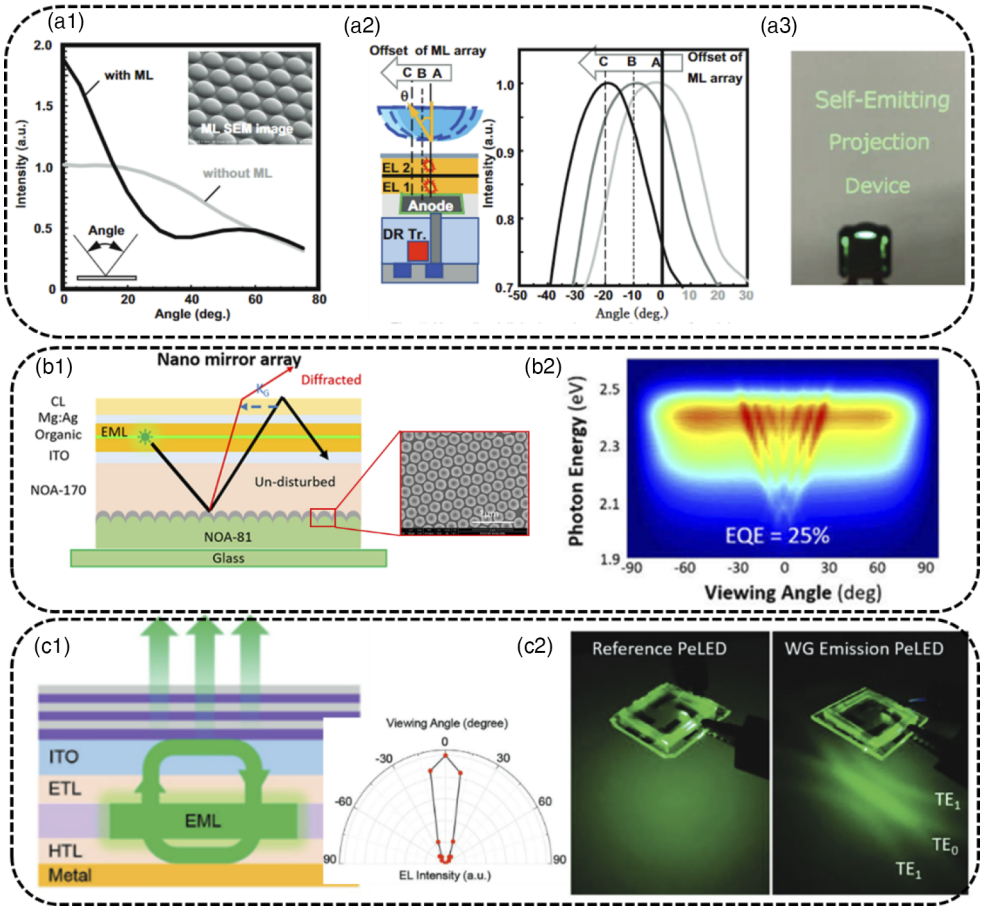

The optical performance of microlens OLED devices: (a1) efficiency improvement; (a2) radiation pattern shift by offset microlens; and (a3) projected image of green writing. (a1)–(a3) Reprinted from Itonaga *et al.*, SID Symp. Dig. Tech. Pap. **51**, 683–686 (2020) [200]. Copyright Wiley-VCH Verlag GmbH & Co. KGaA. Reproduced with permission. (b1) Schematic and (b2) radiation pattern of a corrugated OLED (inset: SEM image of the corrugated structure). (b1) Reprinted with permission from Amoah *et al.*, ACS Appl. Mater. Interfaces **14**, 9377–9385 (2022) [201]. Copyright 2022 American Chemical Society, https://doi.org/10.1021/acsami.1c21128. (b2) Reprinted with permission from [202] © The Optical Society. (c1) Schematic of resonant OLED devices (inset: radiation pattern of resonant OLED devices). Reprinted from Liang *et al.*, Adv. Opt. Mater. **10**, 2101642 (2022) [203]. Copyright Wiley-VCH Verlag GmbH & Co. KGaA. Reproduced with permission. (c2) Spatial patterns from a conventional OLEDs and a waveguide emission OLEDs. Reprinted from Fu *et al.*, Adv. Mater. **33**, 2006801 (2021) [204]. Copyright Wiley-VCH Verlag GmbH & Co. KGaA. Reproduced with permission.

Tandem OLED devices have long been widely used for TV applications. When a voltage is applied, the current-generating layer generates an extra pair of electron and hole, so when more OLED devices are connected in series, more carriers are generated to improve the current efficiency (cd/A). For example, OLEDWorks [84] demonstrate 3-stack, 4-stack, and 5-stack tandem WOLED devices with current efficiency of 12 (cd/A), 15 (cd/A), and 20 (cd/A), respectively. Thus, a tandem OLED device exhibits a higher peak brightness and longer lifetime in comparison with the single-layer OLED because it can deliver higher optical power by a lower current density. But the driving

Figure 23

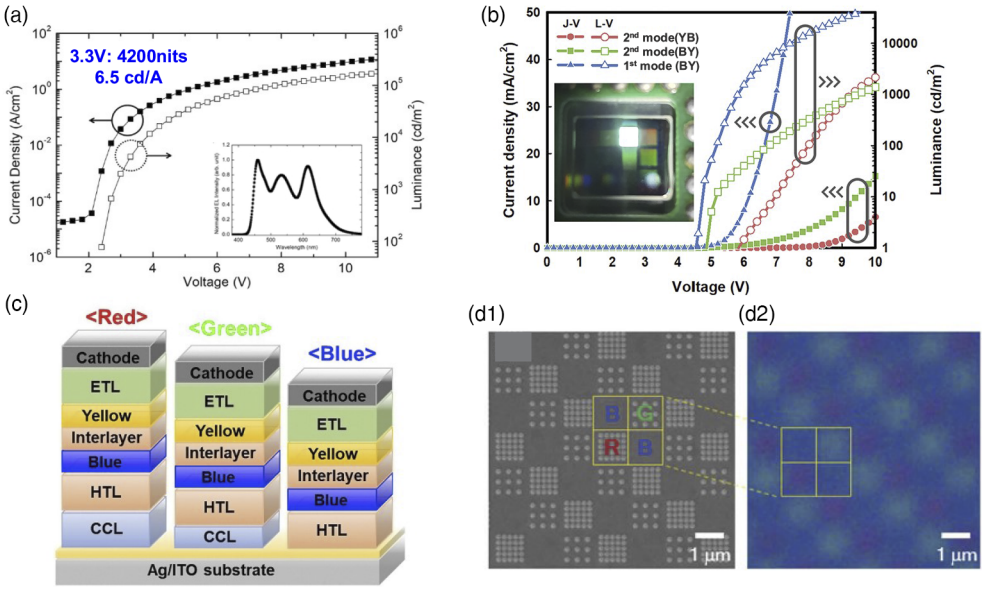

(a) Optical performance of OLED devices with optimized interlayer thickness. (Inset: the emission spectra of the optimized OLED devices.) Reprinted with permission from Lee *et al*., J. Ind. Eng. Chem. **105**, 132–137 (2022) [205]. © 2022 The Korean Society of Industrial and Engineering Chemistry. (b) Optical performance comparison of tandem OLED devices with thin and thick cavity designs. Reprinted with permission from Bae *et al*., ACS Appl. Electron. Mater. **3**, 3240–3246 (2021) [208]. Copyright 2021 American Chemical Society, https://doi.org/10.1021/acsaelm.1c00406. Schematic of OLED devices with customized resonant cavity by RGB devices with (c) different IZO (CCL) thicknesses and (d1) different reflective metasurface. (d2) Photoluminance image of the metasurface OLED devices. (c) Reprinted by permission from Org. Electron. **87**, Kim *et al*., "Primary color generation from white organic light-emitting diodes using a cavity control layer for AR/VR applications," 105938 [211], Copyright 2020, with permission from Elsevier. (d1) and (d2) Reprinted by permission from Joo *et al*., Science **370**, 459–463 (2020) [214]. © 2020 AAAS.

voltage required to connect OLEDs in series is also proportional to the number of stacks. In a high-resolution-density microdisplay, small transistors limit the maximum operating voltage. To reduce the driving voltage, p- and n-doped transport layers are applied to increase the carrier mobility [206]. However, the side effects of the doped transport layer in electrical cross talk between each subpixel should also be considered [207]. Another way to reduce the driving voltage is to design all the emissive layers to resonate at the first antinode to achieve a thinner device profile as shown Fig. 23(b). Bae *et al*. [208] demonstrated that the driving voltage for achieving 1000 nits was reduced from 9.5 to 5.8 V, despite the lower current efficiency of a thin OLED device. If we set 9 V as the maximum driving voltage for the backplane, the thin OLED device shows 10 times the brightness. In addition, because the color filter absorbs about 70% of the emitted light from the WOLED device, how to remove CFs or reduce the optical loss of CFs becomes crucial. By resonating the white light emission spectrum of the OLED device to the desired color corresponding to RGB subpixels, the emission spectrum of the OLED device can be matched with the transmission spectrum of the color filter, thereby reducing the light loss caused by the color filter [209–213]. Strong microcavity design in top-emitting OLED devices is a widely used approach to achieve narrow emission spectra. However, unlike conventional RGB OLEDs, which

have a single color in the microcavity, WOLED devices have two or three colors in the cavity at the same time. In 2020, Kim *et al*. [211] proposed to apply different thicknesses of IZO as a cavity control layer (Fig. 23(c)), and Joo *et al*. [214] used a reflective metasurface as a phase modulation layer (Figs. 23(d1) and 23(d2)), both of which successfully resonated RGB lights from WOLED devices. However, due to the wide emission spectrum of the WOLED devices, the color purity is not good enough to completely remove the color filters, but the efficiency is improved.

5.3c. μLED

As the size of a μLED chip decreases, its EQE decreases, indicating that surface defects at the periphery of the LED chip results in a larger non-radiative Shockley–Read–Hall (SRH) recombination. This phenomenon can be evaluated by the ABC model as follows:

$$IQE = \frac{Bn^2}{An + Bn^2 + Cn^3}; A = A_0 + v_s\frac{P}{A}, \tag{11}$$

where n is the carrier concentration, and A, B, and C are the coefficients related to SRH recombination, radiation, and Auger recombination, respectively. In addition, the SRH coefficient (A) consists of two parts: the bulk SRH coefficient (A_0) and the product of the surface recombination velocity (v_s) and the ratio of perimeter to surface area. As the size of LED devices decreases, the ratio of perimeter to surface area increases and leads to a larger non-radiative SRH recombination, and this effect is more severe in LED devices with larger surface recombination velocity [215]. The most common way to mitigate the size effect of μLEDs is to apply dielectric sidewall passivation in the LED chips to reduce defects generated during the etching process. The passivation process is developed for all kinds of μLEDs, such as AlGaInP red LEDs [216–219], GaN blue and green LEDs, and nanorod LEDs [220–222]. In addition, by reducing the ratio of electrode size to LED mesa size or adding a current confinement layer to avoid non-radiative recombination on the sidewalls of the LED chip, the IQE of the μLEDs can also be improved. In addition to the surface defects, studies have been conducted to discuss the influence of device surface recombination velocity on the size effect of the μLEDs. Smith *et al*. [223] analyzed the size-dependent IQE for GaN-based green and blue μLEDs smaller than 10 μm, as shown in Fig. 24(a). It shows that for LED chips >10 μm, blue μLEDs are more efficient than green μLEDs. It is well understood that the low efficiency of green μLEDs (high indium doping) is caused by high defects densities and a strong quantum-confined Stark effect. Surprisingly, however, blue μLEDs are less efficient than green μLEDs when the chip size is <10 μm. In other words, the size-dependent efficiency drop for blue μLEDs is more severe than for green μLEDs, and it can be explained by the lower surface recombination velocity of green μLEDs [224]. According to the above comparison, both bulk SRH coefficient and surface recombination velocity of the LED device affects the efficiency of the μLED chip, so that a more efficient LED device at a large chip size does not guarantee a better performance as the chip size shrinks. Similar considerations should be taken when determining whether AlGaInP or InGaN μLEDs are more efficient for red μLEDs. High indium doping (>30%) in InGaN red μLEDs result in a high bulk SRH coefficient and a low surface recombination velocity. As a result, InGaN red μLEDs exhibit a low IQE [225,226], but its efficiency is independent of the chip size [227]. On the other hand, AlGaInP LEDs with better lattice matching have low bulk SRH coefficients but high surface recombination velocity [228], which results in high-efficiency red LEDs accompanied by severe size-dependent efficiency drop [229]. Figure 24(b) illustrates the size effect of two types of red μLEDs. The debate persists until now, with both teams improving their devices to achieve the target EQE (5%) for the small μLED chip size (5 μm × 5 μm) [230].

In addition to the size-dependent IQE of μLED devices, the LEE of μLEDs also depends on the die size. An inverted trapezoidal LED chip shape with reflective sidewalls was used in the optical simulation. The small LED chip size improves the interplay between the dipole emission and the oblique sidewall, which redirects the trapped waveguide mode to the air mode. In contrast to the IQE drop, LEE typically increases as the LED chip size decreases (Fig. 24(c)) [231,232]. Like an OLED microdisplay, the directional-emission μLED devices are also favored in the projection display system. Since the 2000s, different types of diffractive photonic crystals (PhC) have been applied on LED devices to extract waveguide modes for a higher LEE [233–235]. By diffracting the guided modes to the normal direction, LED devices with an efficient directional light emission can be realized. However, a thick LED chip (few micrometers) simultaneously supports many guided modes with various in-plane vectors, so a constant reciprocal lattice vector of PhC cannot diffract all the guided modes in the normal direction at same time and achieve non-directional emission. Therefore, the thickness (< 1 μm) of the LED device and the location of the MQW are tailored to concentrate the power into one or two guided modes. Then, PhC is applied to diffract the high-power guided modes to the normal direction, as shown in Fig. 24(d) [236]. Drawbacks of using PhC on LED devices are also evident, such as defects caused by drilling holes on LED devices, and the lower current injection efficiency of PhC LED devices.

Figure 24(e) depicts a parabolic LED chip with reflective sidewalls [237–239]. It is also proposed to concentrate the emitted light in the normal direction. However, the difficulty of fabricating parabolic LED chips below 10 μm remains a challenge. In addition, the parabolic shape design can only work well for the luminescence at the center of the MQW, and the luminescence at the edge of the chip may interfere with the directionality of the radiation pattern. The resonant cavity LED (RC-LED) with strong cavity, resonating the emitted light in the LED device through the high reflectivity upper and lower mirrors, is also used to improve the directivity of the radiation pattern as shown in Fig. 24(f) [240,241]. However, due to the multiple reflections of light back and forth in the RC-LED device, a tiny optical loss in the cavity can eventually lead to a severe efficiency drop. To reduce absorption by metal mirrors, DBR and nanoporous GaN with high reflectivity and low absorption are used to form cavities [242,243]. Furthermore, as in designing a PhC-LED, a thin LED device also needs to limit the number of resonant modes to achieve a higher directionality radiation pattern.

5.3d. LCOS

To analyze the efficiency of a LCOS microdisplay, we can turn to Eq. (10) to consider all the factors involved. Some general analyses have been discussed above. The operation of a LCOS requires a polarized light. Therefore, the polarization management efficiency η_p is an important part for determining the final efficiency. Next, we focus on the parameters η_m and η_p in the LCOS. We can estimate η_m as follows:

$$\eta_{m,LCOS} = (T_{window})^2 \times FF \times R_{mirror,LC} \times \eta_{diffraction}. \tag{12}$$

In a LCOS device, the window transmittance refers to the transmittance of the cover glass. The fill factor is the fractional coverage of aluminum electrode in a pixel. The gap between pixels can be very narrow (<0.2 μm), leading to a large fill factor (>90%). The reflectance in the LCOS projection system is determined jointly by the mirror reflectance and the LC mode. In contrast, the reflectance in the DMD system is only determined by the mirror. Despite a small gap between pixels, the diffraction still exists because of the formation of amplitude gratings [244]. A great deal of efforts has been made to increase the optical efficiency of LCOS devices. Li *et al.* [138] proposed a double mirror structure to realize a 100% fill factor and to eliminate the

Figure 24

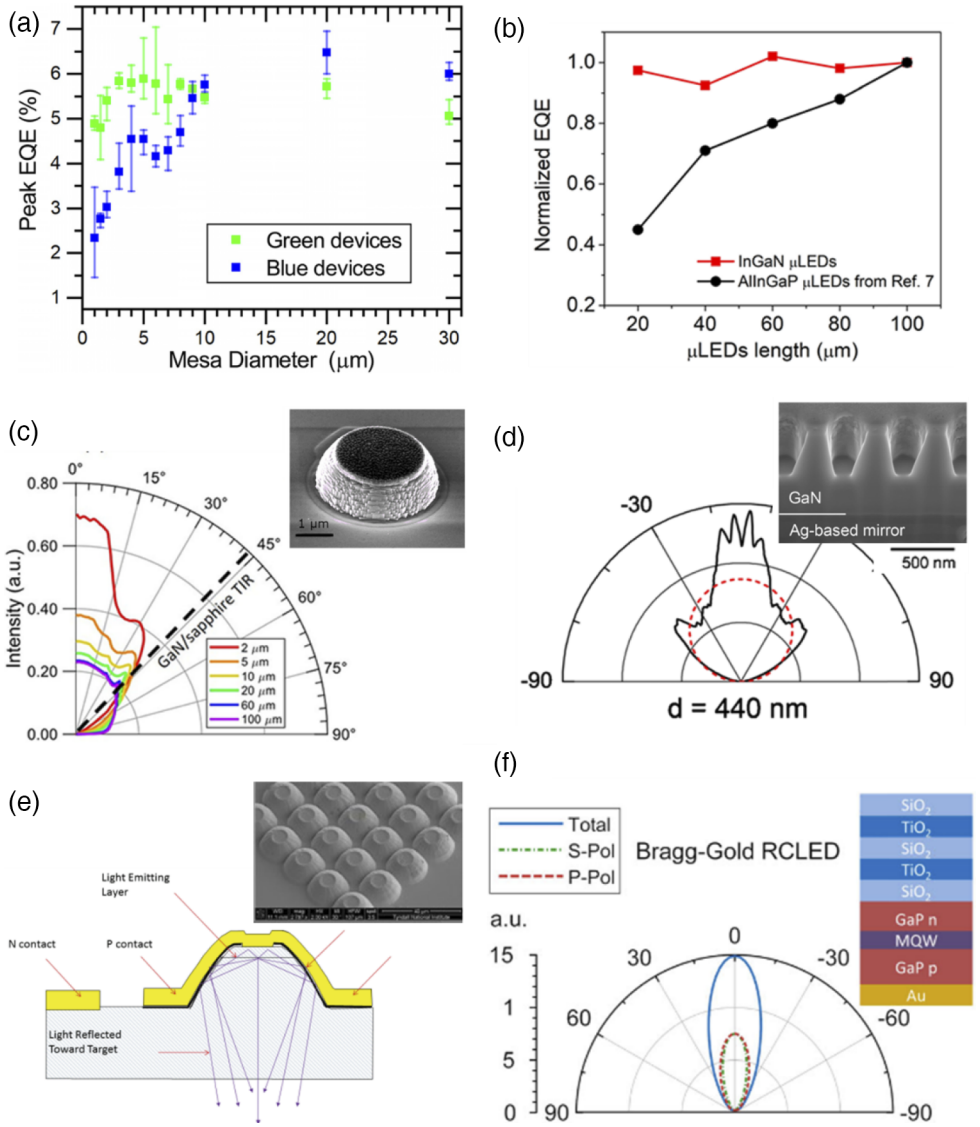

(a) Size effect of InGaN green and blue μLEDs. Reprinted with permission from Smith *et al.*, Appl. Phys. Lett. **116**, 071102 (2020) [223]. Copyright 2020, AIP Publishing LLC. (b) Size effect of InGaN and AlInGaP red μLEDs. Reprinted from [230] under a Creative Commons license. (c) LEE of μLED with different chip size. Inset: SEM image of the μLED chip. Reprinted with permission from Ley *et al.*, Appl. Phys. Lett. **116**, 251104 (2020) [232]. Copyright 2020, AIP Publishing LLC. (d) Directional emission of PhC-LED. Red dashed lines indicate the Lambertian distribution. Reprinted with permission from Rangel *et al.*, Appl. Phys. Lett. **98**, 081104 (2011) [236]. Copyright 2011, AIP Publishing LLC. (e) Schematic of a parabolic surface μLED. Inset: SEM image of the μLED chip. Reprinted from Henry *et al.*, SID Symp. Dig. Tech. Pap. **47**, 747–750 (2016) [238]. Copyright Wiley-VCH Verlag GmbH & Co. KGaA. Reproduced with permission. (f) Schematic and simulated radiation pattern of a resonant LED. Reprinted from Khaidarov *et al.*, Laser Photon. Rev. **14**, 1900235 (2020) [240]. Copyright Wiley-VCH Verlag GmbH & Co. KGaA. Reproduced with permission.

diffraction. In such a device configuration, a bottom mirror is introduced, and the top mirror and bottom mirror are separated by a dielectric layer with a certain height.

Figure 25

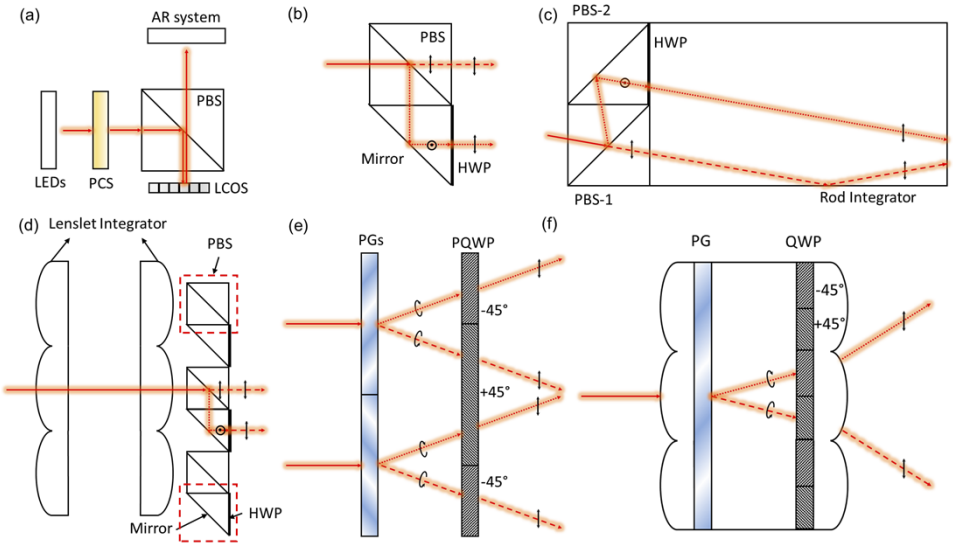

(a) Amplitude LCOS integrated with AR systems. (b) Basic PCS with a PBS. (c) Conventional PCS with a rod integrator. (d) Conventional PCS with lens integrators. (e) complex-ordered PG-based PCS. (f) PCS with a PG and a patterned QWP sandwiched between lens integrators.

Light shining on the pixel electrode region is reflected by the top mirror; light shining on the pixel gap region is reflected by the bottom mirror. In this way, double mirrors behave as a plane mirror instead of pixelated mirrors. Abeeluck *et al*. [166] reported a high-performance LCOS microdisplay with an ultra-small pixel pitch, a fill factor of 93.5%, low diffraction losses and high reflectance. Such a high fill factor can still be achieved at an ultra-small pixel pitch, reducing absorption and diffraction losses. High reflectance arises from an optimized DBR laminated between the backplane and the LC layer.

Most LC devices [245,246], including LCOS, operate based on a polarized light, whereas many light sources are unpolarized, such as arc lamps and energy-efficient LEDs. Polarized lasers are rarely used in LCOS due to the cost issue. One way to obtain polarized light from an unpolarized source is to absorb one polarization by an absorptive polarizer, but it leads to $\eta_p < 50\%$. In general, two approaches are commonly used to improve the conversion efficiency. A polarization recycling system leveraging a RP [247] with hundreds of coatings (e.g., 3M's DBEF) randomize light polarization and contribute to the conversion efficiency statistically through multiple roundtrips. In contrast, a polarization conversion system (PCS) is deterministic, where light only passes through the system once and the orthogonal component follow distinctly different paths. A typical LCOS integrated with a PCS is illustrated in Fig. 25(a). Furthermore, a basic PCS is sketched in Fig. 25(b). Light from the source encounters a PBS and is divided into two beams with orthogonal polarizations (s and p), respectively. The transmitted beam remains its original polarization, whereas the other is reflected by the PBS and passing through a half-wave plate (HWP) orientated 45° to the polarization vector. Thus, all output light shares the same polarization, but the final projected images will suffer from severe luminance non-uniformity, where two bright regions are centered on the top half and bottom half of the output image.

In most cases, a PCS will include either a lenslet or a rod integrator to shape the circular beam to a rectangular format and homogenize the output. A PCS with the combination of two PBSs and a rod integrator [248] is illustrated in Fig. 25(c). The

incident unpolarized light is separated into s and p polarizations by the first PBS and achieves the same polarization after one beam passes through the HWP. Both beams are sent into the mixing rod for uniform illuminance. The rod can be hollow and coated with a highly reflective material, or it may be a solid, and the incident light propagates through TIRs. Owing to multiple reflections, the position of each ray at input and output ports are uncorrelated and therefore the illuminance at the output can be spatially homogenized. Empirically, the uniformity of light intensity distribution is proportional to the length of rod integrator and numerical aperture of the incident beam and is reversely proportional to the beam diameter and refractive index of the rod. Only detailed raytracing with many rays can assure rod design with acceptable uniformity at the output end. Although in theory the rod integrator is not polarization preserving, but in practice the relatively short rod length preserves the polarization well enough and the phase difference between s and p polarizations remains relatively small even at a large incident angle.

In a typical PCS with a lenslet integrator [249] (Fig. 25(d)), the first lenslet array images the source onto the corresponding lenslet in the second array, forming an array of virtual sources. The PBS array and the HWPs split each source into two paths and convert them into the same linear polarization state. Each lenslet in the second array images the lenslet in the first array onto the microdisplay. Although the light distribution of each lenslet is asymmetric, the summation largely cancels each other, and the overlaying creates a much more uniform illumination than each individual lenslet does. Too few lenslets would deteriorate the output uniformity, but too many lenslets could cause the critical alignment issue.

As the form factor of LCOS shrinks down, such a traditional PCS with PBS cannot be simply scaled down accordingly due to its inherent bulkiness and fabrication difficulties. LC-based Pancharatnam–Berry optical elements (PBOEs) are polarization sensitive to orthogonal CP lights and exhibit a high diffraction efficiency [250]. By controlling the 2D pattern of the LC molecular orientation, an arbitrary phase pattern can be achieved, such as polarization gratings (PGs) and PB lenses. A polarization conversion device based on PG was proposed by Du *et al*. [251] in Fig. 25(e). A complex-ordered multidomain LC polymer film is fabricated with photo-alignment technique. Each domain is square-shaped and equally splits into four subdomains of PGs, where each grating vector points to the center of the domain. LCP and RCP lights are spatially separated at a short distance from the polymer film. An additional patterned QWP with ±45° optical axis is placed to convert both CP lights to the same linearly polarized light. Although the device shows ≥90% conversion efficiency, it requires precise alignment. In addition, only highly collimated input light is accepted, and the output illuminance is not uniform. Kim *et al*. [252] demonstrated a compact PCS with a uniform PG and a patterned QWP, sandwiched in a pair of lenslet integrators, as shown in Fig. 25(f). However, the lenslet integrator cannot guarantee a uniform output when the LCOS form factor keeps decreasing.

5.3e. DMD

The DMD belongs to light modulating display; thus, Eq. (10) works for the DLP microdisplay as well. Compared with LCOS, DMD does not require a polarized light, leading to $\eta_p = 100\%$. Therefore, here we only focus on the parameter η_m. According to TI's published white paper [253], η_m can be estimated using

$$\eta_{m,DMD} = (T_{window})^2 \times FF \times R_{mirror} \times \eta_{diffraction}. \tag{13}$$

From Eq. (13), the overall optical efficiency is a product of window transmittance T_{window}, fill factor (FF), the mirror reflectance R_{mirror}, and diffraction efficiency

$\eta_{\text{diffraction}}$. The DMD windows depend on the packaging types: type a uses Corning glass; wafer-level packaging uses Eagle XG glass. Both types adopt anti-reflection thin film coatings to increase transmittance. Let us assume each coated surface has an approximately 99% transmittance. Therefore, the transmittance after a single pass and a double pass will be 98% and 96%, respectively. The fill factor is the fractional mirror coverage (on-state mirrors) as viewed from the illumination direction, which depends on the micromirror size, micromirror gap, and tilt angle. For commercialized DMD products from TI, the typical on-state *FF* is larger than 90%. The *FF* less than 100% causes a small amount of light absorbed and thus reduces the optical efficiency. The third factor is the mirror reflectance. The aluminum-based mirrors employed in the DMD usually exhibit an 89% reflectance in the visible range. Window transmittance, fill factor, and mirror reflectance should be as high as possible to obtain maximum optical efficiency. Diffraction effect in the DMD is a main limiting factor for achieving a higher optical efficiency, which is related to the pixel pitch, fill factor, and incident wavelength and angle. For the flat state micromirrors, the DMD acts as a pure binary amplitude grating because of the gap between the micromirrors. For the on-state micromirrors, the DMD behaves as a coupled amplitude and phase grating because position-dependent phase change is formed because of an inclined configuration [71,254]. For this reason, maximum diffraction efficiency may be achieved by searching a possible "blaze" condition. Recently, Deng *et al.* [255] reported a high single-order diffraction efficiency via optimizing the incident angle of the illumination light. However, the relatively large gap between the micromirrors still poses a constraint on further improving overall DMD efficiency. To summarize, overall DMD efficiency can be estimated by taking the above four factors into account. The total photopic efficiency is approximately 60–70%, depending on the DMD pitch, tilt angle, and f/# of the projection lens.

5.3f. LBS

For the LBS microdisplay, there is usually no projection lens in the AR system. Therefore, the efficiency of LBS is determined by the laser light sources and the MEMS scanner. Developing high-efficiency laser light sources [256,257] and high-efficiency MEMS scanners [258] is critical for the next-generation low-power AR glasses. For the laser sources, RGB laser diodes are employed to generate a color laser beam. In particular, the efficiency of direct emission green diode lasers [259–261] is crucial for long usage time of the AR glasses. It is noted that to assure a fast-switching speed, the lasers still work in the subthreshold current when the pixel is black, thus consuming additional power. In addition to laser sources, the scanning process consumes electrical power as well. The MEMS mirror driver sends electrical signals to deliver the accurate control of the MEMS mirrors. The MEMS mirror(s) can be two separate 1D MEMS mirrors or one 2D MEMS mirror. The 2D MEMS mirror can exhibit a lower power consumption than the two 1D MEMS mirrors. However, the possible cross talk between the two axes is an issue for the high-resolution LBS microdisplay. The methods to actuate the MEMS mirror include electrostatic actuation, electromagnetic actuation, and piezoelectric actuation. Among these three actuation methods, piezoelectric actuation exhibits the highest actuation forces and the highest power efficiency [151]. Recently, Boni *et al.* [262] demonstrated the piezoelectric MEMS mirrors working at the target FoV of $56° \times 32°$ (diagonal 65°). Their measured power consumption was less than 20 mW. Lastly, there is a trade-off between the light source efficiency and the resolution [263]. The light source can be on during the entire pixel time (pixel duty cycle is 1) to maximize the light source efficiency, but the scanner motion during the entire pixel time may blur the spot along the scan direction and sacrifice the resolution.

5.4. High Dynamic Range

HDR displays have been constantly pursued and improved to deliver a better visual experience than SDR displays since the early 2000s [264]. Dynamic range is determined by the peak brightness, contrast ratio, bit depth, and color gamut. The peak brightness of at least 1000 cd/m^2, contrast ratio over 200,000:1, and gray levels more than 10 bits have been proposed as the HDR standard. Many efforts have been devoted to HDR direct-view LCDs such as mini-LCD backlit TVs, desktop monitors, laptop computers, and pads [4,265]. For near-eye displays, it is more challenging to achieve HDR because of additional optical elements are involved [266]. For instance, in an immersive VR headset, the brightness and contrast ratio are jointly determined by the light engine and the imaging lens (Fresnel lens or "pancake" lens). For a see-through AR, the contrast ratio is greatly reduced by the imaging lens, optical combiner, and ambient light. It is challenging to achieve an ACR over 5:1 under strong day light condition. Meanwhile, there is a strict constraint on the weight and volume of the AR/VR devices. For this reason, some HDR methods suitable for large space displays cannot be transferred directly to near-eye displays. Overall, HDR is a critical metric in AR/VR and more endeavors are urgently needed to achieve HDR near-eye displays. In the following, we focus on how light engines help achieve HDR near-eye displays with an emphasis on novel designs and strategies.

5.4a. Dual Modulation Display

To improve the dynamic range of a display system, a dual modulation display system is proposed. Figure 26(a) illustrates a simplified device configuration for a dual modulation display system, where the first modulation panel (subpanel) can be a LC panel without color filters, DLP, LBS or mini-LED array, and the second modulation panel

Figure 26

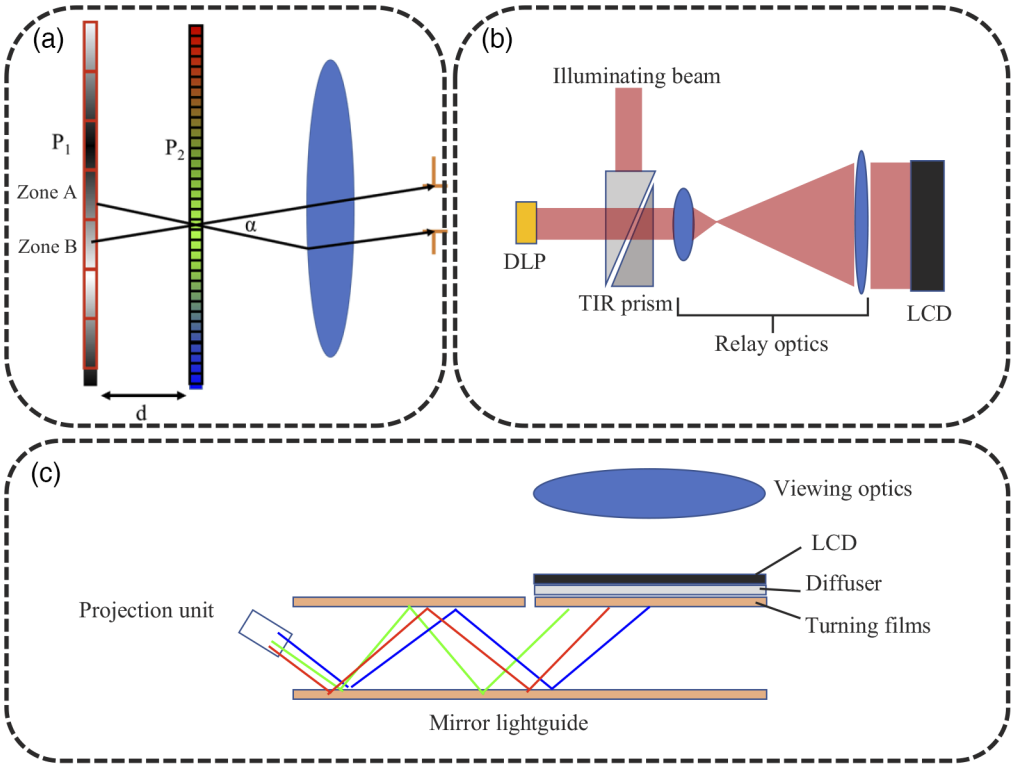

(a) Simplified schematic of a dual modulation display system. (b) DLP-based HDR display system. (c) Folded LBS-based HDR display system.

can be a LCD with color filters (main panel). The severity of visual artifacts mainly depends on three factors: the dimming zone size of the first modulation panel (P1), the distance between the dual panels, and the range of the acceptance cone for the near-eye display (α). Compared with direct-view displays with a tiny viewing cone ($\alpha \sim 0.1°$), the viewing cone in VR display systems is several degrees, resulting in a greater cross talk in the same panel space (d) between subpanel and main panel. For example, as shown in Fig. 26(a), both zone A and zone B simultaneously illuminate the target pixel in main panel and enter the pupil range. Therefore, reducing the dimming zone size of the subpanel (P1) and space between the dual panels is critical to mitigate the visual artifacts caused by dual-modulation display systems. Here, we analyze the pros and cons of three pairs of advanced HDR near-eye displays: DLP microdisplay + LCD; mini-LED array + LCD, and LBS microdisplay + LCD.

(1) Combination of DLP microdisplay (subpanel) and LCD (main panel). As shown in Fig. 26(b), due to the bulky illumination system of the DLP microdisplay, the distance (d) between the two panels is in the millimeter range, so relay optics is used to reimage the intensity distribution on the subpanel to the main panel. However, such a bulky display system is impractical for NED applications.
(2) Local dimming mini-LED array has been widely used as a subpanel for direct-view HDR LCDs, and its compact system configuration is suitable for NED applications. However, Tan *et al*. [267,268] pointed out that when the native contrast ratio of a LC is 2000:1, the viewing cone of the dimming zone should be less than 0.5° to eliminate the halo artifacts. The corresponding dimming zone size is about 400 μm, and the required number of mini-LEDs is about 40,000, which is much larger than advanced mini-LED LCDs with only a few thousand local dimming zones in commercial projects.
(3) To achieve a dual-modulation display system with a high-resolution subpanel and a compact design, in Fig. 26(c) we show a guided LBS projection system that Zhao *et al*. [266] proposed as a subpanel, which eliminates the relay optics, and has a compact form factor. The optical system consists of a projection unit, lightguide, turning film, and a diffuser. The lightguide is a critical element to replace the relay optics and enables a compact form factor via multiple reflections. Tilting the system can further reduce the volume, and the inclined rays will be deflected by a thin turning film composed of micro prisms. Owing to the magnification of the projection system, the numerical aperture of the relayed image of primary modulation is reduced, calling for a diffuser at the secondary modulation to achieve an acceptable eyebox. The superior HDR images achieved by the proposed display system are shown in Fig. 26(c). Overall, research into HDR NED applications is still in its infancy. Many issues still deserve more study, such as halo artifacts caused by an inadequate number of dimming zones, image degradation caused by the cross talk between two panels, cross talk variation during pupil swimming, and compact form factors.

5.4b. HDR Optics

The optics with limited MTF and stray light also cause image degradation in the AR/VR display systems. For example, the folded optics (called pancake eyepiece) has degraded image quality due to stray light (ghost image). To analyze the stray light, the optical path of the pancake eyepiece is shown in Fig. 27(a). Compared with the ideal situation shown in Fig. 3(b), which is composed of ideal CP light and linearly polarized light, the polarization state of the light in an actual pancake eyepiece is composed of elliptically polarized light. It is this undesired elliptically polarized light that causes the straylight, which in turn decreases the image contrast of the VR system. For the

Figure 27

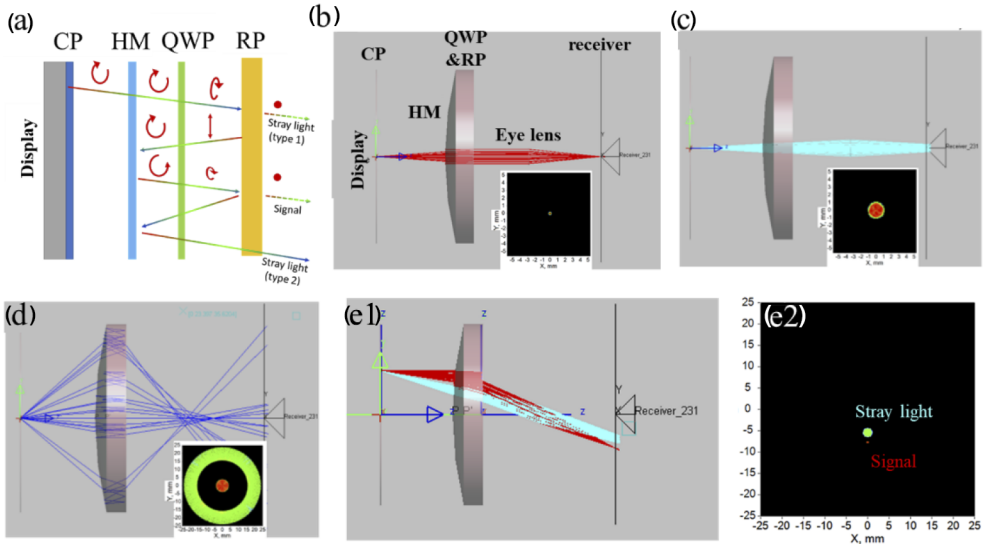

(a) Simplified schematic of folded optics (pancake eyepiece) VR displays. The ray path of (b) signal, (c) stray light (type 1), and (d) stray light (type 2). (e1) Ray path and (e2) intensity distribution of signal, and stray light (type 1). The pixel position is off axis.

display panel, a point source is used to present the light emitted from pixels, and the circular polarizer is laminated on top of the point source to generate the CP light. The point light source from the display panel passes through the pancake eyepiece and becomes a collimated beam. Then, the human eye ideally images the signal beam (Fig. 27(b)) to a point on the retina. The straylight can be distinguished by the time the light travels through the pancake lens. Type 1 straylight refers to the stray light that is not reflected by the RP but passes directly through it (Fig. 27(c)). Compared with the signal beam (Fig. 27(b)) passing through the pancake lens thrice, the straylight passes through the pancake lens only once. Therefore, it has less optical path in the pancake lens, that is, it experiences a smaller optical power. Such an insufficient lens power causes the divergent beam to hit the eye lens, and the divergent beam is focused further away from the retina. In other words, at the retina, the straylight is not a sharp focus point, but a circular illumination area (Fig. 27(c)). Type 2 straylight is reflected twice by the RP and experiences a stronger lens power than the signal light path. As a result, the ray path is focused in front of the retina (Fig. 27(d)). To reduce ghosting and preserve the HDR of the display panel, tailoring the angular distribution of the display panel is an effective solution. Figure 27(e) illustrates that the chief ray of the emission cone of the signal beam and the stray light are different. Therefore, the effects of stray light can be reduced if we can carefully modulate the radiation pattern of the display to match the emission cone of the signal beam and avoid overlapping with the emission cone of the ghost image.

5.4c. HDR LCOS

For the amplitude-modulating LCOS device, the contrast ratio is greatly affected by the FFE. Chiang *et al*. investigated the contrast ratios of five LC modes at different electrode slopes [137]. The contrast ratio is defined as the ratio of the average reflectance at the bright pixel to that at the dark pixel. When all the pixels are turned on and off, the VA mode exhibits a calculated contrast ratio as high as 3300:1 at the electrode slope of 0.3. For most of displayed contents, it is rare to turn on/off all pixels. For the dark/bright/dark pixel configuration, the 90°-MTN mode exhibits a higher contrast

ratio than the VA mode due to a weaker fringing field. In addition to the FFE, the contrast ratio of the PBS, and the $f/\#$ of the projection lens also affect the system contrast ratio. Recently, Abeeluck *et al*. [166] presented an amplitude LCOS microdisplay with about averaged 3000:1 measured by a lens with an $f/\# = 2.5$. In real AR applications, the dynamic range of the outdoor scenes can possibly be as high as 14 orders of magnitude. It is challenging to achieve such a HDR just using a single LCOS panel. For this reason, Xu and Hua [269] proposed a HDR head-mounted display (HMD) based on a pair of LCOS panels, which is composed of a HDR image generator and the viewing optics as shown in Fig. 28(a). In a near-eye display, the spacing between the LCOS panels with the same spatial resolution should be as small as possible to avoid cross talk and to improve the accuracy of dynamic range enhancement. Therefore, the relay optics with a 1:1 magnification was introduced to optically overlay the modulation layers (the gap can be as small as a few micrometers) and thereby enabled pixel-by-pixel modulation on dynamic range. More specifically, a double telecentric relay system was adopted because it can provide uniform illumination, uniform optical magnification, and uniform light efficiency. The LCOS1 was equipped with the LED source and the wire grid film (WGF). The LED source served as the illumination for the HDR image generator, and the WGF generated a high-efficiency linearly polarized light. The LED source and WGF polarizer were removed from the LCOS2. To demonstrate the performance of dual LCOS panels, a HDR image was first synthesized by capturing a HDR scene with different camera exposure time. The HDR scene mainly consisted of a desk lamp and two resolution targets. To display the synthesized HDR image using the HDR-HMD, it was then re-rendered into two low-dynamic-range modulation images. The two modulation images were geometrically corrected and then displayed by corresponding LCOS panels. In this way, the HDR image could be successfully displayed by the HDR-HMD system. Figure 28(b) shows that the details and dynamic range in the HDR scene are preserved. In contrast, they are lost in a low-dynamic-range HMD based on one LCOS panel, as shown in Fig. 28(c). Although the proposed HDR HMD can display HDR contents, it undoubtedly increases the bulkiness and cost of the AR headset.

5.4d. HDR DLP

From a system perspective, several factors such as illumination angle, coating quality, mirror gap, and numerical aperture play significant roles in determining the contrast ratio of the DMD system [72]. Illumination angle greatly affects the distribution and the amount of reflected and scattered light. In particular, as the mirrors are in the off state, there is a larger probability for the light to hit the edges of the mirrors and mirror vias, leading to more scattered light. Coating quality influences the reflected light from all surfaces such as the surfaces of a lens and a prism. The reflected light may travel through the projection lens by a certain optical path, reducing the contrast ratio. Mirror gap determines the diffracted light that may be collected by the projection lens as well. Finally, the numerical aperture of the projection system controls the amount of collected light including stray light. Based on these factors, several strategies have been proposed to increase the contrast ratio [270–274]. A straightforward method is to use dark (non-reflecting) metal layers below each mirror. The reduced reflected or scattered light helps boost the contrast ratio to exceed 1000:1. In addition to dark metal layers, several other methods have also been proposed to improve the DMD's contrast ratio. Meuret [272] proposed two methods to improve the contrast ratio: cutting off the cone of light and shifting the cones of light to larger angles. The reference contrast ratio degraded by the scattering was 430:1, which was simulated by the optical ray-tracing program ASAP. Truncating the light cones with the adjusted aperture stop in the projection lens improved the full-on/full-off contrast ratio to 750:1. For the second method, the full-on/full-off contrast ratio could be improved to 755:1

Figure 28

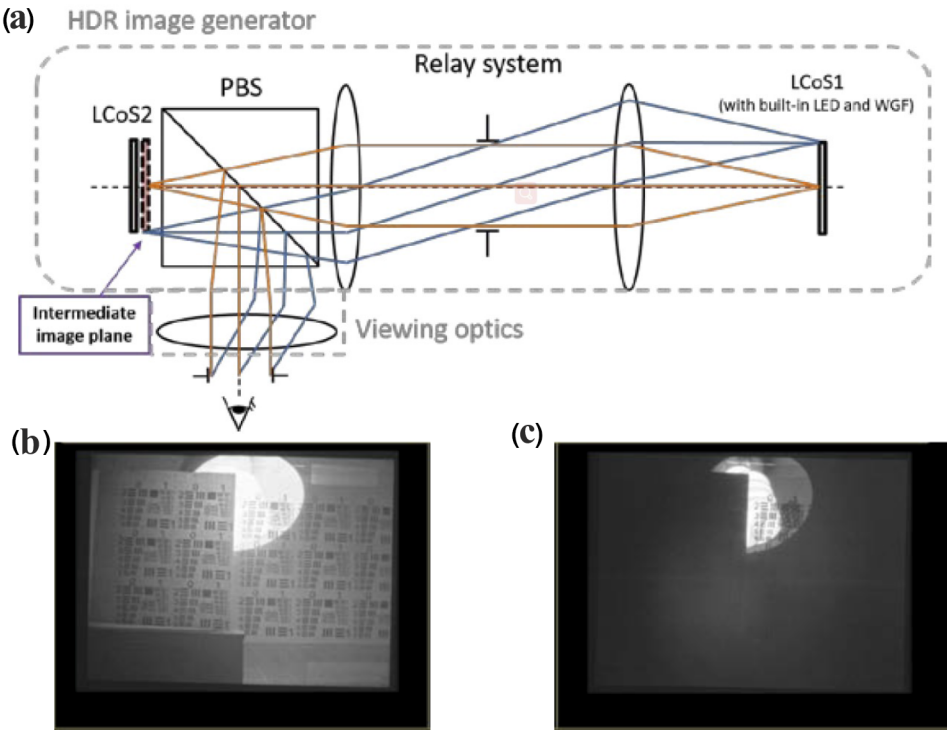

(a) Schematic of a HDR HMD based on dual LCOS panels. (b) Re-rendered HDR image displayed by the HDR-HMD. (c) Low dynamic range image displayed by a low-dynamic-range HMD. (a)–(c) Reprinted with permission [269] © The Optical Society.

by increasing the cones of illumination light by 3° with the well-adjusted asymmetric aperture stop in the projection lens. If we combine any of the two methods with the dark metal layer, a higher contrast ratio can be expected. Later, Pan and Wang [273] proposed a novel prism design to increase the contrast ratio while maintaining the optical efficiency. The prism was composed of three smaller prisms with the same material. The first TIR surface was used for eliminating the interference between the illumination beam and the reflected beam at the on state of the DMD. The image rays directly travelled through the second TIR surface; however, the stray light would be deflected away from the projection lens because of the TIR, thus greatly enhancing the contrast ratio. Ding and Pan [274] designed a freeform surface lens to achieve a high contrast ratio without reducing system efficiency. The freeform surface lens was designed to eliminate the overlap effect between the on state and the flat state caused by the anamorphic phenomenon.

The DMD itself is a binary device; therefore, the gray level is generated by sequentially projecting bit-planes. Traditional PWM poses a constraint on the maximum achievable bit depth due to the exponential relationship between the frame rate and the bit depth. Intensity-modulated light can achieve both high frame rate and high bit depth, but the maximum brightness is greatly sacrificed. Although multiple cascaded DMDs can also increase the bit depth, its efficiency loss, sophisticated calibration, and increased cost limit its widespread adoption. To achieve a high bit-depth DLP microdisplay with high frame rate and high brightness, Chang *et al.* [174] proposed a hybrid light modulation (HLM) by combining PWM and intensity-modulated light as schematized in Fig. 29(a). For the least-significant bit-planes (0–3 in Fig. 29(a)), intensity-modulated light encoded in n_1 bits is applied to alleviate increased exposure

Figure 29

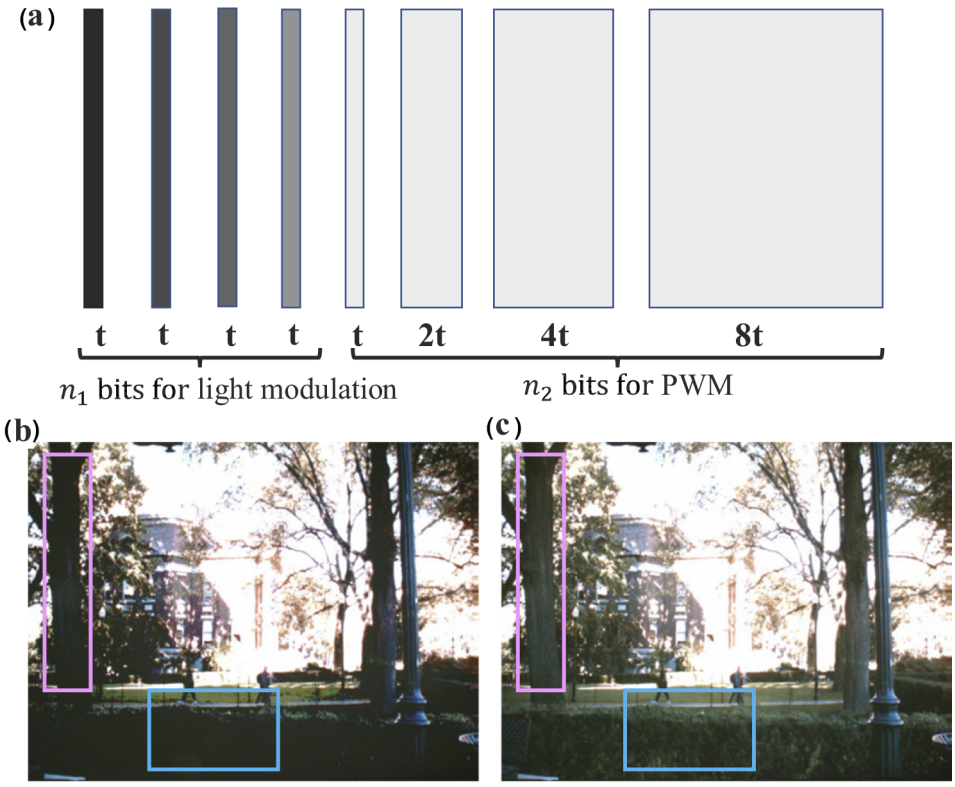

(a) Schematic for realizing an 8-bit gray-scale image with HLM. (b) 8-bit projected image with the traditional PWM method. (c) 16-bit projected image with the HLM method. (a)–(c) Reprinted with permission from [174]. © The Optical Society.

time from PWM; for more significant bit-planes (4–7 in Fig. 29(a)), PWM encoded in n_2 bits is employed to mitigate the brightness losses from intensity-modulated light. The total frame time is $n_1 t + (2^{n_2} - 1)t$, and the maximum averaged brightness can be calculated as

$$L_{\max} = \frac{L(2^{-n_1} + \cdots + 2^{-1})t + t(1 + 2^1 + \cdots + 2^{n_2-1})L}{n_1 t + (2^{n_2} - 1)t}, \tag{14}$$

where L is the maximum intensity of light source used in the PWM, and t is the minimum bit-plane exposure time. Owing to an exponential growth, 2^{n_2} is usually much larger than n_1, leading to $L_{\max} \approx L$. By carefully selecting n_1, the HLM helps achieve a 16-bit depth DLP microdisplay with adequate frame rate and high brightness. A 16-bit image has 16 million times more RGB colors than an 8-bit image, thus preserving more subtle details. Figures 29(b) and 29(c) show an 8-bit projected image using the traditional PWM method and a 16-bit projected image using the HLM method, respectively. The bushes and tree trunks marked in Fig. 29(c) are more visible, demonstrating the advantage of high bit depth. Finally, by combing some strategies to achieve high contrast ratio and the HLM, the DLP microdisplay can simultaneously exhibit high contrast ratio, high bit depth, high frame rate, and high brightness.

5.4e. HDR LBS

The contrast ratio of a LBS microdisplay is mainly determined by the diffraction limitation and scattered light in the optical system [275]. For a dark region surrounded by white regions, the luminance of the dark region is not zero due to the diffraction spread from all the white pixels. A larger mirror size may increase the contrast ratio

by reducing the diffraction, but the dynamic mirror deformation may be increased. Therefore, an optimal mirror size should be searched. The gray level in the LBS is realized by varying the luminance of each pixel. Laser diodes can be directly modulated by the driving current to generate the current-dependent luminance. It is noted that the pixel time at the center and edge of the display is different due to the sinusoidal movement in the horizontal/vertical scan. For central pixels with a shorter pixel time, a higher laser modulation rate is desired, especially for a high-resolution microdisplay. For example, Holmstrom *et al*. [151] calculated the maximum required pixel clock frequency for supporting HD1080 (1920 × 1080), which was about 260 MHz in the bidirectional raster scanning architecture and 60 Hz refresh rate. Although external modulators such as acousto-optic modulators may realize such a high pixel rate, the cost, and the size of the LBS will be increased. Therefore, high-speed laser drivers are still essential, and the maximum achievable bit depth is limited by the laser driver and laser diodes. Recently, Petrak *et al.* [276] presented a LBS microdisplay with maximum supported 10-bit depth and 200 MHz pixel clock frequency. Wide color gamut is another advantage of the LBS [277,278]. The color gamut of the LBS is determined by the central wavelengths of three laser sources and the full width at half maximum of their emission spectra. By employing a green laser source with the central wavelength of 530 nm, its color gamut can be much larger than the sRGB. The green laser sources were realized by frequency doubled infrared laser diodes or direct emission green laser diodes. The latter truly enables a miniaturized LBS microdisplay and accelerates the development of the full-color compact LBS light engine for AR applications. For the LCOS and the DMD systems, the backlight source can be LEDs or lasers. If the laser backlight is adopted, the color gamut of the LCOS or the DMD can be comparable with that of the LBS.

5.4f. HDR OLED and μLED

OLED and μLED emissive displays are current-driven devices, so a pixel circuit is required to generate the desired current to achieve a certain brightness. In the pixel circuit, data voltages that correspond to the desired gray levels determine the magnitude of the driving currents, exhibiting the different luminance. To enhance the quality of HDR, a wider range of data voltage for maximizing display luminance is favorable. On the other hand, an extremely low luminance interval for distinguishing the gray scale of a black image is also beneficial to HDR. Although OLED, mini-LED, and μLED can provide a higher quality of black images, their pixel circuits cannot ensure these devices to be turned off completely. Because each pixel circuit needs to perform compensation in addition to data input and emission operations in each frame to improve the uniformity of the displayed images, a current may flow through these emissive devices during the compensation and data input periods, causing flicker to reduce the dynamic range. Hence, to achieve HDR, the developed pixel circuits should provide no leakage current flowing through such emissive devices except during the emission period when a black image is displayed. Furthermore, after the images are illuminated, there are some charges stored at the emissive devices. Nevertheless, these charges may slightly activate these devices, degrading the quality of the displayed pure black images. To resolve this issue for a higher dynamic range, the charges must be released before each emission. Thus, pixel circuits require to reset the anode or cathode of these emissive devices before the generation of the driving currents. By designing pixel circuits to prevent the emissive devices from flickering, a better quality of HDR can be attained.

5.5. Compactness

The form factor of light engines is much more demanding for AR than VR. Presently, several microdisplay technologies, such as μLED, μOLED, LCOS, DLP, and LBS have

Figure 30

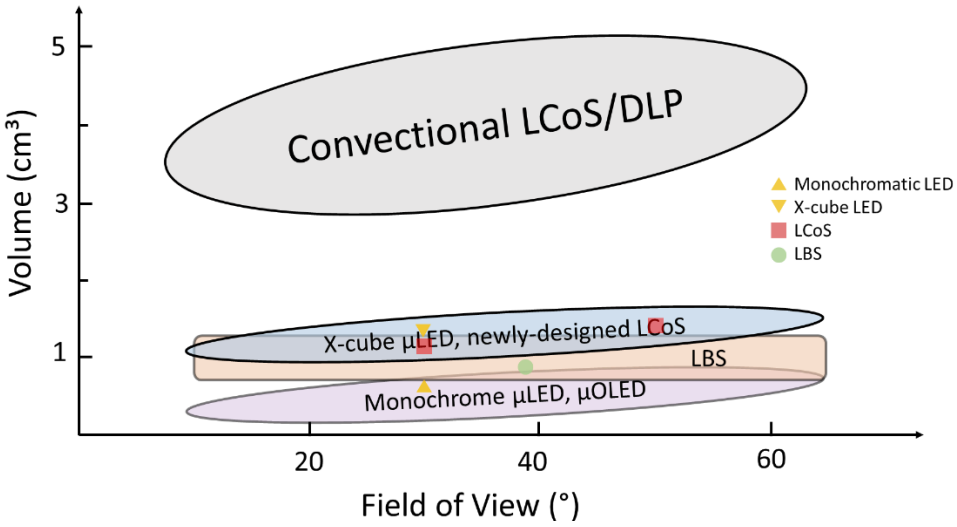

A qualitative comparison of volume size of each light engine in AR at each FoV. Data points of μLED [279], LCOS [280], and LBS [281] are marked out.

been developed for AR. Each technology has its own pros and cons. Figure 30 shows a generic comparison between the volume and the FoV in panel-based displays, and data points of state-of-the-art μLED [279], LCOS [280], and LBS [281] are marked out. Among them, quantum-dot based μLED and μOLED displays are both self-emissive and can achieve very high pixel density and full color on a single panel, which seems ideal for compact light engines. However, the trade-off between brightness and lifetime remains to be overcome for μOLED to extends its application to AR because of the high brightness requirement [282]. μLED aims to preserve all the advantages of μOLED and mitigate the brightness-lifetime issue, but mass production is still in the infancy stage [283]. Although these two panel-based display technologies still have limited market penetration in present AR headsets, they remain strong contenders because the above-mentioned issues are gradually being overcome. LCOS and DLP are both non-emissive panel displays and have reached a matured stage for mass production after decades of investments in standard CMOS technology [170], but an extra illumination system usually leads to a larger form factor. In the illumination system, the light from an external illuminating source (e.g., LEDs) usually needs to be homogenized by passing through a pair of fly-eye lenses or a rod integrator before reaching the LCOS/DLP panel. In a traditional LCOS display [132], a PBS functions as both a polarizer and an analyzer. In the telecentric DLP display [270], a light separator (prism) is employed to direct the uncontrolled beam away from the projection lens. To further reduce the form factor, these bulky optics should be shrunk or even removed. The transmissive LCD, like LCOS, relies on liquid crystal for amplitude modulation, but it uses a backlight illumination. At first glance, the transmissive property seems intriguing to make a simpler optical design, but the lower fill factor (~20% due to black matrices) limits its pixel density to be ~2000–3000 PPI, which is lower than its reflective counterpart (>4000 PPI). On the other hand, LBS consisting of a tiny laser module and MEMS mirrors, has a very attractive form factor and is still pushing its limit, but its frame rate and scanning uniformity remain to be improved. Next, we discuss recent progress in reducing the form factor of LCOS and LBS displays.

A conventional LCOS display consists of a color combiner, a homogenizer, a PBS, and a LCOS panel, as shown in Fig. 31(a). This configuration is referred to as free-space-lit LCOS, because light mainly propagates in free space. Similar to the edge-lit backlight

Figure 31

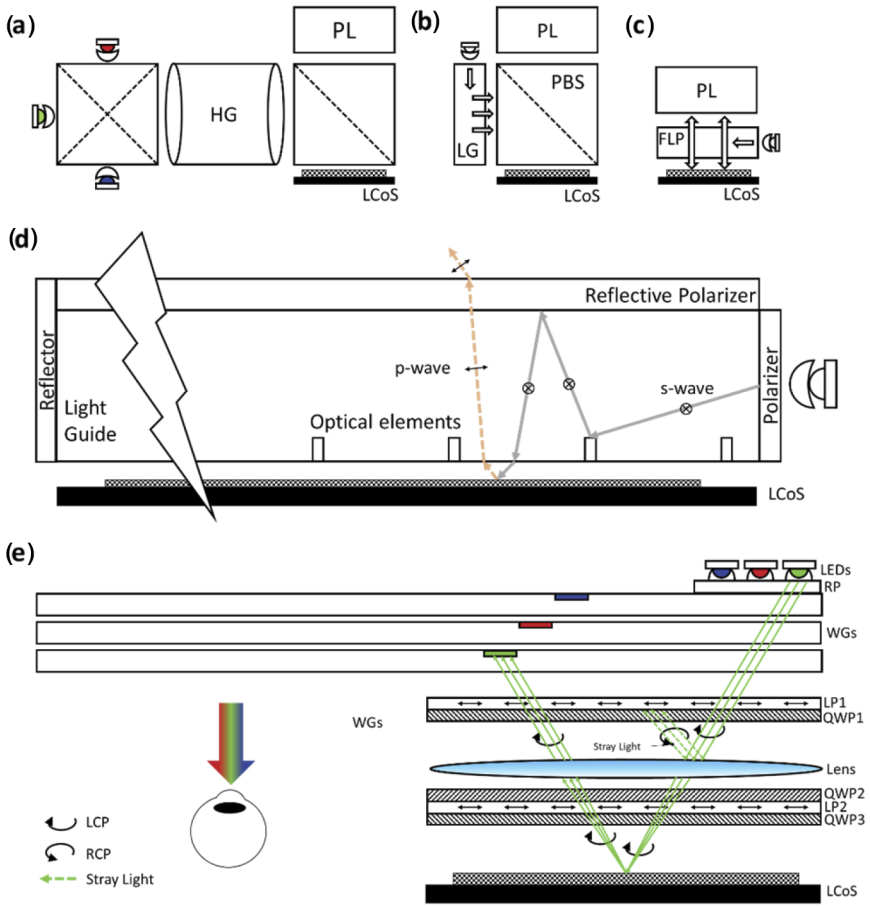

(a) Free-space color-sequential LCOS design with an X-cube, a homogenizer, and a PBS. (b) Backlit LCOS with collimation optics replaced by a light guide. (c) Front-lit LCOS where the PBS is removed. (d) Light propagation process in a front-lit LCOS. (e) New slim LCOS with an enlarged FoV. HG, homogenizer; PL, projection light; LG, light guide; FLP, front-lit plate.

[284] for a direct-view LCD, a back-lit LCOS [285] was proposed to reduce to from factor of the illumination system, as plotted in Fig. 31(b). The whole illumination system could be replaced by a lightguide plate with LEDs on the edge. The lightguide mixes the input light to attain uniform illumination. Still, a PBS cube, which is about 1 cm^3, is required to polarize and direct the illumination toward the LCOS panel, and then analyze the spatially modulated light from the LCOS panel. If the LCOS panel is directly illuminated from top, then the bulky PBS can be replaced by a planar polarizer.

Later, a so-called front-lit LCOS [286,287] was introduced by placing a flat plate in front of LCOS to eliminate both illumination system and PBS, as shown in Fig. 31(c). The idea of "front-lit" could trace back to the reflective LCD direct-view displays [288] in mid-1990s to solve the readability issue in low-light condition. The flat plate is only 1 mm thick in total and the detailed structure of front-lit LCOS is illustrated in Fig. 31(d). The front-lit plate contains a lightguide on top of the LCOS module. The LED is located on the edge of the lightguide, and a polarizer is inserted between the LED and the lightguide. On top of the lightguide, a RP is placed as an analyzer. Assuming the polarizer attached to the LED transmits s-polarized light, the RP should reflect s-wave and let p-wave pass. The s-wave propagates in the lightguide by TIR process or reflecting from optical elements such as dielectric mirrors. When the TIR

condition is not satisfied, the ray escapes from the lightguide and is modulated and reflected by the LCOS panel. The p-wave in the reflected ray passes the RP and forms an image. The downside of this design is that the viewing cone is limited to about 30°. In the original design [286], the LCOS is operating in color-filter mode illuminated by a white LED. If operating in color sequential mode [287], an additional hollow rod is used for RGB color mixing by means of multiple reflections, but the overall thickness of the front-lit plate is still slim (1.5 mm).

Recently, a new LCOS architecture [289,290] specially designed for large-FoV AR applications, radically removes the light guide in the front-lit design, as shown in Fig. 31(e). In this design, the LCOS panel modulates a CP light. The RGB LEDs are placed side-by-side in the light source region. A RP is attached to LEDs for polarization recycling. A linear polarizer (LP) attached with a QWP converts the incident light to LCP state. A lens is placed below QWP and functions as a Fourier transform of the LED light. The LCOS panel at the focal plane of the lens receives the angular spectrum of light from LEDs, where each pixel corresponds to a plane wave component at a different propagation angle. When the light is reflected, the spatial pixel is transformed to far field after passing through the lens for a second time, which is exactly what a waveguide combiner needs. A double circular polarizer, a linear polarizer sandwiched between two crossed QWPs, is inserted between the lens and the LCOS, functioning as a polarizer and analyzer. The orientation of the slow axis of QWP1 and QWP3 should be aligned, whereas that of QWP2 is orthogonal to the other two. In the on state, the LCOS panel modulates the incident light so that the polarization state of the reflected light remains unchanged, which is still LCP and passes through two linear polarizers without any loss ideally. The circular polarization helps suppress stray light caused by Fresnel reflection which will flip the handedness of incident light. For example, the stray light is RCP and will be absorbed by the LP1. Such a compact LCOS design shortens the distance between the collimation lens to the waveguide combiner and therefore enlarges the FoV. With an improved LCOS design, some commercial products with volume close to 1 cm^3 have been launched [280].

An LBS display can be generally divided into two parts including a laser illumination module and a sets of MEMS mirrors. Unlike panel-based display systems, the form factor of a LBS display remains unchanged when increasing the pixel density and FoV [277], because there is no real object plane and pixel information is encoded in the angular domain. Conventionally, in the laser module, the separated RGB laser beams are collimated and then combined before sending it to the scanning MEMS mirror.

Figure 32

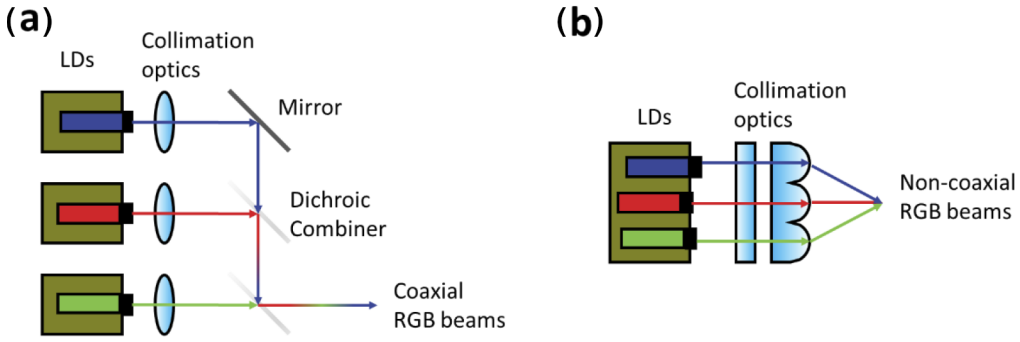

(a) Laser module with separate hermetically sealed RGB laser diodes, separate collimation lens, and a dichroic beam combiner. (b) RGB laser diodes are integrated in one package and share collimation optics without a beam combiner.

Table 1. Comparison of Different Light Engines for AR/VR

VR Light Engine	Resolution Density	Frame Rate	Efficiency	Contrast Ratio	Form Factor[a]
LCD	Low Max: ~2000 PPI (with subpixel rendering)	Medium (90–120 Hz; limited by LC response time and driving scan time)	Low (can be tripled by field sequential colors)	Low ~500:1 (can be enhanced by local dimming)	Medium
μOLED* display	Medium WOLED: ~3000 PPI RGB OLED: ~2645 PPI	Medium (limited by scan and compensation time)	Medium (can be improved by tandem structure)	High ($>10^4$:1)	Small (self-emissive)
AR Light Engine	**Resolution Density**	**Frame Rate**	**Efficiency**	**Contrast Ratio**	**Form Factor***
LCOS display	High 8500 PPI (~3 μm)	Medium (≥720 Hz)	Medium (can be improved by laser backlight)	Medium (~500:1)	Small (new designs without PBS)
DLP display	Medium Texas instruments: 4700 PPI (5.4 μm)	High (improved by hybrid modulation)	Medium (without polarization loss)	Medium (a few thousand to one)	Medium (TIR prism)
μLED display	Medium PlayNitride: 4536 PPI (color conversion) JBD: ~10,000 PPI (single color)	Medium (similar to μOLED display)	Medium (red is worse: EQE ~1%)	High ($>10^4$:1)	Small (self-emissive, single panel)
LBS display	Low (HoloLens 2; worse image quality)	Low (trade-off with resolution density)	High (simple optical structure: only mirror loss)	High ($>10^4$:1)	Small (independent of FoV and pixel density)

[a]μOLED can be used on both AR and VR displays.

Combiners can be a simple X-cube, or a series of mirrors or prisms with dichroic coatings allowing wavelength-selective reflection and transmission of collimated RGB laser beams, as shown in Fig. 32(a). A combiner system occupies the valuable space in light engine and requires precise assembly and alignment processes. A new design [96] is proposed to eliminate any additional combining optical elements by correcting the angular offset of RGB laser beams with software compensation in the time domain, as shown in Fig. 32(b). Two common lenses are used for collimating the RGB laser beams, and the non-coaxial beams intersect at the MEMS mirror plane with a tilt angle. The three laser diodes are shifted accordingly in the propagation direction to compensate for the wavelength-dependent back focal length of lenses. A widely used MEMS mirror configuration is to cascade two 1D MEMS mirrors adopting raster scanning method. The first MEMS mirror has a small diameter and is driven in resonance frequency for horizontal scan. The 1D picture is then sent to a much larger second MEMS mirror for linear scan in the vertical axis. The advantages of this design are the wider angular swing space and faster scan speed. However, the drawback is a larger form factor because two MEMS mirrors need to be aligned and the driving electronics are more complex. The size of the LBS light engine can be dramatically reduced by using a single 2D MEMS mirror, which can scan in both axes, as shown in Fig. 8(d). The trade-offs are the possible cross talk between two axes and the lower frame rate. A LBS with volume less than 1 cm^3 has been demonstrated [281].

6. DISCUSSION AND CONCLUSION

In this paper, we have first reviewed the optical configuration of AR/VR displays, and the requirements of our HVS. Then, we described the operation principle and highlight

the pros and cons of six advanced light engines by five human-centric display metrics. Here, we briefly summarize the pros and cons of each light engine, as listed in Table 1. These analyses on the pros and cons of each light engine can serve as a basis for further developing new light engines to enhance the optical performance of AR/VR displays.

(1) Transmissive LCDs: The aperture ratio, which is governed by the TFT size and black matrices, determines the maximum resolution density of the active-matrix LCD panel for VR headsets. In 2022, a 2016 PPI transmissive LCD prototype has been demonstrated by Innolux. To further increase the resolution density, single-crystal silicon transistors can be utilized, but the FFE needs to be considered as well. Furthermore, the LC response time is about 3 ms, and its optical efficiency is lower than that of LCOS microdisplays due to its larger cell gap and smaller aperture ratio. However, its relatively mature and cheap manufacturing still offers a great advantage for VR applications.
(2) LCOS microdisplay: Its pixel pitch can be as small as 3 μm. Its fast response time enables field sequential color operation, so that the pixel pitch remains at 3 μm for a full-color pixel. It is a mature high-resolution density microdisplay. However, the demand for higher resolution density (<1 μm) for phase modulation applications and for reducing panel size has not stopped. To achieve these goals, the bottleneck of severe FFE needs to be overcome. In addition, a novel front-lit illumination system and PCS have been developed to realize efficient and compact LCOS microdisplays.
(3) DLP microdisplay: It exhibits the highest frame rate among all microdisplay technologies considered because of its fast electromechanical response of the micromirrors, thus supporting multiplane displays. By applying HLM methods and prism designs, a single DMD can simultaneously achieve high contrast ratio and high bit depth. However, the optics of DLP is still bulky and difficult to further improve. It shows the worst compactness of all the six microdisplay technologies discussed here.
(4) OLED microdisplays: High current efficiency is critical for OLED devices to achieve a high brightness with a reasonable lifetime. Tandem WOLED devices and patterned RGB OLED devices have been developed to achieve this goal. The RGB OLEDs without color filters shows high optical efficiency and better color performance. To achieving high-resolution-density RGB OLED devices, the development of organic material patterning methods has recently flourished. Tandem WOLED devices generate additional carrier pairs for higher current efficiency, but the downside is its higher driving voltage. Advanced research has focused on reducing the driving voltage, balancing the carrier recombination for white light emission, and optimizing the cavity design to improve the optical efficiency of tandem WOLED devices. In addition, the frame rate of OLED microdisplays is mainly determined by the compensation method of the driving circuit and similar restrictions also apply to μLED microdisplays.
(5) μLED microdisplays: Although color-conversion μLEDs, vertically stacked μLEDs, and multi-color MQW μLEDs have been proposed and demonstrated as prototypes, there is still no mature fabrication process for full-color high-resolution-density microdisplays. Combining three separate RGB μLED displays with an X-prism is promising, but its volume increases noticeably. In addition, advanced LED chip designs have been developed to mitigate the size effects and narrow the emission cones, thereby increasing the optical efficiency for projection displays. Unlike traditional LEDs, where green color is the least efficient, the least efficient μLEDs are red.

(6) LBS microdisplay: There is a trade-off between resolution density and frame rate. Therefore, to maintain a decent resolution density, the frame rate is limited to about 60 Hz. However, LBS microdisplays offer the advantage of providing high optical coupling in projection systems and are more suitable for some AR display systems such as Maxwellian displays.

FUNDING

Nichia Corporation; Meta.

ACKNOWLEDGMENT

The authors are indebted to Dr. Ming-Yang Deng for useful discussions.

DISCLOSURES

The authors declare no conflicts of interest.

DATA AVAILABILITY

All data needed to evaluate the conclusions in the paper are present in the paper. Additional data related to this paper may be requested from the authors.

REFERENCES

1. M. Schadt, "Milestone in the history of field-effect liquid crystal displays and materials," Jpn. J. Appl. Phys. **48**, 03B001 (2009).
2. C. W. Tang and S. A. VanSlyke, "Organic electroluminescent diodes," Appl. Phys. Lett. **51**, 913–915 (1987).
3. J. Y. Lin and H. X. Jiang, "Development of microLED," Appl. Phys. Lett. **116**, 100502 (2020).
4. E. L. Hsiang, Z. Yang, Q. Yang, Y. F. Lan, and S. T. Wu, "Prospects and challenges of mini-LED, OLED, and micro-LED displays," J. Soc. Inf. Disp. **29**, 446–465 (2021).
5. Y. Huang, E. L. Hsiang, M. Y. Deng, and S. T. Wu, "Mini-LED, Micro-LED and OLED displays: present status and future perspectives," Light: Sci. Appl. **9**, 105 (2020).
6. H. W. Chen, J. H. Lee, B. Y. Lin, S. Chen, and S. T. Wu, "Liquid crystal display and organic light-emitting diode display: present status and future perspectives," Light: Sci. Appl. **7**, 17168 (2018).
7. O. Cakmakci and J. Rolland, "Head-worn displays: a review," J. Disp. Technol. **2**, 199–216 (2006).
8. S. Choi, K. Jung, and S. D. Noh, "Virtual reality applications in manufacturing industries: past research, present findings, and future directions," Concurr. Eng. **23**, 40–63 (2015).
9. X. Li, W. Yi, H. L. Chi, X. Wang, and A. P. C. Chan, "A critical review of virtual and augmented reality (VR/AR) applications in construction safety," Autom. Constr. **86**, 150–162 (2018).
10. K. Yin, E. L. Hsiang, J. Zou, Y. Li, Z. Yang, Q. Yang, P. C. Lai, C. L. Lin, and S. T. Wu, "Advanced liquid crystal devices for augmented reality and virtual reality displays: principles and applications," Light: Sci. Appl. **11**, 161 (2022).
11. J. Xiong, E. L. Hsiang, Z. He, T. Zhan, and S. T. Wu, "Augmented reality and virtual reality displays: emerging technologies and future perspectives," Light: Sci. Appl. **10**, 216 (2021).

12. D. Cheng, Q. Wang, Y. Liu, H. Chen, D. Ni, X. Wang, C. Yao, Q. Hou, W. Hou, G. Luo, and Y. Wang, "Design and manufacture AR head-mounted displays: a review and outlook," Light: Adv. Manuf. **2**, 336–369 (2021).
13. B. C. Kress, *Optical Architectures for Augmented-, Virtual-, and Mixed-Reality Headsets* (SPIE, 2020).
14. C. Chang, K. Bang, G. Wetzstein, B. Lee, and L. Gao, "Toward the next-generation VR/AR optics: a review of holographic near-eye displays from a human-centric perspective," Optica **7**, 1563–1578 (2020).
15. Q. Yang, Z. Yang, Y. F. Lan, and S. T. Wu, "Low-diffraction transparent micro light-emitting diode displays with optimized pixel structure," J. Soc. Inf. Disp. **30**, 395–403 (2022).
16. H. Kim, Y. T. Kwon, H. R. Lim, J. H. Kim, Y. S. Kim, and W. H. Yeo, "Recent advances in wearable sensors and integrated functional devices for virtual and augmented reality applications," Adv. Funct. Mater. **31**, 2005692 (2021).
17. H. G. Kim, H. T. Lim, and Y. M. Ro, "Deep virtual reality image quality assessment with human perception guider for omnidirectional image," IEEE Trans. Circuits Syst. Video Technol. **30**, 917–928 (2020).
18. M. R. Miller, H. Jun, F. Herrera, J. Y. Villa, G. Welch, and J. N. Bailenson, "Social interaction in augmented reality," PLoS One **14**, e0216290 (2019).
19. D. Shin, "How does immersion work in augmented reality games? a user-centric view of immersion and engagement," Inf. Commun. Soc **22**, 1212–1229 (2019).
20. R. T. Azuma, "Making augmented reality a reality," in *Imaging and Applied Optics 2017 (3D, AIO, COSI, IS, MATH, PcAOP)*, OSA Technical Digest (Online) (Optica Publishing Group, 2017), p. JTu1F.1.
21. J. Kim, Y. Jeong, M. Stengel, K. Akşit, R. Albert, B. Boudaoud, T. Greer, J. Kim, W. Lopes, Z. Majercik, P. Shirley, J. Spjut, M. McGuire, and D. Luebke, "Foveated AR: dynamically-foveated augmented reality display," ACM Trans. Graph. **38**, 1 (2019).
22. T. Hirzle, M. Cordts, E. Rukzio, J. Gugenheimer, and A. Bulling, "A critical assessment of the use of ssq as a measure of general discomfort in vr head-mounted displays," in *Proceedings of the 2021 CHI Conference on Human Factors in Computing Systems*, CHI '21 (Association for Computing Machinery, 2021), pp. 530:1–530:14.
23. N. A. Dodgson, "Variation and extrema of human interpupillary distance," Proc. SPIE **5291**, 36–46 (2004).
24. J. Schwiegerling, *Field Guide to Visual and Ophthalmic Optics* (SPIE, 2004).
25. J. W. Goodman, *Introduction to Fourier Optics*, 3rd ed. (Roberts and Company Publishers, 2004).
26. J. min Cho, Y. do Kim, S. H. Jung, H. Shin, and T. Kim, "78-4: screen door effect mitigation and its quantitative evaluation in VR display," Dig. Tech. Pap. - Soc. Inf. Disp. Int. Symp. **48**, 1154–1156 (2017).
27. S. Reichelt, R. Häussler, G. Fütterer, and N. Leister, "Depth cues in human visual perception and their realization in 3D displays," Proc. SPIE **7690**, 76900B (2010).
28. H. Hua, "Enabling focus cues in head-mounted displays," Proc. IEEE **105**, 805–824 (2017).
29. K. J. MacKenzie, D. M. Hoffman, and S. J. Watt, "Accommodation to multiple-focal-plane displays: implications for improving stereoscopic displays and for accommodation control," J. Vis. **10**(8), 22 (2010).
30. R. Zabels, K. Osmanis, M. Narels, U. Gertners, A. Ozols, K. Rūtenbergs, and I. Osmanis, "AR displays: next-generation technologies to solve the vergence–accommodation conflict," Appl. Sci. **9**, 3147 (2019).

31. D. M. Hoffman, A. R. Girshick, K. Akeley, and M. S. Banks, "Vergence–accommodation conflicts hinder visual performance and cause visual fatigue," J. Vis. **8**(3), 33 (2008).
32. G. Kramida, "Resolving the vergence-accommodation conflict in head-mounted displays," IEEE Trans. Vis. Comput. Graphics **22**, 1912–1931 (2016).
33. H. Huang and H. Hua, "High-performance integral-imaging-based light field augmented reality display using freeform optics," Opt. Express **26**, 17578–17590 (2018).
34. X. Wang and H. Hua, "Depth-enhanced head-mounted light field displays based on integral imaging," Opt. Lett. **46**, 985–988 (2021).
35. A. Maimone, A. Georgiou, and J. S. Kollin, "Holographic near-eye displays for virtual and augmented reality," ACM Trans. Graph. **36**, 1–16 (2017).
36. S. B. Kim and J. H. Park, "Optical see-through Maxwellian near-to-eye display with an enlarged eyebox," Opt. Lett. **43**, 767–770 (2018).
37. T. Zhan, J. Xiong, J. Zou, and S. T. Wu, "Multifocal displays: review and prospect," Photonis X **1**, 10 (2020).
38. J. Miseli, "7.3: motion artifacts," Dig. Tech. Pap. - Soc. Inf. Disp. Int. Symp. **35**, 86–89 (2004).
39. B. Shneiderman, "Response time and display rate in human performance with computers," ACM Comput. Surv. **16**, 265–285 (1984).
40. H. Pan, X. F. Feng, and S. Daly, "LCD motion blur modeling and analysis," in *IEEE International Conference on Image Processing 2005* (2005).
41. J. Zhao, R. S. Allison, M. Vinnikov, and S. Jennings, "Estimating the motion-to-photon latency in head mounted displays," in *2017 IEEE Virtual Reality (VR)* (2017), pp. 313–314.
42. P. Lincoln, A. Blate, M. Singh, T. Whitted, A. State, A. Lastra, and H. Fuchs, "From motion to photons in 80 microseconds: towards minimal latency for virtual and augmented reality," IEEE Trans. Vis. Comput. Graphics **22**, 1367–1376 (2016).
43. H. Seetzen, W. Heidrich, W. Stuerzlinger, G. Ward, L. Whitehead, M. Trentacoste, A. Ghosh, and A. Vorozcovs, "High dynamic range display systems," ACM Trans. Graph. **23**, 760–768 (2004).
44. P. Lincoln, A. Blate, M. Singh, A. State, M. C. Whitton, T. Whitted, and H. Fuchs, "Scene-adaptive high dynamic range display for low latency augmented reality," in *Proceedings of the 21st ACM SIGGRAPH Symposium on Interactive 3D Graphics and Games, I3D '17* (Association for Computing Machinery, 2017), pp. 15:1–15:7.
45. Y. H. Lee, T. Zhan, and S. T. Wu, "Prospects and challenges in augmented reality displays," Virtual Real. Intell. Hardw. **1**, 10–20 (2019).
46. S. A. Cholewiak, Z. Başgöze, O. Cakmakci, D. M. Hoffman, and E. A. Cooper, "A perceptual eyebox for near-eye displays," Opt. Express **28**, 38008–38028 (2020).
47. E. Hecht, *Optics* (Pearson, 2017).
48. T. Lin, T. Lin, T. Lin, T. Zhan, T. Zhan, J. Zou, F. Fan, and S. T. Wu, "Maxwellian near-eye display with an expanded eyebox," Opt. Express **28**, 38616–38625 (2020).
49. J. Xiong, Y. Li, K. Li, and S. T. Wu, "Aberration-free pupil steerable Maxwellian display for augmented reality with cholesteric liquid crystal holographic lenses," Opt. Lett. **46**, 1760–1763 (2021).
50. T. Zhan, J. Zou, J. Xiong, X. Liu, H. Chen, J. Yang, S. Liu, Y. Dong, and S. T. Wu, "Practical chromatic aberration correction in virtual reality displays enabled by cost-effective ultra-broadband liquid crystal polymer lenses," Adv. Opt. Mater. **8**, 1901360 (2020).

51. B. A. Narasimhan, "Ultra-compact pancake optics based on ThinEyes super-resolution technology for virtual reality headsets," Proc. SPIE **10676**, 106761G (2018).
52. A. Maimone and J. Wang, "Holographic optics for thin and lightweight virtual reality," ACM Trans. Graph. **39**, 67 (2020).
53. Y. Li, T. Zhan, Z. Yang, C. Xu, P. L. LiKamWa, K. Li, and S. T. Wu, "Broadband cholesteric liquid crystal lens for chromatic aberration correction in catadioptric virtual reality optics," Opt. Express **29**, 6011–6020 (2021).
54. K. Pulli, "11-2: invited paper: Meta 2: immersive optical-see-through augmented reality," Dig. Tech. Pap. - Soc. Inf. Disp. Int. Symp. **48**, 132–133 (2017).
55. B. Lee, C. Yoo, J. Jeong, B. Lee, and K. Bang, "Key issues and technologies for AR/VR head-mounted displays," Proc. SPIE **11304**, 1130402 (2020).
56. G. Westheimer, "The Maxwellian view," Vision Res. **6**, 669–682 (1966).
57. C. Jang, K. Bang, S. Moon, J. Kim, S. Lee, and B. Lee, "Retinal 3D: augmented reality near-eye display via pupil-tracked light field projection on retina," ACM Trans. Graph. **36**, 1–13 (2017).
58. D. Cheng, Y. Wang, H. Hua, and M. M. Talha, "Design of an optical see-through head-mounted display with a low f-number and large field of view using a freeform prism," Appl. Opt. **48**, 2655–2668 (2009).
59. D. K. Yang and S. T. Wu, *Fundamentals of Liquid Crystal Devices* (John Wiley & Sons, 2006).
60. S. H. Lee, S. L. Lee, and H. Y. Kim, "Electro-optic characteristics and switching principle of a nematic liquid crystal cell controlled by fringe-field switching," Appl. Phys. Lett. **73**, 2881–2883 (1998).
61. M. F. Schiekel and K. Fahrenschon, "Deformation of nematic liquid crystals with vertical orientation in electrical fields," Appl. Phys. Lett. **19**, 391–393 (1971).
62. D. H. Kim, Y. J. Lim, D. E. Kim, H. Ren, S. H. Ahn, and S. H. Lee, "Past, present, and future of fringe-field switching-liquid crystal display," J. Inf. Disp. **15**, 99–106 (2014).
63. J. J. Lyu, J. Sohn, H. Y. Kim, and S. H. Lee, "Recent trends on patterned vertical alignment (PVA) and fringe-field switching (FFS) liquid crystal displays for liquid crystal television applications," J. Disp. Technol. **3**, 404–412 (2007).
64. S. S. Kim, B. H. You, J. H. Cho, D. G. Kim, B. H. Berkeley, and N. D. Kim, "An 82-in. ultra-definition 120-Hz LCD TV using new driving scheme and advanced super PVA technology," J. Soc. Inf. Disp. **17**, 71–78 (2009).
65. M. N. Ernstoff, A. M. Leupp, M. J. Little, and H. T. Peterson, "Liquid crystal pictorial display," in *1973 International Electron Devices Meeting* (IEEE, 1973), pp. 548–551.
66. N. Collings, W. A. Crossland, P. J. Ayliffe, D. G. Vass, and I. Underwood, "Evolutionary development of advanced liquid crystal spatial light modulators," Appl. Opt. **28**, 4740–4747 (1989).
67. S. T. Wu and C. S. Wu, "Mixed-mode twisted nematic liquid crystal cells for reflective displays," Appl. Phys. Lett. **68**, 1455–1457 (1996).
68. D. Dudley, W. M. Duncan, and J. Slaughter, "Emerging digital micromirror device (DMD) applications," Proc. SPIE **4985**, 14–25 (2003).
69. L. J. Hornbeck, "Digital light processing for high-brightness high-resolution applications," Proc. SPIE **3013**, 27–40 (1997).
70. Texas Instrument, "Introduction to ±12 degree orthogonal digital micromirror devices (DMDs)," https://www.ti.com/lit/pdf/dlpa008b.
71. S. Scholes, R. Kara, J. Pinnell, V. Rodríguez-Fajardo, and A. Forbes, "Structured light with digital micromirror devices: a guide to best practice," Opt. Eng. **59**, 1 (2019).
72. Texas Instruments, "DLP system optics," https://www.ti.com/lit/pdf/dlpa022.

73. D. Y. Kondakov, "Characterization of triplet-triplet annihilation in organic light-emitting diodes based on anthracene derivatives," J. Appl. Phys. **102**, 114504 (2007).
74. M. A. Baldo, S. Lamansky, P. E. Burrows, M. E. Thompson, and S. R. Forrest, "Very high-efficiency green organic light-emitting devices based on electrophosphorescence," Appl. Phys. Lett. **75**, 4–6 (1999).
75. H. Uoyama, K. Goushi, K. Shizu, H. Nomura, and C. Adachi, "Highly efficient organic light-emitting diodes from delayed fluorescence," Nature **492**, 234–238 (2012).
76. Y. S. Park, S. Lee, K. H. Kim, S. Y. Kim, J. H. Lee, and J. J. Kim, "Exciplex-forming co-host for organic light-emitting diodes with ultimate efficiency," Adv. Funct. Mater. **23**, 4914–4920 (2013).
77. A. Salehi, X. Fu, D. H. Shin, and F. So, "Recent advances in OLED optical design," Adv. Funct. Mater. **29**, 1808803 (2019).
78. W. K. Lee, Y. T. Chen, S. W. Wen, P. H. Liao, M. C. Lee, T. S. Hsu, Y. J. Chen, G. D. Su, H. Y. Lin, C. C. Chen, W. Y. Lin, L. Xu, G. Yu, B. L. Kwak, R. J. Visser, and C. C. Wu, "Three-dimensional pixel configurations for optical outcoupling of OLED displays—optical simulation," J. Soc. Inf. Disp. **27**, 273–284 (2019).
79. S. L. Lee, C. C. Cheng, C. J. Liu, C. N. Yeh, and Y. C. Lin, "9.4-inch 228-ppi flexible micro-LED display," J. Soc. Inf. Disp. **29**, 360–369 (2021).
80. J. Bae, Y. Shin, H. Yoo, Y. Choi, J. Lim, D. Jeon, I. Kim, M. Han, and S. Lee, "Quantum dot-integrated GaN light-emitting diodes with resolution beyond the retinal limit," Nat. Commun. **13**, 1862 (2022).
81. K. Parikh, J. Zhuang, K. Pallister, J. Jiang, and M. Smith, "40-1: invited paper: next generation virtual reality displays: challenges and opportunities," Dig. Tech. Pap. - Soc. Inf. Disp. Int. Symp. **49**, 502–505 (2018).
82. K. Kim, C. Kim, J. K. Park, D. H. Kim, and K. Jung, "75-4: invited paper: FMM materials and manufacturing process: review of the technical issues," Dig. Tech. Pap. - Soc. Inf. Disp. Int. Symp. **49**, 1011–1013 (2018).
83. Y. Onoyama, J. Yamashita, H. Kitagawa, E. Hasegawa, A. Makita, S. Yokoyama, R. Asaki, E. Kambe, T. Nishimura, J. Yamada, K. Uchino, S. Makimura, Y. Shiraishi, and T. Urabes, "70.4L: late-news paper: 0.5-inch XGA Micro-OLED display on a silicon backplane with high-definition technologies," Dig. Tech. Pap. - Soc. Inf. Disp. Int. Symp. **43**, 950–953 (2012).
84. J. Hamer, M. Kondakova, J. Spindler, R. Cupello, S. Hamer, M. Andre, S. McClurg, A. Pleten, B. Primerano, D. Scott, G. Scherer, and S. Stickel, "High-performance OLED microdisplays made with multi-stack OLED formulations on CMOS backplanes," Proc. SPIE **11473**, 114730F (2020).
85. J. H. Lee, C. H. Chen, P. H. Lee, H. Y. Lin, M. K. Leung, T. L. Chiu, and C. F. Lin, "Blue organic light-emitting diodes: current status, challenges, and future outlook," J. Mater. Chem. C **7**, 5874–5888 (2019).
86. N. Holonyak and S. F. Bevacqua, "Coherent (visible) light emission from $Ga(As_{1-x}P_x)$ junctions," Appl. Phys. Lett. **1**, 82–83 (1962).
87. Y. Nanishi, "The birth of the blue LED," Nat. Photonics **8**, 884–886 (2014).
88. X. J. Yu, Y. L. Ho, L. Tan, H. C. Huang, and H. S. Kwok, "LED-based projection systems," J. Disp. Technol. **3**, 295–303 (2007).
89. H. X. Jiang, S. X. Jin, J. Li, J. Shakya, and J. Y. Lin, "III-nitride blue microdisplays," Appl. Phys. Lett. **78**, 1303–1305 (2001).
90. A. R. Anwar, M. T. Sajjad, M. A. Johar, C. A. Hernández-Gutiérrez, M. Usman, and S. P. Łepkowski, "Recent progress in micro-LED-based display technologies," Laser Photonics Rev. **16**, 2100427 (2022).
91. K. L. Liang, W. H. Kuo, H. T. Shen, P. W. Yu, Y. H. Fang, and C. C. Lin, "Advances in color-converted micro-LED arrays," Jpn. J. Appl. Phys. **60**, SA0802 (2021).

92. Z. J. Liu, W. C. Chong, K. M. Wong, K. H. Tam, and K. M. Lau, "A novel BLU-free full-color LED projector using LED on silicon micro-displays," IEEE Photonics Technol. Lett. **25**, 2267–2270 (2013).
93. G. R. B. E. Römer and P. Bechtold, "Electro-optic and acousto-optic laser beam scanners," Phys. Procedia **56**, 29–39 (2014).
94. G. Silva, F. Carpignano, F. Guerinoni, S. Costantini, M. De Fazio, and S. Merlo, "Optical detection of the electromechanical response of MEMS micromirrors designed for scanning picoprojectors," IEEE J. Sel. Top. Quantum Electron. **21**, 147–156 (2015).
95. J. Ma, "Advanced MEMS-based technologies and displays," Displays **37**, 2–10 (2015).
96. J. Reitterer, Z. Chen, A. Balbekova, G. Schmid, G. Schestak, F. Nassar, M. Dorfmeister, and M. Ley, "Ultra-compact micro-electro-mechanical laser beam scanner for augmented reality applications," Proc. SPIE **11765**, 1176504 (2021).
97. C. L. Yang, Y. H. Wu, I. A. Yao, Y. S. Tsou, C. H. Tsai, and J. S. Lin, "47-1: invited paper: high resolution HDR VR display using Mini-LED," Dig. Tech. Pap. - Soc. Inf. Disp. Int. Symp. **52**, 636–639 (2021).
98. M. S. Park, H. J. Youn, C. S. Lee, and S. H. Yoon, "P-156: flicker effect depending on the density of charge impurities in the cell," Dig. Tech. Pap. - Soc. Inf. Disp. Int. Symp. **49**, 1744–1747 (2018).
99. T. Nakamura, M. Tada, and H. Kimura, "A 550-PPI LCD using 1.5 μm channel width LTPS TFTs with low frame rate driving," J. Soc. Inf. Disp. **23**, 580–586 (2015).
100. P. Huo, L. Yao, B. Li, Y. Fang, Z. Wang, J. Xu, and J. Xie, "P-3.3: analysis and improvement of flicker NG on VR display," Dig. Tech. Pap. - Soc. Inf. Disp. Int. Symp. **52**, 721–723 (2021).
101. K. Yoshida, S. Ueda, A. Hachiya, K. Okada, A. Hirai, Y. Kawahira, K. Misaki, H. Furukawa, and H. Katoh, "Thin and low-reflection metal black matrix for high PPI liquid crystal display," J. Soc. Inf. Disp. **30**, 413–422 (2022).
102. L. Yao, F. Li, Y. Fang, W. Li, H. Su, L. Yan, Y. Gao, K. Li, C. Wang, L. Hou, and J. Xie, "P-3.7: study on preparation and performance of new black matrix with high PPI VR display," Dig. Tech. Pap. - Soc. Inf. Disp. Int. Symp. **52**, 735–737 (2021).
103. Y. Ma, H. Ikeno, P. Shen, L. Wu, H. Wu, Q. Song, and C. Tseng, "37-3: a novel pixel structure for 847 PPI display with LTPS technology," Dig. Tech. Pap. - Soc. Inf. Disp. Int. Symp. **47**, 477–479 (2016).
104. J. H. Kwon, S. H. Ji, S. H. Han, M. S. Kwak, M. Jun, and I. B. Kang, "P-184: improvement of color mixing in high PPI mobile displays," Dig. Tech. Pap. - Soc. Inf. Disp. Int. Symp. **47**, 1830–1833 (2016).
105. C. Kim, K. Kim, O. Kwon, J. Jung, J. K. Park, D. H. Kim, and K. Jung, "Fine metal mask material and manufacturing process for high-resolution active-matrix organic light-emitting diode displays," J. Soc. Inf. Disp. **28**, 668–679 (2020).
106. C. Kim, J. H. Jung, D. Y. Sung, J. S. Park, J. K. Park, T. Kim, D. H. Kim, and K. Jung, "11-3: 2,400ppi RGB side-by-side OLED micro-display for AR applications," Dig. Tech. Pap. - Soc. Inf. Disp. Int. Symp. **52**, 131–134 (2021).
107. Y. Jiang, B. S. T. Tam, S. C. Dong, and C. W. Tang, "61-2: 2-inch, 2,000-PPI silicon nitride mask for patterning ultra-high-resolution OLED displays," Dig. Tech. Pap. - Soc. Inf. Disp. Int. Symp. **51**, 909–912 (2020).
108. C. Hwang, S. S. Kim, S. W. Bang, S. H. Choi, B. D. Chin, and H. Ko, "67-3: unique belt plane source evaporation techniques for the mass production of 2250ppi AMOLED and 77" QD OLED TV," Dig. Tech. Pap. - Soc. Inf. Disp. Int. Symp. **50**, 949–952 (2019).

109. P. E. Malinowski, T. H. Ke, A. Nakamura, Y. H. Liu, D. Vander Velpen, E. Vandenplas, N. Papadopoulos, A. J. Kronemeijer, J. L. van der Steen, S. Steudel, C. C. Kuo, Y. Y. Huang, Y. H. Chen, M. H. Yeh, G. Gelinck, and P. Heremans, "High resolution photolithography for direct view active matrix organic light-emitting diode augmented reality displays," J. Soc. Inf. Disp. **26**, 128–136 (2018).
110. T. H. Ke, A. Glushkova, C. M. Sandeheng, G. M. Alvarez, E. Vandenplas, R. M. Ciarnain, P. E. Malinowski, J. Mitard, N. Rassoul, A. Belmonte, Z. Tokei, G. S. Kar, J. Genoe, and P. Heremans, "11-2: technology developments in high-resolution FMM-free OLED and BEOL IGZO TFTs for power-efficient microdisplays," Dig. Tech. Pap. - Soc. Inf. Disp. Int. Symp. **52**, 127–130 (2021).
111. M. C. Gather, A. Köhnen, A. Falcou, H. Becker, and K. Meerholz, "Solution-processed full-color polymer organic light-emitting diode displays fabricated by direct photolithography," Adv. Funct. Mater. **17**, 191–200 (2007).
112. K. Kim, G. Kim, B. Ram Lee, S. Ji, S. Y. Kim, B. Wan An, M. Hoon Song, and J. U. Park, "High-resolution electrohydrodynamic jet printing of small-molecule organic light-emitting diodes," Nanoscale **7**, 13410–13415 (2015).
113. L. Mu, C. Jiang, J. Wang, H. Zheng, L. Ying, M. Xu, J. Wang, J. Peng, and Y. Cao, "34-3: OLED display with high resolution fabricated by electrohydrodynamic printing," Dig. Tech. Pap. - Soc. Inf. Disp. Int. Symp. **51**, 485–488 (2020).
114. L. Qi, X. Zhang, W. C. Chong, P. Li, and K. M. Lau, "848 ppi high-brightness active-matrix micro-LED micro-display using GaN-on-Si epi-wafers towards mass production," Opt. Express **29**, 10580–10591 (2021).
115. K. A. Bulashevich, S. S. Konoplev, and S. Y. Karpov, "Effect of die shape and size on performance of III-nitride micro-LEDs: a modeling study," Photonics **5**, 41 (2018).
116. L. Zhang, F. Ou, W. C. Chong, Y. Chen, and Q. Li, "Wafer-scale monolithic hybrid integration of Si-based IC and III–V epi-layers—A mass manufacturable approach for active matrix micro-LED micro-displays," J. Soc. Inf. Disp. **26**, 137–145 (2018).
117. H. Kawanishi, H. Onuma, M. Maegawa, T. Kurisu, T. Ono, S. Akase, S. Yamaguchi, N. Momotani, Y. Fujita, Y. Kondo, K. Kubota, T. Yoshida, Y. Ikawa, T. Ono, H. Higashisaka, Y. Hirano, and S. Anzai, "High-resolution and high-brightness full-colour 'silicon display' for augmented and mixed reality," J. Soc. Inf. Disp. **29**, 57–67 (2021).
118. M. A. Triana, E. L. Hsiang, C. Zhang, Y. Dong, and S. T. Wu, "Luminescent nanomaterials for energy-efficient display and healthcare," ACS Energy Lett. **7**, 1001–1020 (2022).
119. Z. Liu, C. H. Lin, B. R. Hyun, C. W. Sher, Z. Lv, B. Luo, F. Jiang, T. Wu, C. H. Ho, H. C. Kuo, and J. H. He, "Micro-light-emitting diodes with quantum dots in display technology," Light: Sci. Appl. **9**, 83 (2020).
120. T. H. Kim, K. S. Cho, E. K. Lee, S. J. Lee, J. Chae, J. W. Kim, D. H. Kim, J. Y. Kwon, G. Amaratunga, S. Y. Lee, B. L. Choi, Y. Kuk, J. M. Kim, and K. Kim, "Full-colour quantum dot displays fabricated by transfer printing," Nat. Photonics **5**, 176–182 (2011).
121. R. Palankar, N. Medvedev, A. Rong, and M. Delcea, "Fabrication of quantum dot microarrays using electron beam lithography for applications in analyte sensing and cellular dynamics," ACS Nano **7**, 4617–4628 (2013).
122. H. L. Kang, J. Kang, J. K. Won, S. M. Jung, J. Kim, C. H. Park, B. K. Ju, M. G. Kim, and S. K. Park, "Spatial light patterning of full color quantum dot displays enabled by locally controlled surface tailoring," Adv. Opt. Mater. **6**, 1701335 (2018).

123. D. M. Geum, S. K. Kim, C. M. Kang, S. H. Moon, J. Kyhm, J. Han, D. S. Lee, and S. Kim, "Strategy toward the fabrication of ultrahigh-resolution micro-LED displays by bonding-interface-engineered vertical stacking and surface passivation," Nanoscale **11**, 23139–23148 (2019).
124. Z. Wang, S. Zhu, X. Shan, Z. Yuan, X. Cui, and P. Tian, "Full-color micro-LED display based on a single chip with two types of InGaN/GaN MQWs," Opt. Lett. **46**, 4358–4361 (2021).
125. L. Li, G. Tang, Z. Shi, H. Ding, C. Liu, D. Cheng, Q. Zhang, L. Yin, Z. Yao, L. Duan, D. Zhang, C. Wang, M. Feng, Q. Sun, Q. Wang, Y. Han, L. Wang, Y. Luo, and X. Sheng, "Transfer-printed, tandem microscale light-emitting diodes for full-color displays," Proc. Natl. Acad. Sci. U. S. A. **118**, e2023436118 (2021).
126. D. J. Kong, C. M. Kang, J. Y. Lee, J. Kim, and D. S. Lee, "Color tunable monolithic InGaN/GaN LED having a multi-junction structure," Opt. Express **24**, A667–A673 (2016).
127. S. H. Mun, C. M. Kang, J. H. Min, S. Y. Choi, W. L. Jeong, G. G. Kim, J. S. Lee, K. P. Kim, H. C. Ko, and D. S. Lee, "Highly efficient full-color inorganic LEDs on a single wafer by using multiple adhesive bonding," Adv. Mater. Interfaces **8**, 2100300 (2021).
128. C. M. Kang, J. Y. Lee, D. J. Kong, J. P. Shim, S. Kim, S. H. Mun, S. Y. Choi, M. D. Park, J. Kim, and D. S. Lee, "Hybrid full-color inorganic light-emitting diodes integrated on a single wafer using selective area growth and adhesive bonding," ACS Photonics **5**, 4413–4422 (2018).
129. K. Yadavalli, C. L. Chuang, and H. S. El-Ghoroury, "Monolithic and heterogeneous integration of RGB micro-LED arrays with pixel-level optics array and CMOS image processor to enable small form-factor display applications," Proc. SPIE **11310**, 113100Z (2020).
130. C. M. Kang, S. J. Kang, S. H. Mun, S. Y. Choi, J. H. Min, S. Kim, J. P. Shim, and D. S. Lee, "Monolithic integration of AlGaInP-based red and InGaN-based green LEDs via adhesive bonding for multicolor emission," Sci. Rep. **7**, 10333 (2017).
131. H. S. El-Ghoroury, M. Yeh, J. C. Chen, X. Li, and C. L. Chuang, "Growth of monolithic full-color GaN-based LED with intermediate carrier blocking layers," AIP Adv. **6**, 075316 (2016).
132. Y. Huang, E. Liao, R. Chen, and S. T. Wu, "Liquid-crystal-on-silicon for augmented reality displays," Appl. Sci. **8**, 2366 (2018).
133. R. Dąbrowski, P. Kula, and J. Herman, "High birefringence liquid crystals," Crystals **3**, 443–482 (2013).
134. S. Gauza, H. Wang, C. H. Wen, S. T. Wu, A. J. Seed, and R. Dabrowski, "High birefringence isothiocyanato tolane liquid crystals," Jpn. J. Appl. Phys. **42**, 3463–3466 (2003).
135. J. Zou, Z. Yang, C. Mao, and S. T. Wu, "Fast-response liquid crystals for 6G optical communications," Crystals **11**, 797 (2021).
136. K. H. Fan-Chiang, S. H. Chen, and S. T. Wu, "High-definition vertically aligned liquid crystal microdisplays using a circularly polarized light," Appl. Phys. Lett. **87**, 031110 (2005).
137. K. H. Fan-Chiang, S. T. Wu, and S. H. Chen, "Fringing field effect of the liquid-crystal-on-silicon devices," Jpn. J. Appl. Phys. **41**, 4577–4585 (2002).
138. Y. W. Li, W. H. Chen, K. H. Fan Chiang, H. C. Kuo, and H. C. Tsai, "18.2: color filter LCOS with double mirror structure," Dig. Tech. Pap. - Soc. Inf. Disp. Int. Symp. **45**, 223–225 (2014).
139. H. Vithana, "Vertically aligned nematic mode liquid crystal display having large tilt angles and high contrast," U.S. patent 9,551,901 (10 September 2017).

140. C. H. Liao, "Reducing fringe field effect for spatial light modulator," U.S. patent 10,416,498 (21 June 2018).
141. L. Yang, J. Xia, and X. Zhang, "Optimization of fringing field effect using dielectric separation and local electric field enhancement," J. Disp. Technol. **11**, 242–247 (2015).
142. Y. Isomae, Y. Shibata, T. Ishinabe, and H. Fujikake, "Design of 1-μm-pitch liquid crystal spatial light modulators having dielectric shield wall structure for holographic display with wide field of view," Opt. Rev. **24**, 165–176 (2017).
143. Y. Isomae, T. Ishinabe, Y. Shibata, and H. Fujikake, "Alignment control of liquid crystals in a 1.0-μm-pitch spatial light modulator by lattice-shaped dielectric wall structure," J. Soc. Inf. Disp. **27**, 251–258 (2019).
144. U. Efron, B. Apter, and E. Bahat-Treidel, "Fringing-field effect in liquid-crystal beam-steering devices: an approximate analytical model," J. Opt. Soc. Am. A **21**, 1996–2008 (2004).
145. S. Moser, M. Ritsch-Marte, and G. Thalhammer, "Model-based compensation of pixel crosstalk in liquid crystal spatial light modulators," Opt. Express **27**, 25046–25063 (2019).
146. M. Persson, D. Engström, and M. Goksör, "Reducing the effect of pixel crosstalk in phase only spatial light modulators," Opt. Express **20**, 22334–22343 (2012).
147. H. M. Chen, J. P. Yang, H. T. Yen, Z. N. Hsu, Y. Huang, and S. T. Wu, "Pursuing high quality phase-only liquid crystal on silicon (LCoS) devices," Appl. Sci. **8**, 2323 (2018).
148. J. Zou, Q. Yang, E. L. Hsiang, H. Ooishi, Z. Yang, K. Yoshidaya, and S. T. Wu, "Fast-response liquid crystal for spatial light modulator and LiDAR applications," Crystals **11**, 93 (2021).
149. S. H. Lee, S. S. Bhattacharyya, H. S. Jin, and K. U. Jeong, "Devices and materials for high-performance mobile liquid crystal displays," J. Mater. Chem. **22**, 11893–11903 (2012).
150. J. Li, Z. Peng, R. Chen, J. Li, M. Hu, L. Zhang, and Z. An, "Investigation of terminal olefine in the isothiocyanatotolane liquid crystals with alkoxy end group," Liq. Cryst. **45**, 1498–1507 (2018).
151. S. T. S. Holmstrom, U. Baran, and H. Urey, "MEMS laser scanners: a review," J. Microelectromech. Syst. **23**, 259–275 (2014).
152. H. Urey, D. W. Wine, and J. R. Lewis, "Scanner design and resolution trade-offs for miniature scanning displays," Proc. SPIE **3636**, 60–68 (1999).
153. P. J. Brosens, "Dynamic mirror distortions in optical scanning," Appl. Opt. **11**, 2987–2989 (1972).
154. S. T. Wu, "Nematic liquid crystal modulator with response time less than 100 μs at room temperature," Appl. Phys. Lett. **57**, 986–988 (1990).
155. F. Peng, H. Chen, F. Gou, Y. H. Lee, M. Wand, M. C. Li, S. L. Lee, and S. T. Wu, "Analytical equation for the motion picture response time of display devices," J. Appl. Phys. **121**, 023108 (2017).
156. S. I. Jo, S. S. Yoon, S. R. Park, J. H. Lee, M. C. Jun, and I. B. Kang, "44-2: invited paper: fast response time advanced high performance in-plane switching (AH-IPS) mode for high resolution application," Dig. Tech. Pap. - Soc. Inf. Disp. Int. Symp. **49**, 581–584 (2018).
157. F. Gou, H. Chen, M. C. Li, S. L. Lee, and S. T. Wu, "Submillisecond-response liquid crystal for high-resolution virtual reality displays," Opt. Express **25**, 7984–7997 (2017).
158. W. K. Choi, C. W. Hsu, C. H. Tung, and B. K. Tseng, "Effects of electrode structure and dielectric anisotropy on the performance of VA-FFS LC mode," Opt. Express **27**, 34343–34358 (2019).

159. T. H. Choi, S. W. Oh, Y. J. Park, Y. Choi, and T. H. Yoon, "Fast fringe-field switching of a liquid crystal cell by two-dimensional confinement with virtual walls," Sci. Rep. **6**, 27936 (2016).
160. T. Matsushima, S. Kimura, and S. Komura, "Fast response in-plane switching liquid crystal display mode optimized for high-resolution virtual-reality head-mounted display," J. Soc. Inf. Disp. **29**, 221–229 (2021).
161. J. H. Yoon, S. J. Lee, Y. J. Lim, E. J. Seo, H. S. Shin, J. M. Myoung, and S. H. Lee, "Fast switching, high contrast and high resolution liquid crystal device for virtual reality display," Opt. Express **26**, 34142–34149 (2018).
162. M. Engel, G. Bernatz, A. Götz, H. Hirschmann, and S. K. Lee, "43.1: invited paper: UB-FFS: new materials for advanced mobile applications," Dig. Tech. Pap. - Soc. Inf. Disp. Int. Symp. **46**, 645–647 (2015).
163. H. Chen, M. Hu, F. Peng, J. Li, Z. An, and S. T. Wu, "Ultra-low viscosity liquid crystal materials," Opt. Mater. Express **5**, 655–660 (2015).
164. Y. Chen, F. Peng, and S. T. Wu, "Submillisecond-response vertical-aligned liquid crystal for color sequential projection displays," J. Disp. Technol. **9**, 78–81 (2013).
165. F. Peng, F. Gou, H. Chen, Y. Huang, and S. T. Wu, "A submillisecond-response liquid crystal for color sequential projection displays," J. Soc. Inf. Disp. **24**, 241–245 (2016).
166. A. K. Abeeluck, A. Iverson, H. Goetz, and E. Passon, "58-2: *Invited Paper:* high-performance displays for wearable and HUD applications," Dig. Tech. Pap. - Soc. Inf. Disp. Int. Symp. **49**, 768–771 (2018).
167. S. T. Wu, "Design of a liquid crystal based tunable electrooptic filter," Appl. Opt. **28**, 48–52 (1989).
168. Y. Li, Z. Yang, R. Chen, L. Mo, J. Li, M. Hu, and S. T. Wu, "Submillisecond-response polymer network liquid crystal phase modulators," Polymers **12**, 2862 (2020).
169. Q. Yang, J. Zou, Y. Li, and S. T. Wu, "Fast-response liquid crystal phase modulators with an excellent photostability," Crystals **10**, 765 (2020).
170. Z. Zhang, Z. You, and D. Chu, "Fundamentals of phase-only liquid crystal on silicon (LCOS) devices," Light: Sci. Appl. **3**, e213 (2014).
171. Q. Guo, K. Yan, V. Chigrinov, H. Zhao, and M. Tribelsky, "Ferroelectric liquid crystals: physics and applications," Crystals **9**, 470 (2019).
172. V. Chigrinov, Q. Guo, and A. Kudreyko, "Photo-aligned ferroelectric liquid crystal devices with novel electro-optic characteristics," Crystals **10**, 563 (2020).
173. T. Haist and W. Osten, "Holography using pixelated spatial light modulators—part 1: theory and basic considerations," J. Micro/Nanolith. MEMS MOEMS **14**, 041310 (2015).
174. J. H. R. Chang, B. V. K. Vijaya Kumar, and A. C. Sankaranarayanan, "2^{16} shades of gray: high bit-depth projection using light intensity control," Opt. Express **24**, 27937–27950 (2016).
175. K. Rathinavel, H. Wang, A. Blate, and H. Fuchs, "An extended depth-at-field volumetric near-eye augmented reality display," IEEE Trans. Visual. Comput. Graphics **24**, 2857–2866 (2018).
176. S. Lee, Y. Jo, D. Yoo, J. Cho, D. Lee, and B. Lee, "Tomographic near-eye displays," Nat. Commun. **10**, 2497 (2019).
177. H. Urey, D. W. Wine, and T. D. Osborn, "Optical performance requirements for MEMS-scanner-based microdisplays," Proc. SPIE **4178**, 176–185 (2000).
178. C. L. Lin, C. C. Hung, P. Y. Kuo, and M. H. Cheng, "New LTPS pixel circuit with AC driving method to reduce OLED degradation for 3D AMOLED displays," J. Disp. Technol. **8**, 681–683 (2012).

179. H. J. In and O. K. Kwon, "A simple pixel structure using polycrystalline-silicon thin-film transistors for high-resolution active-matrix organic light-emitting diode displays," IEEE Electron Device Lett. **33**, 1018–1020 (2012).
180. C. L. Lin, F. H. Chen, C. C. Hung, P. S. Chen, M. Y. Deng, C. M. Lu, and T. H. Huang, "New a-IGZO pixel circuit composed of three transistors and one capacitor for use in high-speed-scan AMOLED displays," J. Disp. Technol. **11**, 1031–1034 (2015).
181. N. H. Keum, K. Oh, S. K. Hong, and O. K. Kwon, "A pixel structure using block emission driving method for high image quality in active matrix organic light-emitting diode displays," J. Disp. Technol. **12**, 1250–1256 (2016).
182. C. L. Lin, C. C. Hung, W. Y. Chang, K. W. Chou, and C. Y. Chuang, "Novel a-Si:H AMOLED pixel circuit to ameliorate OLED luminance degradation by external detection," IEEE Electron Device Lett. **32**, 1716–1718 (2011).
183. S. Sambandan and A. Nathan, "Single-technology-based statistical calibration for high-performance active-matrix organic LED displays," J. Disp. Technol. **3**, 284–294 (2007).
184. C. L. Lin, P. C. Lai, L. W. Shih, C. C. Hung, P. C. Lai, T. Y. Lin, K. H. Liu, and T. H. Wang, "Compensation pixel circuit to improve image quality for mobile AMOLED displays," IEEE J. Solid-State Circuits **54**, 489–500 (2019).
185. F. Fournier and J. Rolland, "Design methodology for high brightness projectors," J. Disp. Technol. **4**, 86–91 (2008).
186. E. L. Hsiang, Z. Yang, T. Zhan, J. Zou, H. Akimoto, and S. T. Wu, "Optimizing the display performance for virtual reality systems," OSA Continuum **4**, 3052–3067 (2021).
187. L. Noui, J. Reitterer, and M. Schöffmann, "Laser beam scanner and combiner architectures," Proc. SPIE **11765**, 1176508 (2021).
188. M. Sugawara, M. Suzuki, and N. Miyauchi, "14-5L: late-news paper: retinal imaging laser eyewear with focus-free and augmented reality," Dig. Tech. Pap. - Soc. Inf. Disp. Int. Symp. **47**, 164–167 (2016).
189. J. Zou, T. Zhan, E. L. Hsiang, X. Du, X. Yu, K. Li, and S. T. Wu, "Doubling the optical efficiency of VR systems with a directional backlight and a diffractive deflection film," Opt. Express **29**, 20673–20686 (2021).
190. Y. J. Wang, S. H. Ouyang, W. C. Chao, J. G. Lu, and H. P. D. Shieh, "High directional backlight using an integrated light guide plate," Opt. Express **23**, 1567–1575 (2015).
191. Y. Zhang, D. Yi, W. Qiao, and L. Chen, "Directional backlight module based on pixelated nano-gratings," Opt. Commun. **459**, 125034 (2020).
192. A. Ghosh, I. Khayrullin, F. Vazan, F. Zhao, H. Lin, O. Prache, L. Sziklas, S. Peruvemba, and A. Sculley, "Developing the world's brightest WUXGA OLED microdisplay," Inf. Disp. **38**, 19–23 (2022).
193. X. Fu, S. Yin, Y. A. Chen, L. Zhu, Q. Dong, C. H. Chang, and F. So, "Light extraction in tandem organic light emitting diodes," Appl. Phys. Lett. **119**, 060504 (2021).
194. B. Pyo, C. W. Joo, H. S. Kim, B. H. Kwon, J. I. Lee, J. Lee, and M. C. Suh, "A nanoporous polymer film as a diffuser as well as a light extraction component for top emitting organic light emitting diodes with a strong microcavity structure," Nanoscale **8**, 8575–8582 (2016).
195. J. Kim, Y. Qu, C. Coburn, and S. R. Forrest, "Efficient outcoupling of organic light-emitting devices using a light-scattering dielectric layer," ACS Photonics **5**, 3315–3321 (2018).
196. J. Song, K. H. Kim, E. Kim, C. K. Moon, Y. H. Kim, J. J. Kim, and S. Yoo, "Lens-free OLEDs with over 50% external quantum efficiency via external scattering and horizontally oriented emitters," Nat. Commun. **9**, 3207 (2018).

197. M. Thomschke, S. Reineke, B. Lüssem, and K. Leo, "Highly efficient white top-emitting organic light-emitting diodes comprising laminated microlens films," Nano Lett. **12**, 424–428 (2012).
198. Y. Sun and S. R. Forrest, "Organic light emitting devices with enhanced out-coupling via microlenses fabricated by imprint lithography," J. Appl. Phys. **100**, 073106 (2006).
199. Y. Motoyama, K. Sugiyama, H. Tanaka, H. Tsuchioka, K. Matsusaki, and H. Fukumoto, "High-efficiency OLED microdisplay with microlens array," J. Soc. Inf. Disp. **27**, 354–360 (2019).
200. K. Itonaga, S. Sudo, J. Nishikawa, K. Kimura, H. Uchiyama, M. Yagi, R. Sawano, T. Matsuyama, K. Sasaki, K. Itatsu, T. Tsuchiya, Y. Nomura, and Y. Sato, "47-1: the world smallest OLED microdisplay projection device design methodology," Dig. Tech. Pap. - Soc. Inf. Disp. Int. Symp. **51**, 683–686 (2020).
201. S. Amoah, X. Fu, S. Yin, Q. Dong, C. Dong, and F. So, "Curved mirror arrays for light extraction in top-emitting organic light-emitting diodes," ACS Appl. Mater. Interfaces **14**, 9377–9385 (2022).
202. X. Fu, Y. A. Chen, D. H. Shin, Y. Mehta, I. T. Chen, N. Barange, L. Zhu, S. Amoah, C. H. Chang, and F. So, "Recovering cavity effects in corrugated organic light emitting diodes," Opt. Express **28**, 32214–32225 (2020).
203. J. Liang, Y. Du, K. Wang, A. Ren, X. Dong, C. Zhang, J. Tang, Y. Yan, and Y. S. Zhao, "Ultrahigh color rendering in RGB perovskite micro-light-emitting diode arrays with resonance-enhanced photon recycling for next generation displays," Adv. Opt. Mater. **10**, 2101642 (2022).
204. X. Fu, Y. Mehta, Y. A. Chen, L. Lei, L. Zhu, N. Barange, Q. Dong, S. Yin, J. Mendes, S. He, R. Gogusetti, C. H. Chang, and F. So, "Directional polarized light emission from thin-film light-emitting diodes," Adv. Mater. **33**, 2006801 (2021).
205. S. J. Lee, C. mo Kang, J. W. Shin, D. H. Ahn, C. W. Joo, H. Cho, N. S. Cho, H. M. Youn, Y. J. An, J. S. Kim, J. Lee, and H. Lee, "Three-wavelength white organic light-emitting diodes on silicon for high luminance and color gamut microdisplays," J. Ind. Eng. Chem. **105**, 132–137 (2022).
206. H. Cho, C. W. Byun, C. M. Kang, J. W. Shin, B. H. Kwon, S. Choi, N. S. Cho, J. I. Lee, H. Kim, J. H. Lee, M. Kim, and H. Lee, "White organic light-emitting diode (OLED) microdisplay with a tandem structure," J. Inf. Disp. **20**, 249–255 (2019).
207. L. Penninck, M. Diethelm, S. Altazin, R. Hiestand, C. Kirsch, and B. Ruhstaller, "Modelling crosstalk through common semiconductor layers in AMOLED displays," J. Soc. Inf. Disp. **26**, 546–554 (2018).
208. H. W. Bae, Y. W. Kwon, M. An, J. Kim, J. H. Kwon, and D. Lee, "High-color-stability and low-driving-voltage white organic light-emitting diodes on silicon with interlayers of thin charge generation units for microdisplay applications," ACS Appl. Electron. Mater. **3**, 3240–3246 (2021).
209. H. Cho, C. W. Joo, S. Choi, C. mo Kang, G. H. Kim, J. W. Shin, B. H. Kwon, H. Lee, C. W. Byun, and N. S. Cho, "Design of white tandem organic light-emitting diodes for full-color microdisplay with high current efficiency and high color gamut," ETRI Journal **43**, 1093–1102 (2021).
210. U. Vogel, B. Richter, P. Wartenberg, P. König, O. R. Hild, K. Fehse, M. Schober, E. Bodenstein, and B. Beyer, "OLED microdisplays in near-to-eye applications: challenges and solutions," Proc. SPIE **10335**, 1033503 (2017).
211. S. K. Kim, M. J. Park, R. Lampande, S. W. Jung, H.-U. Park, J. K. Jeong, and J. H. Kwon, "Primary color generation from white organic light-emitting diodes using a cavity control layer for AR/VR applications," Org. Electron. **87**, 105938 (2020).

212. H. Cho, C. W. Joo, S. Choi, C. mo Kang, B. H. Kwon, J. W. Shin, K. Kim, D. H. Ahn, and N. S. Cho, "Organic light-emitting diode structure for high color gamut in high-resolution microdisplay: over 90% color gamut based on BT.2020," Org. Electron. **101**, 106419 (2022).
213. M. K. Fung, Y. Q. Li, and L. S. Liao, "Tandem organic light-emitting diodes," Adv. Mater. **28**, 10381–10408 (2016).
214. W. J. Joo, J. Kyoung, M. Esfandyarpour, S. H. Lee, H. Koo, S. Song, Y. N. Kwon, S. H. Song, J. C. Bae, A. Jo, M. J. Kwon, S. H. Han, S. H. Kim, S. Hwang, and M. L. Brongersma, "Metasurface-driven OLED displays beyond 10,000 pixels per inch," Science **370**, 459–463 (2020).
215. F. Olivier, S. Tirano, L. Dupré, B. Aventurier, C. Largeron, and F. Templier, "Influence of size-reduction on the performances of GaN-based micro-LEDs for display application," J. Lumin. **191**, 112–116 (2017).
216. S. Han, C. Xu, H. Li, S. Liu, H. Xu, Y. Zhu, A. Fang, and X. Wang, "AlGaInP-based micro-LED array with enhanced optoelectrical properties," Opt. Mater. **114**, 110860 (2021).
217. M. S. Wong, J. A. Kearns, C. Lee, J. M. Smith, C. Lynsky, G. Lheureux, H. Choi, J. Kim, C. Kim, S. Nakamura, S. Nakamura, J. S. Speck, S. P. DenBaars, and S. P. DenBaars, "Improved performance of AlGaInP red micro-light-emitting diodes with sidewall treatments," Opt. Express **28**, 5787–5793 (2020).
218. H. H. Huang, S. K. Huang, Y. L. Tsai, S. W. Wang, Y. Y. Lee, S. Y. Weng, H. C. Kuo, and C. chung Lin, "Investigation on reliability of red micro-light emitting diodes with atomic layer deposition passivation layers," Opt. Express **28**, 38184–38195 (2020).
219. J. Park, W. Baek, D. M. Geum, and S. Kim, "Understanding the sidewall passivation effects in AlGaInP/GaInP micro-LED," Nanoscale Res. Lett. **17**, 29 (2022).
220. M. S. Wong, D. Hwang, A. I. Alhassan, C. Lee, R. Ley, S. Nakamura, and S. P. DenBaars, "High efficiency of III-nitride micro-light-emitting diodes by sidewall passivation using atomic layer deposition," Opt. Express **26**, 21324–21331 (2018).
221. D. Chen, Z. Wang, F. C. Hu, C. Shen, N. Chi, W. Liu, W. Liu, D. W. Zhang, H. L. Lu, and H. L. Lu, "Improved electro-optical and photoelectric performance of GaN-based micro-LEDs with an atomic layer deposited AlN passivation layer," Opt. Express **29**, 36559–36566 (2021).
222. M. S. Wong, C. Lee, D. J. Myers, D. Hwang, J. A. Kearns, T. Li, J. S. Speck, S. Nakamura, and S. P. DenBaars, "Size-independent peak efficiency of III-nitride micro-light-emitting-diodes using chemical treatment and sidewall passivation," Appl. Phys. Express **12**, 097004 (2019).
223. J. M. Smith, R. Ley, M. S. Wong, Y. H. Baek, J. H. Kang, C. H. Kim, M. J. Gordon, S. Nakamura, J. S. Speck, and S. P. DenBaars, "Comparison of size-dependent characteristics of blue and green InGaN microLEDs down to 1 μm in diameter," Appl. Phys. Lett. **116**, 071102 (2020).
224. K. A. Bulashevich and S. Yu Karpov, "Impact of surface recombination on efficiency of III-nitride light-emitting diodes," Phys. Status Solidi. Rapid Res. Lett. **10**, 480–484 (2016).
225. Z. Zhuang, D. Iida, and K. Ohkawa, "InGaN-based red light-emitting diodes: from traditional to micro-LEDs," Jpn. J. Appl. Phys. **61**, SA0809 (2022).
226. Z. Zhuang, D. Iida, M. Velazquez-Rizo, and K. Ohkawa, "630-nm red InGaN micro-light-emitting diodes (<20 μm × 20 μm) exceeding 1 mW/mm2 for full-color micro-displays," Photonics Res. **9**, 1796–1802 (2021).
227. P. Li, H. Li, H. Zhang, C. Lynsky, M. Iza, J. S. Speck, S. Nakamura, and S. P. DenBaars, "Size-independent peak external quantum efficiency (>2%) of InGaN

red micro-light-emitting diodes with an emission wavelength over 600 nm," Appl. Phys. Lett. **119**, 081102 (2021).
228. Y. Zhao, Y. Zhao, J. Liang, Q. Zeng, Y. Li, Y. Li, P. Li, P. Li, K. Fan, K. Fan, W. Sun, W. Sun, J. Lv, Y. Qin, Q. Wang, J. Tao, J. Tao, W. Wang, and W. Wang, "2021 PPI silicon-based AlGaInP red micro-LED arrays fabricated via wafer bonding and epilayer lift-off," Opt. Express **29**, 20217–20228 (2021).
229. J. T. Oh, S. Y. Lee, Y. T. Moon, J. H. Moon, S. Park, K. Y. Hong, K. Y. Song, C. Oh, J. I. Shim, H. H. Jeong, J. O. Song, H. Amano, and T. Y. Seong, "Light output performance of red AlGaInP-based light emitting diodes with different chip geometries and structures," Opt. Express **26**, 11194–11200 (2018).
230. P. Li, H. Li, M. S. Wong, P. Chan, Y. Yang, H. Zhang, M. Iza, J. S. Speck, S. Nakamura, and S. P. Denbaars, "Progress of InGaN-based red micro-light emitting diodes," Crystals **12**, 541 (2022).
231. S. Lan, H. Wan, J. Zhao, and S. Zhou, "Light extraction analysis of AlGaInP based red and GaN based blue/green flip-chip micro-LEDs using the monte carlo ray tracing method," Micromachines **10**, 860 (2019).
232. R. T. Ley, J. M. Smith, M. S. Wong, T. Margalith, S. Nakamura, S. P. DenBaars, and M. J. Gordon, "Revealing the importance of light extraction efficiency in InGaN/GaN microLEDs via chemical treatment and dielectric passivation," Appl. Phys. Lett. **116**, 251104 (2020).
233. A. A. Erchak, D. J. Ripin, S. Fan, P. Rakich, J. D. Joannopoulos, E. P. Ippen, G. S. Petrich, and L. A. Kolodziejski, "Enhanced coupling to vertical radiation using a two-dimensional photonic crystal in a semiconductor light-emitting diode," Appl. Phys. Lett. **78**, 563–565 (2001).
234. A. David, H. Benisty, and C. Weisbuch, "Photonic crystal light-emitting sources," Rep. Prog. Phys. **75**, 126501 (2012).
235. C. Hoepfner, "61.1: invited paper: PhlatLight photonic lattice LEDs for RPTV light engines," Dig. Tech. Pap. - Soc. Inf. Disp. Int. Symp. **37**, 1808–1811 (2006).
236. E. Rangel, E. Matioli, Y. S. Choi, C. Weisbuch, J. S. Speck, and E. L. Hu, "Directionality control through selective excitation of low-order guided modes in thin-film InGaN photonic crystal light-emitting diodes," Appl. Phys. Lett. **98**, 081104 (2011).
237. E. L. Hsiang, Z. He, Z. Yang, Y. F. Lan, and S. T. Wu, "Tailoring the light distribution of micro-LED displays with a compact compound parabolic concentrator and an engineered diffusor," Opt. Express **29**, 39859–39873 (2021).
238. W. Henry and C. Percival, "55-2: invited paper: ILED displays: next generation display technology," Dig. Tech. Pap. - Soc. Inf. Disp. Int. Symp. **47**, 747–750 (2016).
239. S. Tanriseven, P. Maaskant, and B. Corbett, "Broadband quantum dot micro-light-emitting diodes with parabolic sidewalls," Appl. Phys. Lett. **92**, 123501 (2008).
240. E. Khaidarov, Z. Liu, R. Paniagua-Domínguez, S. T. Ha, V. Valuckas, X. Liang, Y. Akimov, P. Bai, C. E. Png, H. V. Demir, and A. I. Kuznetsov, "Control of LED emission with functional dielectric metasurfaces," Laser Photonics Rev. **14**, 1900235 (2020).
241. J. Huang, Z. Hu, X. Gao, Y. Xu, and L. Wang, "Unidirectional-emitting GaN-based micro-LED for 3D display," Opt. Lett. **46**, 3476–3479 (2021).
242. G. Y. Shiu, K. T. Chen, F. H. Fan, K. P. Huang, W. J. Hsu, J. J. Dai, C. F. Lai, and C. F. Lin, "InGaN light-emitting diodes with an embedded nanoporous GaN distributed bragg reflectors," Sci. Rep. **6**, 29138 (2016).
243. C. J. Wang, Y. Ke, G. Y. Shiu, Y. Y. Chen, Y. S. Lin, H. Chen, and C. F. Lin, "InGaN resonant-cavity light-emitting diodes with porous and dielectric reflectors," Appl. Sci. **11**, 8 (2020).

244. K. H. Fan Chiang, S. H. Chen, and S. T. Wu, "Diffraction effect on high-resolution liquid-crystal-on-silicon devices," Jpn. J. Appl. Phys. **44**, 3068–3072 (2005).
245. Z. Yang, T. Zhan, and S. T. Wu, "Polarization independent guided-mode resonance in liquid crystal-based polarization gratings," OSA Continuum **3**, 3107–3115 (2020).
246. Z. Yang, T. Zhan, and S. T. Wu, "Polarization-independent liquid crystal-based refractive index sensor," J. Soc. Inf. Disp. **29**, 305–310 (2021).
247. M. F. Weber, O. B. Jr, S. C. Jr, J. M. Jonza, A. J. Ouderkirk, D. L. Wortman, and C. A. Stover, "Display with reflective polarizer and randomizing cavity," U.S. patent application 6,025,897A (15 February 2000).
248. M. Duelli and A. T. Taylor, "16.3: Novel polarization conversion and integration system for projection displays," Dig. Tech. Pap. - Soc. Inf. Disp. Int. Symp. **34**, 766–769 (2003).
249. M. S. Brennesholtz and E. H. Stupp, *Projection Displays*, 2nd ed. (Wiley, 2008).
250. T. Zhan, Y. H. Lee, G. Tan, J. Xiong, K. Yin, F. Gou, J. Zou, N. Zhang, D. Zhao, J. Yang, S. Liu, and S. T. Wu, "Pancharatnam–berry optical elements for head-up and near-eye displays [Invited]," J. Opt. Soc. Am. B **36**, D52–D65 (2019).
251. T. Du, F. Fan, A. M. W. Tam, J. Sun, V. G. Chigrinov, and H. S. Kwok, "Complex nanoscale-ordered liquid crystal polymer film for high transmittance holographic polarizer," Adv. Mater. **27**, 7191–7195 (2015).
252. J. Kim, R. K. Komanduri, K. F. Lawler, D. J. Kekas, and M. J. Escuti, "Efficient and monolithic polarization conversion system based on a polarization grating," Appl. Opt. **51**, 4852–4857 (2012).
253. Texas Instruments, "DMD Optical Efficiency for Visible Wavelengths," https://www.ti.com/lit/pdf/dlpa083.
254. Y. X. Ren, R. D. Lu, and L. Gong, "Tailoring light with a digital micromirror device," Ann. Phys. **527**, 447–470 (2015).
255. M. J. Deng, Y. Y. Zhao, Z. X. Liang, J. T. Chen, Y. Zhang, and X. M. Duan, "Maximizing energy utilization in DMD-based projection lithography," Opt. Express **30**, 4692–4705 (2022).
256. S. Essaian and J. Khaydarov, "State of the art of compact green lasers for mobile projectors," Opt. Rev. **19**, 400–404 (2012).
257. R. Stevenson, "Lasers get the green light," IEEE Spectrum **47**, 34–39 (2010).
258. U. Hofmann, J. Janes, and H. J. Quenzer, "High-Q MEMS resonators for laser beam scanning displays," Micromachines **3**, 509–528 (2012).
259. A. Avramescu, T. Lermer, J. Müller, C. Eichler, G. Bruederl, M. Sabathil, S. Lutgen, and U. Strauss, "True green laser diodes at 524 nm with 50 mW continuous wave output power on *c*-plane GaN," Appl. Phys. Express **3**, 061003 (2010).
260. H. C. Yu, Z. W. Zheng, Y. Mei, R. B. Xu, J. P. Liu, H. Yang, B. P. Zhang, T. C. Lu, and H. C. Kuo, "Progress and prospects of GaN-based VCSEL from near UV to green emission," Prog. Quantum Electron. **57**, 1–19 (2018).
261. L. Jiang, J. Liu, A. Tian, Y. Cheng, Z. Li, L. Zhang, S. Zhang, D. Li, M. Ikeda, and H. Yang, "GaN-based green laser diodes," J. Semicond. **37**, 111001 (2016).
262. N. Boni, R. Carminati, G. Mendicino, M. Merli, D. Terzi, B. Lazarova, and M. Fusi, "Piezoelectric MEMS mirrors for the next generation of small form factor AR glasses," Proc. SPIE **12013**, 1201305 (2022).
263. H. Urey, N. Nestorovic, B. S. Ng, and A. A. Gross, "Optics designs and system MTF for laser scanning displays," Proc. SPIE **3689**, 238–248 (1999).
264. R. Mukherjee, K. Debattista, T. Bashford-Rogers, B. Waterfield, and A. Chalmers, "A study on user preference of high dynamic range over low dynamic range video," Vision Comput. **32**, 825–834 (2016).

265. Z. Yang, E. L. Hsiang, Y. Qian, and S. T. Wu, "Performance comparison between mini-LED backlit LCD and OLED display for 15.6-inch notebook computers," Appl. Sci. **12**, 1239 (2022).
266. Y. Zhao, N. Matsuda, X. Wang, M. Zannoli, and D. Lanman, "High dynamic range near-eye displays," Proc. SPIE **11310**, 113100X (2020).
267. G. Tan, Y. Huang, M. C. Li, S. L. Lee, and S. T. Wu, "High dynamic range liquid crystal displays with a mini-LED backlight," Opt. Express **26**, 16572–16584 (2018).
268. E. L. Hsiang, Q. Yang, Z. He, J. Zou, and S. T. Wu, "Halo effect in high-dynamic-range mini-LED backlit LCDs," Opt. Express **28**, 36822–36837 (2020).
269. M. Xu and H. Hua, "High dynamic range head mounted display based on dual-layer spatial modulation," Opt. Express **25**, 23320–23333 (2017).
270. Y. C. Huang and J. W. Pan, "High contrast ratio and compact-sized prism for DLP projection system," Opt. Express **22**, 17016–17029 (2014).
271. G. Damberg, J. Gregson, and W. Heidrich, "High brightness HDR projection using dynamic freeform lensing," ACM Trans. Graph. **35**, 1–11 (2016).
272. Y. Meuret, "Contrast-improving methods for digital micromirror device projectors," Opt. Eng. **42**, 840–845 (2003).
273. J. W. Pan and H. H. Wang, "High contrast ratio prism design in a mini projector," Appl. Opt. **52**, 8347–8354 (2013).
274. W. C. Ding and J. W. Pan, "High-contrast ratio and high-efficiency anamorphic DLP illumination system design with a freeform surface lens," Appl. Opt. **60**, 6255–6263 (2021).
275. H. Urey, "P-82: diffraction limited resolution and maximum contrast for scanning displays," Dig. Tech. Pap. - Soc. Inf. Disp. Int. Symp. **31**, 866–869 (2000).
276. O. Petrak, F. Schwarz, L. Pohl, M. Reher, C. Janicke, J. Przytarski, F. Senger, J. Albers, T. Giese, L. Ratzmann, P. Blicharski, S. Marauska, T. von Wantoch, and U. Hofmann, "Laser beam scanning based AR-display applying resonant 2D MEMS mirrors," Proc. SPIE **11765**, 1176503 (2021).
277. F. Fidler, A. Balbekova, L. Noui, S. Anjou, T. Werner, and J. Reitterer, "Laser beam scanning in XR: benefits and challenges," Proc. SPIE **11765**, 1176502 (2021).
278. K. V. Chellappan, E. Erden, and H. Urey, "Laser-based displays: a review," Appl. Opt. **49**, F79–F98 (2010).
279. Jade Bird Display, "AmμLEDTM development kits," https://www.jb-display.com/development-kits.
280. E. Tang, "Smallest LED light engines for AR," Proc. SPIE **11932**, 119321W (2022).
281. J. Reitterer, "Trixel 3 – the world's smallest laser beam scanner for high-volume consumer augmented reality applications," Proc. SPIE **11932**, 1193209 (2022).
282. G. Haas, "52-1: invited paper: microdisplays for wearable augmented reality — OLED vs LED based systems (invited)," Dig. Tech. Pap. - Soc. Inf. Disp. Int. Symp. **50**, 713–716 (2019).
283. Z. Chen, S. Yan, and C. Danesh, "MicroLED technologies and applications: characteristics, fabrication, progress, and challenges," J. Phys. D: Appl. Phys. **54**, 123001 (2021).
284. Y. H. Ju, J. H. Park, J. H. Lee, J. Y. Lee, K. B. Nahm, J. H. Ko, and J. H. Kim, "Study on the simulation model for the optimization of optical structures of edge-lit backlight for LCD applications," J. Opt. Soc. Korea **12**, 25–30 (2008).
285. T. Levola and P. Ayras, "Illumination of LCOS micro displays using planar lightguides," in *2008 2nd Electronics System-Integration Technology Conference* (2008), pp. 815–818.

286. Y. W. Li, C. W. Lin, K. Y. Chen, K. H. Fan-Chiang, H. C. Kuo, and H. C. Tsai, "18.5L: late-news paper: front-lit LCOS for wearable applications," Dig. Tech. Pap. - Soc. Inf. Disp. Int. Symp. **45**, 234–236 (2014).
287. K. Y. Chen, Y. W. Li, K. H. Fan-Chiang, H. C. Kuo, and H. C. Tsai, "P-181L: late-news poster: color sequential front-lit LCOS for wearable displays," Dig. Tech. Pap. - Soc. Inf. Disp. Int. Symp. **46**, 1737–1740 (2015).
288. J. Busch and G. Scheib, "Front lighting system for liquid crystal display," U.S. patent application 5,477,239A (19 December 1995).
289. E. H. Arend, S. Bhargava, H.-C. Cheng, K. R. Curtis, M. H. Schuck III, and B. J. Sissom, "Waveguide illuminator," U.S. patent application US17/571,366 (13 June 2019).
290. K. R. Curtis, "Unveiling magic Leap 2's advanced AR platform and revolutionary optics," Proc. SPIE **11932**, 119320P (2022).

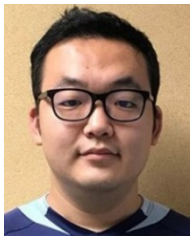

En-Lin Hsiang received his BS and MS degrees from National Chiao Tung University, Hsinchu, Taiwan, in 2014 and 2016, respectively. Currently, he is working toward a PhD at the College of Optics and Photonics, University of Central Florida, USA. His current research focuses on advanced display technologies including high-dynamic-range flat panel display and light engines for AR/VR displays.

Zhiyong Yang received his BS degree in Optoelectronic Engineering from Chongqing University in 2017 and MS degree in Electrical Engineering and Computer Science from the University of Michigan, Ann Arbor, in 2019. He is currently working toward a PhD from the College of Optics and Photonics, University of Central Florida. His current research interests include liquid-crystal-on-silicon, mini-LED backlight, OLED display, and μLED display.

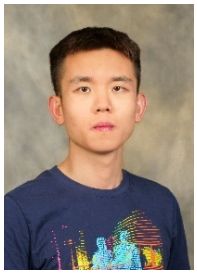

Qian Yang received his BS degree in Physics from Nanjing University in 2017 and MS degree in Physics from University of Rochester in 2019. He is currently working toward a PhD from the College of Optics and Photonics, University of Central Florida. His current research interests include liquid crystal SLMs for LiDAR applications, planar optics for AR/VR displays, and mini-LED and μLED displays.

Po-Cheng Lai received his BS degree in Electrical Engineering from Feng Chia University, Taiwan, in 2014, and MS and PhD degrees in Electrical Engineering from National Cheng Kung University, Taiwan, in 2016 and 2022, respectively. His research focuses on the pixel circuit design for active-matrix OLEDs and gate driver circuit design for active-matrix LCDs.

Chih-Lung Lin received his BS and PhD degrees in Electrical Engineering from National Taiwan University, Taiwan, in 1993 and 1999, respectively. He is currently the chair of the Department of Electrical and Engineering, National Cheng Kung University, Tainan, Taiwan. His current research interests include pixel circuit

design for AMOLED, gate driver circuit design for AMLCD, and flexible display circuits.

Shin-Tson Wu is a Trustee Chair Professor at College of Optics and Photonics, University of Central Florida. He received his PhD in Physics from the University of Southern California and BS in Physics from National Taiwan University. He is an Academician of Academia Sinica, a Charter fellow of National Academy of Inventors, and a recipient of Optica Edwin H. Land Medal (2022), SPIE Maria Goeppert-Mayer Award (2022), OSA Esther Hoffman Beller Medal (2014), SID Slottow-Owaki Prize (2011), OSA Joseph Fraunhofer Award (2010), SPIE G. G. Stokes Award (2008), and SID Jan Rajchman Prize (2008). His research interests at UCF focus on augmented reality and virtual reality, including light engines, optical systems, and display materials.